RICE UNIVERSITY

Quantum Transport in Spatially Modulated Two-dimensional Electron and Hole Systems

by

Zhuoquan Yuan

A THESIS SUBMITTED
IN PARTIAL FULFILLMENT OF THE
REQUIREMENTS FOR THE DEGREE

Doctor of Philosophy

APPROVED, THESIS COMMITTEE:

_____

Ruirui Du, Professor, Chair
Physics and Astronomy

_____

Douglas Natelson, Associate Professor
Physics and Astronomy

_____

Junichiro Kono, Professor
Electrical and Computer Engineering

HOUSTON, TEXAS
MAY, 2009

To Xiaofan, my parents and my aunt

Abstract

Two-dimensional electron (2DES) and hole (2DHS) systems have attracted intense research attentions in past decades. A 2DES or 2DHS modulated by one-dimensional or two-dimensional spatially periodic potential shows particular importance because the existence of modulation provides a tunable parameter for exploring interaction between electrons and scattering centers presenting on the two-dimensional systems. This thesis documents a systematic experimental study, in collaboration with Bell Labs, of electronic transport in very-high mobility 2DES and 2DHS in GaAs/AlGaAs quantum structures. Fabrication of triangular antidot lattice in 2DES, as well as low-temperature transport and photoconductivity properties in spatially modulated 2DES, has been studied. Strong Geometric resonance (GR), up to seven peaks resolved, is observed in the longitudinal magnetoresistance because of high mobility of 2DES after fabrication of antidot lattice. Photoresistance shows clear millimeterwave-induced resistance oscillations (MIRO) but with heavily damping amplitudes, and magnetoplasmon resonance (MPR) is also observed as well. GR, MIRO and MPR are decoupled from each other in our modulated 2DES. These experimental findings pave the way for studies of nonlinear transport in modulated 2DES. Magnetotransport measurements on a new material, the Carbon δ-doped 2DHG in GaAs/AlGaAs quantum well, indicate that the 2DHG has a transport scattering time compatible with those in very-high mobility 2DES. However, photoresistance measurement shows much weaker MIRO in the 2DHS than that in 2DES with compatible transport scattering time. Low-temperature transport measurements on Landau, Zeeman, and spin-orbital parameters imply that the C-doped 2DHS has small zero field spin splitting and large effective g-factor. As part of the thesis work, the thesis

also presents a development of low-temperature/high magnetic field (300mK/12T) scanning Hall probe microscope (SHPM) technique for measuring small local magnetic fields at low temperature and an algorithm for calculating the current density from measured magnetic fields based on Fourier transformation technique. Integration of SHPM and the algorithm provides a practical tool for imaging the current distribution and a powerful method to explore electronic transport properties of 2DES and 2DHS.

Acknowledgements

Quantum Transport in Spatially Modulated Two-dimensional Electron and Hole Systems

Table of Contents

Table of Figures

Chapter One Introduction

In past decades, extensive researches on magneto-transport were done on Two Dimensional Electron Gas (2DEG). Following the most important discoveries of the Integer Quantum Hall Effect (IQHE) by K. von Klitzing, G. Dorda and M. Pepper in 1980 [1], and the Fractional Quantum Hall Effect (FQHE) by D. C. Tsui, H. L. Stormer and A. C. Gossard in 1982 [2], many new interesting phenomena were observed in 2DEG, see Ref. 3. This thesis will focus on magnetotransport in the low magnetic field regime, where novel effects have been reported, including Geometric Resonance (GR) [4-7], Microwave Induced Resistance Oscillations (MIRO) [8, 9] and microwave induced Zero-Resistance State (ZRS) [10, 11] or Zero-Conductance State (ZCS) [12].

Under one-dimensional [4-6] or two dimensional [7] spatially periodic modulation, magnetoresistance in 2DEG showed Geometric Resonance (GR) when commensurability occurs between two length scales, period of modulation, a, and diameter of cyclotron orbit, $2R_c$. More details of GR will be covered in section 2.6. The presence of spatially periodic modulation breaks the translational symmetry of the 2DEG system. If the 2DEG is clean enough after introduction of modulation, it will be an appropriate system for studies of photoresistance with finite momentum transfer $\Delta q = 2\pi/a$ under break of translational symmetry.

Under microwave irradiation, a new type of oscillations, named MIRO, was observed in an ultraclean 2DEG [8,9] and in higher mobility 2DEG under sufficiently strong microwave irradiation, MIRO develops into Zero-Resistance State (ZRS) [10,11] or Zero-Conductance State (ZCS) [12]. It is believed that the MIRO arises from transitions

between multiply of Landau Levels (LLs) excited by short-range scattering, while the microscopic origin of MIRO and ZRS still remain unknown. More details of MIRO and ZRS will be presented in section 2.7. In our experiments, we explored MIRO and ZRS in a 2DEG patterned 2D modulation, triangular antidot lattice [13]. The experimental result of influence of 2D modulation on MIRO will be reported in this thesis. It was found that the presence of 2D modulation had little effect on MIRO, and GR and MIRO are decoupled, while ZRS was damped out due to a fourfold drop of mobility of 2DEG.

It is suggested [14] that current distribution of ZRS is the key to address its exact microscopic origin. Therefore imaging of current distribution will be a straightforward way to settle the issue. In this thesis, a development of low temperature Scanning Hall Probe Microscope (SHPM) technique will be presented. With this low temperature SHPM, imaging current distribution of ZRS is proposed.

At the same time, the two-dimensional hole gas (2DHG) has also attracted much research attentions because of its unique charge and spin properties derived from valence band structure. Extensive experiments have been performed on 2DHG to reproduce observed effects on 2DEG. IQHE and FQHE were successfully observed on 2DHG [15, 16]. However, MIRO on 2DHG is much weaker than on 2DEG [17], and ZRS is totally absent on 2DHG, even the 2DHG has the comparable scattering time with 2DEG. This discrepancy implies that further understanding of properties of 2DHG and the mechanism of ZRS are needed. In this thesis, I will present an investigation of magnetotransport on 2DHG, including measurement of effective mass and g-factor of a 2DHG in GaAs/AlGaAs quantum well, and observation of GR and MIRO in 2DHG.

This thesis is organized in five parts. First, related background of magneto-transport will be reviewed in Chapter two. Then in Chapter three, magneto-transport in 2DEG patterned triangular antidot lattice is presented. In Chapter four, I will present the results of magnetotransport in Two Dimensional Hole Gas (2DHG) in a Carbon δ-doped GaAs/AlGaAs quantum well. A development of Scanning Hall Probe Microscope (SHPM) technique to image current distribution will be introduced in Chapter five. Finally, conclusion will be given on Chapter six.

Chapter Two Background of Magneto-Transport

2.1. Formation of high mobility 2DEG

High mobility 2DEG can be realized at the interface of two semiconductors with modulation-doping. The most popular pair of semiconductors is GaAs and $Al_xGa_{1-x}As$. By changing x, the ratio of component Al, lattice constant of $Al_xGa_{1-x}As$ can be adjusted to match that of GaAs to make the interface defect free. It was reported that the quality of 2DEG is mainly influenced by three factors [18]: scattering from ions in doped layer, interface roughness, and impurities in 2DEG. A smooth interface can significantly improve the quality of 2DEG. And with Molecular Beam Epitaxy (MBE) technique, impurities in the 2DEG can be controlled at very low level so that they will not be a dominant factor on determining quality of 2DEG. Actually in most samples used in our experiments, scattering from ions in the doped layer is the dominant factor influencing quality of 2DEG. The typical GaAs/$Al_xGa_{1-x}As$ heterostructure is shown in Fig. 2.1.

2.2. 2DEG under magnetic field

Electron motion under magnetic field is well known text book knowledge. Here I will give a brief review of it. For more details, please check Ref. 19. Let's consider an electron in 2DEG under a magnetic field B applied in the z direction, perpendicular to the 2DEG, i.e., $B = (0, 0, B)$ and using the Landau gauge, we have the vector potential $A = (0, B x, 0)$. Then the Schrödinger equation of the electron in 2DEG has form:

$$\frac{1}{2m}\left[p_x^2 + (p_y - eBx)^2\right]\Psi(x,y) = \varepsilon\Psi(x,y) \tag{2.1}$$

where $m = m^* m_e$ is mass of electron in 2DEG, m^* is the effective mass of electron and

(a) cross section of GaAs/AlGaAs heterostructure
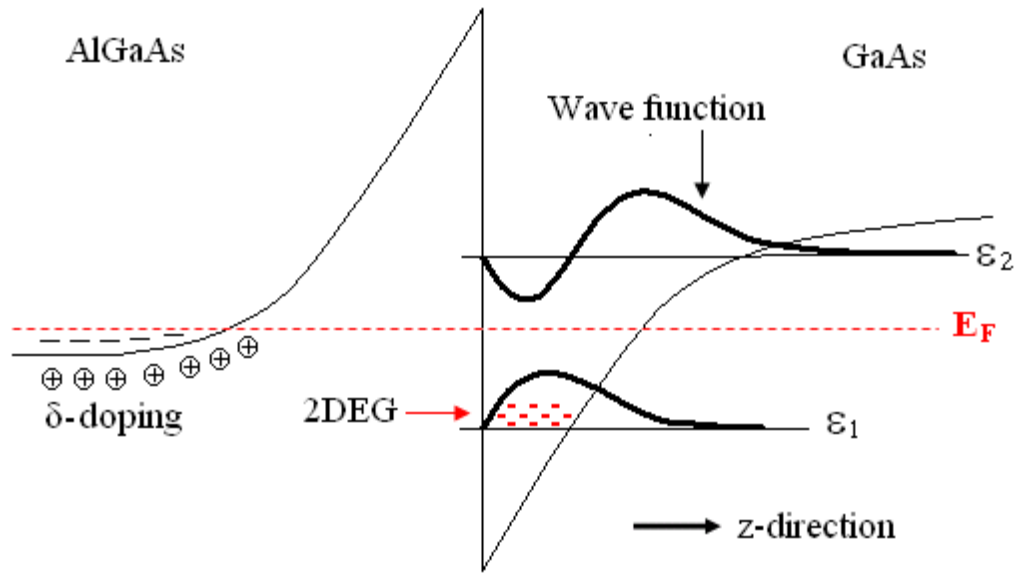
(b) band diagram

Fig. 0.1 Diagrams of typical GaAs/ Al$_x$Ga$_{1-x}$As heterostructure.

m_e is bare electron mass. As the Hamiltonian $H = \frac{1}{2m}\left[p_x^2 + (p_y - eBx)^2\right]$ is y independent and the wave functions can be written as:

$$\Psi(x,y) = e^{ik_y y} u(x) \tag{2.2}$$

where k_y is wave vector on y direction. Substitute Eq. (2.2) into (2.1), it is easy to attain equation for $u(x)$ with $p_x = i\hbar\frac{\partial}{\partial x}$ and $p_y = i\hbar\frac{\partial}{\partial y}$:

$$\left[-\frac{\hbar^2}{2m}\frac{d^2}{dx^2} + \frac{1}{2}m\omega_c^2\left(x - \frac{\hbar k_y}{eB}\right)^2 \right] u(x) = \varepsilon u(x) \tag{2.3}$$

where $\omega_c = eB/m$ is cyclotron frequency. Eq. (2.3) is the Schrödinger equation for one-dimensional harmonic oscillator which has solution:

$$u(x) = \phi_n(x - X_k) = \left(\frac{1}{2^n n!\,\sqrt{\pi}l_B}\right)^{1/2} exp\left[-\frac{(x - X_k)^2}{l_B^2} \right] H_{n-1}\left(\frac{x - X_k}{l_B^2}\right) \tag{2.4}$$

where $n = 1, 2, \dots$is an integer, $X_k \equiv \hbar k_y/(eB) = l_B^2 k_y$ is the center of the cyclotron orbit, $l_B \equiv \sqrt{\hbar/(eB)} = \sqrt{\hbar/(m\omega_c)}$ is magnetic length, and $H_n\,(x)$ are the Hermite polynomials. Therefore we can now attain the solutions of the wave functions and energies for electron motion in 2DEG:

$$\Psi_n(x, y) = \phi_n(x - X_k)\exp(ik_y y) \tag{2.5}$$

$$\varepsilon_n = \left(n - \frac{1}{2}\right)\hbar\omega_c \tag{2.6}$$

These solutions have several important features.

The first one is that the probability density $|\Psi_n(x, y)|^2$ is independent on y so that the density is consisted of parallel strips in the y direction, which are equally spaced along x direction. From Eq. (2.4), it is obvious that the width of the strip is in the order of l_B. The separation between adjacent strips is given by distance between two adjacent centers of cyclotron orbits, ΔX. If sample has dimensions of $L_x \times L_y$, then with periodic boundary condition, we have $k_y = j(2\pi/L_y)$ with j an integer. The separation is given by $\Delta X_k = l_B^2 \Delta k_y = 2\pi l_B^2/L_y$. At $B = 1$ T , $l_B \approx 26nm$, which usually is much smaller than 2DEG sample size, L_y ; hence we have $\Delta X_k \ll l_B$. There is no gap between two adjacent density strips. And this distinction of between x and y directions shall result from the

gauge chosen for vector potential. It's the Landau gauge, $A = (0, Bx, 0)$ which we can see obvious distinction between x and y directions.
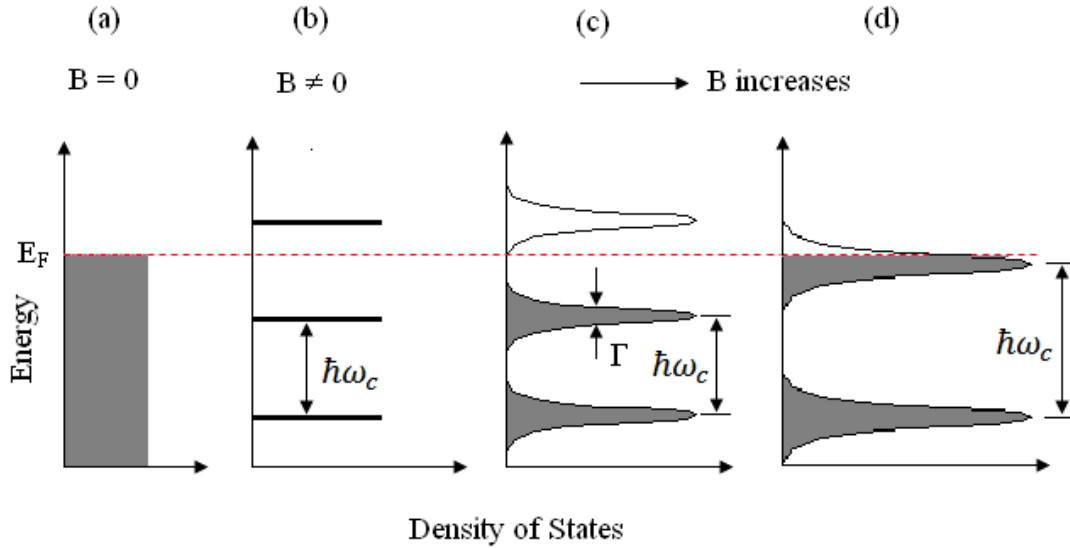
Fig.0.2 Diagrams of density of states of 2DEG without and with magnetic field. (a) density of states at $B = 0$; (b) density of states of Landau levels in ideal condition; (c) and (d) density of states of Landau level with level broadening due to scattering.

The second property is that electrons in 2DEG under magnetic field have a discrete energy spectrum given by Eq. (2.6). The energy level, so-called Landau level, only depends on index n and the spacing between two adjacent energy level is constant at fixed magnetic field, equal to $\hbar\omega_c$. All states with different k_y but same n are degenerate. The density of states collapses from a uniform function below the Fermi energy into a series of δ-functions, as shown in Fig. 2.2 (a) and (b). In a real 2DEG, the electron is scattered by other electrons, holes, phonons and impurities. This scattering will broaden the Landau level so that density of states can't be described by δ-functions. A common assumption is that the density of states has Gaussian or Lorentzian profile, as shown in

Fig. 2.2 (c) and (d). With a Gaussian or Lorentzian profile, the Landau level will acquire

a width, Γ, which is precisely defined as the full width at half-maximum (FWHM) of

profile of Landau level. The electron scattering can be characterized by a scattering time,

or quantum lifetime, τ_q, which is defined as the typical time span between two scattering

events. We attain an important relation $\Gamma = \hbar/\tau_q$, which clearly indicates the origin of

Landau level broadening. From Fig. 2.2 (d), it is clear to see that the Landau levels can be

separated only when $\hbar\omega_c > \Gamma$. This requirement also can be written as $\omega_c\tau_q > 1$ which

means that electron has to survive long enough without scattering to complete at least one

cyclotron orbit in order to resolve the Landau levels.

As the energy of a Landau level only depends on index n, all the states with different

wave vector k_y but same n will be degenerate. To determine the degeneracy of Landau

level, we need to know the number of states in each Landau level. We suppose the 2DEG

system has rectangular dimensions $L_x \times L_y$. Periodic boundary conditions give condition

$k_y = j(2\pi/L_y)$ with j an integer. Under Landau gauge, the cyclotron orbit center,

locating at $X = \hbar k_y/(eB) = j2\pi\,\hbar/(eBL_y)$, shall be inside the sample, that is $0 < X_k <$

L_x. So we have condition $0 < j \le eBL_xL_y/h$. Thus the total number of states in each

Landau level per unit area is $n_B = eB/h$, which is the degeneracy of Landau level. In

real space, the area occupied by each state in Landau level is given by $1/n_B = h/(eB) =$

$2\pi l_B^2$.

From Fig. 2.2 (c) and (d), we can see that when magnetic field increases, separation

between adjacent Landau levels, $\hbar\omega_c$, becomes larger. And number of states in each

Landau level also increases. In a 2DEG sample, the density of electron, n_{2D}, is constant

under magnetic field. Therefore the number of occupied Landau level, named as filling factor v, must decrease. With degeneracy of Landau level, filling factor can be written as:

$$v = \frac{n_{2D}}{n_B} = \frac{h}{eB} n_{2D} \qquad (2.7)$$

Filling factor is usually not an integer, but when Fermi level, E_F, lies between two separated Landau levels, all Landau levels below E_F are full while levels above E_F are totally empty so that $v = 2n$ (spin degeneracy of n), shown in Fig. (c) and (d).

Under increasing magnetic field, Fermi level will move down to lower Landau level and the density of states at E_F will be an oscillatory function of filling factor. This oscillatory behavior of the density of states at E_F results in the well-known Shubnikov-de Haas oscillation [19].

2.3. Transport in 2DEG

2.3.1. Classical transport in 2DEG

Consider a 2DEG under static electric field, $\boldsymbol{E} = (E_x, E_y)$ and magnetic field, B, applied on z direction. Given the velocity of electron $\boldsymbol{v} = (v_x, v_y)$, Newton's second law of motion gives equations:

$$\begin{cases} m\left(\dfrac{d}{dt} + \dfrac{1}{\tau_{tr}}\right) v_x = -e\left(E_x + v_y B\right) \\ m\left(\dfrac{d}{dt} + \dfrac{1}{\tau_{tr}}\right) v_y = -e\left(E_y - v_x B\right) \end{cases} \qquad (2.8)$$

where τ_{tr} is the transport lifetime or collision time describing the collisions of electrons with impurities, lattice imperfections and phonons. At a steady state, velocity of electrons shall not change with time. Thus Eq. (2.8) gives expressions for v_x and v_y:

9

$$\begin{cases} v_x = -\mu(E_x - \omega_c \tau_{tr} E_y)/(1 + \omega_c^2 \tau_{tr}^2) \\ v_y = -\mu(\omega_c \tau_{tr} E_x + E_y)/(1 + \omega_c^2 \tau_{tr}^2) \end{cases} \qquad (2.9)$$

where $\mu = e\tau_{tr}/m$ is mobility. With current density $\boldsymbol{j} = -en\boldsymbol{v}$ and relation $\boldsymbol{j} = \sigma\boldsymbol{E}$, we attain expressions for conductivity tensor, σ.

$$\sigma = \begin{pmatrix} \sigma_{xx} & \sigma_{xy} \\ \sigma_{yx} & \sigma_{yy} \end{pmatrix} = \frac{\sigma_0}{(1 + \omega_c^2 \tau_{tr}^2)} \begin{pmatrix} 1 & -\omega_c \tau_{tr} \\ \omega_c \tau_{tr} & 1 \end{pmatrix} \qquad (2.10a)$$

where $\sigma_0 = en\mu$ is the DC conductivity at zero magnetic field. At high magnetic field when condition $\omega_c \tau_{tr} \gg 1$ is satisfied, Eq. (2.10a) will become:

$$\sigma = \frac{en}{B} \begin{pmatrix} 1/(\mu B) & -1 \\ 1 & 1/(\mu B) \end{pmatrix} \qquad (2.10b)$$

Thus the resistivity tensor, ρ, is given by:

$$\rho = \begin{pmatrix} \rho_{xx} & \rho_{xy} \\ \rho_{yx} & \rho_{yy} \end{pmatrix} = \frac{1}{|\sigma|} \begin{pmatrix} \sigma_{xx} & \sigma_{yx} \\ \sigma_{xy} & \sigma_{yy} \end{pmatrix} = \begin{pmatrix} \dfrac{1}{\sigma_0} & \dfrac{B}{en} \\ -\dfrac{B}{en} & \dfrac{1}{\sigma_0} \end{pmatrix} \qquad (2.11)$$

The off-diagonal elements of the resistivity tensor give the Hall resistance.

2.3.2. Quantum transport in 2DHG

Consider applying a crossed static electric field, $\boldsymbol{E}$, and magnetic field, $\boldsymbol{B}$, on an ideal 2DEG, with the electric field on x direction and magnetic field on z direction. Ideal 2DEG means only electric potential, eEx, and vector potential exist in the system. Under Landau gauge, the Schrödinger equation of the electron in 2DEG is:

$$\left\{ \frac{1}{2m} [p_x^2 + (p_y - eBx)^2] - eEx \right\} \Psi(x,y) = \varepsilon \Psi(x,y) \qquad (2.12)$$

As the Hamiltonian is independent on y, the solution still has the same form as Eq. (2.2).

Substitute Eq. (2.2) into Eq. (2.12), after simplified manipulations, we have equation for $u(x)$:

$$\left[-\frac{\hbar^2}{2m}\frac{d^2}{dx^2} + \frac{1}{2}m\omega_c^2(x - X_k)^2 \right] u(x) = \varepsilon' u(x) \tag{2.13}$$

where $X_k = l_0^2 k_y + v_d/\omega_c$ is again the center of cyclotron orbit moving with drift velocity $v_d = E/B$ and $\varepsilon' = \varepsilon + eEX_k - mv_d^2/2$. Therefore $u(x)$ has the same form as Eq. (2.5) and energy levels are given by:

$$\varepsilon_{nk_y} = \left(n - \frac{1}{2}\right)\hbar\omega_c - eEX_k + \frac{1}{2}mv_d^2 \tag{2.14}$$

Eq. (2.14) indicates that the degeneracy on k_y is lifted by applying static electric field. Suppose the Fermi level lies on Landau level n. Then using the orthogonality of the one-dimensional harmonic oscillator, we attain the velocities in x and y directions for electrons at the Fermi level:

$$v_x = \frac{1}{m}\iint dxdy[\phi_n(x - X_k)e^{ik_y y}]^\dagger p_x \phi_n(x - X_k)e^{ik_y y} = 0$$

$$v_y = \frac{1}{m}\iint dxdy[\phi_n(x - X_k)e^{ik_y y}]^\dagger (p_y - eBx)\phi_n(x - X_k)e^{ik_y y} = -v_d = -\frac{E}{B}$$

Again, with current density $\boldsymbol{j} = -en\boldsymbol{v}$ and relation $\boldsymbol{j} = \sigma\boldsymbol{E}$ and $\sigma_{xy} = -\sigma_{yx}$, we attain the conductivity tensor:

$$\sigma = \begin{pmatrix} 0 & -en/B \\ en/B & 0 \end{pmatrix} \tag{2.15}$$

Thus the resistance tensor follows:

$$\rho = \begin{pmatrix} 0 & B/en \\ -B/en & 0 \end{pmatrix} \tag{2.16}$$

These results of conductivity and resistivity tensors are different with those in classical transport cases. Let's check the off-diagonal elements of the tensors first. From Eq (2.11)

and (2.16), the off-diagonal resistivity is the same, giving the exact Hall resistivity. When Landau levels are totally resolved, condition $\omega_c \tau_{tr} \gg 1$ will be satisfied. Under this condition, consistence is also found in off-diagonal conductivity in Eq. (2.10b) and For the diagonal conductivity and resistivity, the difference is obvious. In quantum transport, an ideal 2DEG under strong magnetic field has zero diagonal conductivity and resistivity so that there is only pure Hall current, orthogonal to external electric field, in the system.

But in the real 2DEG system, scattering potential, V, is always present. Normally, V is much smaller than the external potential eEx so that we can treat V as a perturbation. Although it was reported [20] that up to second order in V, there is no change on the Hall conductivity, the presence of V does lead to nonzero diagonal conductivity as well as diagonal resistivity. More details will be provided in following sections.

Another important property of quantum transport to be emphasized is that even when diagonal conductivity is nonzero due to scattering, it is still much smaller than the off-diagonal one, that is $\sigma_{xy} \gg \sigma_{xx}, \sigma_{yy}$, which will therefore lead:

$$\rho_{xx} = \frac{\sigma_{xx}}{\sigma_{xx}\sigma_{yy} + \sigma_{xy}^2} \approx \frac{\sigma_{xx}}{\sigma_{xy}^2} \qquad (2.17)$$

This fact that diagonal resistivity is directly proportional to diagonal conductivity is contrary to common idea on the reverse relation between resistivity and conductivity at weak or zero magnetic field.

2.4. Shubnikov de Haas (SdH) oscillations

Typical SdH oscillations in magnetoresistance in a 2DEG at $T = 0.3$ K are shown in Fig. 2.3 [21].
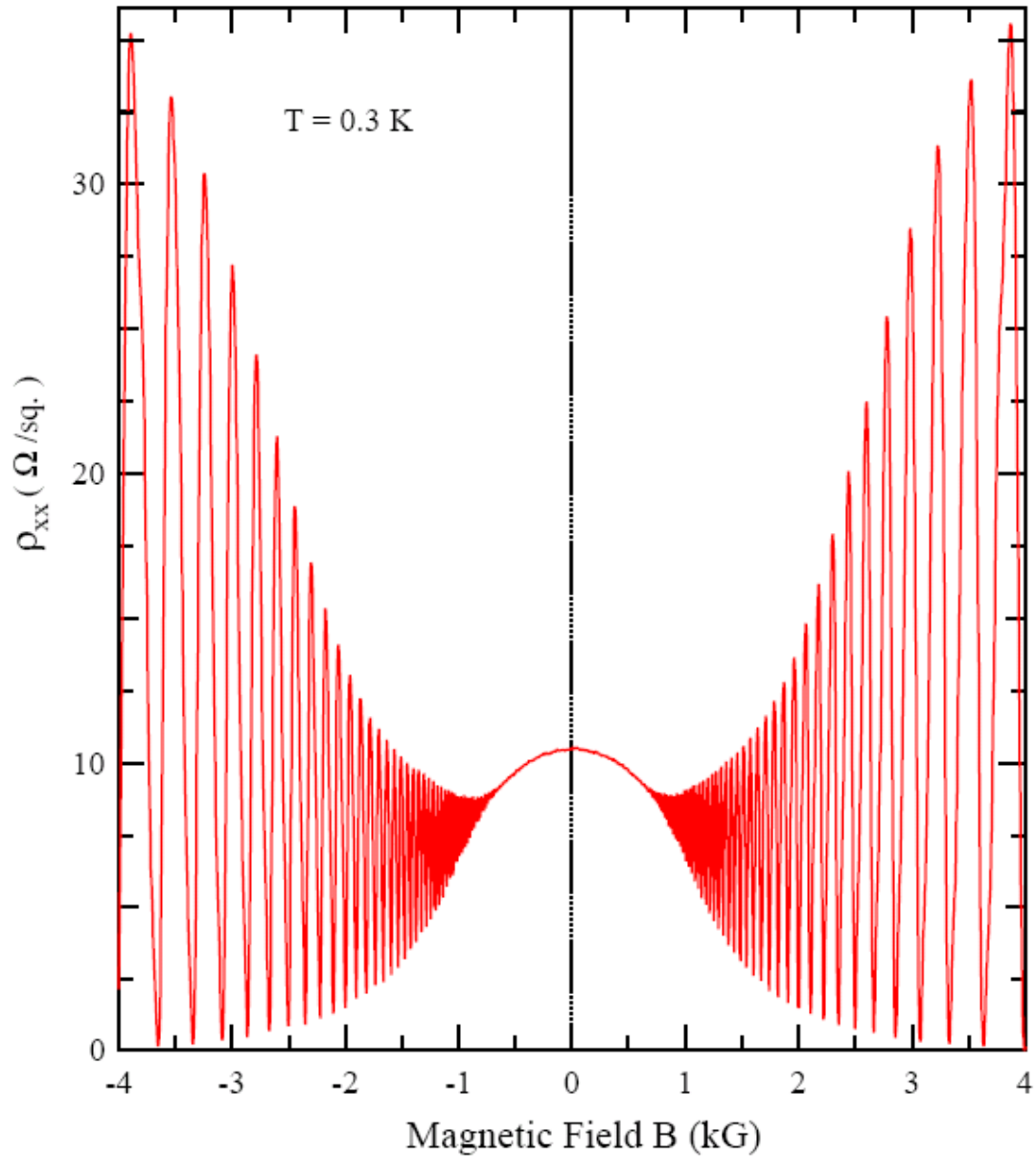
Fig. 0.3 Typical SdH oscillations observed in a 2DEG in GaAs-Al$_{0.3}$Ga$_{0.7}$As heterostructure with density $n_e = 2.1 \times 10^{11} \text{cm}^{-2}$ and mobility $\mu \approx 3.0 \times 10^6$ cm^2/Vs. (figure adapted from Ref. 21)

At low temperature ($T < 4\ K$), elastic scattering by impurities is dominant. With Fermi golden rule, the transition probability $W_{\alpha\alpha'}$ is given by:

$$W_{\alpha\alpha'} = \frac{2\pi}{\hbar}|\langle\alpha|V|\alpha'\rangle|^2\delta(\varepsilon_\alpha - \varepsilon_{\alpha'}) \tag{2.18}$$

where V is scattering potential, α, α' represent initial and final states of scattering with energies $\varepsilon_\alpha, \varepsilon_{\alpha'}$ respectively. Thus the longitudinal conductivity resulting from the migration of the center of cyclotron orbits is given by the Titeica formula [22]:

$$\sigma_{xx} = \frac{1}{2}e^2n\sum_{\alpha\alpha'} W_{\alpha\alpha'\cdot}(X - X')^2\left(-\frac{\partial f_\alpha}{\partial\varepsilon_\alpha}\right) \tag{2.19}$$

where X, X' are centers of cyclotrons of initial and final states and $f_\alpha = 1/[e^{(\varepsilon_\alpha - E_F)/k_BT} - 1]$ is the Fermi distribution of electrons. Under relaxation time approximation, the resistivity can be given by:

$$\rho_{xx} = \rho_0\left[1 + \sum_{r=1}^{\infty} b_r\cos\left(\frac{2\pi E_F}{\hbar\omega_c}r - \frac{\pi}{4}\right)\right] \tag{2.20}$$

where

$$b_r = \frac{(-1)^r}{r^{1/2}}\left(\frac{\hbar\omega_c}{2E_F}\right)^{1/2}\frac{2\pi^2rk_BT/\hbar\omega_c}{\sinh(2\pi^2r\,k_BT/\hbar\omega_c)}\cos\left(\frac{gm^*}{2m_e}\pi r\right)e^{-2\pi\Gamma r/\hbar\omega_c} \tag{2.21}$$

where g is the effective g-factor and m^* is the effective mass of 2DEG. The oscillatory behavior of longitudinal resistivity in $1/B$ results from the fact that the density of states oscillates with filling factor, v, as shown in Fig. 2.2. The frequency of the SdH oscillation in $1/B$ is given by:

$$f = s\frac{h}{e}n_{2D} \tag{2.22}$$

where $s = 1/2$ if spin levels in the same Landau level are not resolved, otherwise $s = 1$.

2.5. Integer Quantum Hall Effect

At higher magnetic field, diagonal and off-diagonal resistance will show the integer quantum Hall effect, first observed by K. von Klitzing, G. Dorda and M. Pepper [1], in which Hall resistance exhibits a series of plateaus with precise values of $h/(e^2 v)$ and longitudinal resistance is almost zero when filling factor, v, is an integer; that is, when the Fermi level is located midway between two adjacent Landau levels. Typical traces of the integer quantum Hall effect is shown in Fig. 2.4. The integer quantum Hall effect can be understood in the following way. At high magnetic field, due to presence of impurities in 2DEG system, most of states of electrons are localized except the states at the center of Landau levels, i.e. only the center of each Landau level contains extended states; the rest are localized states, and the energy span between two adjacent extended states area is the mobility gap, as shown in Fig. 2.5. During transport, only the extended states contribute to conduction. When the Fermi level locates inside the mobility gap, all states around the Fermi level are localized and play no part in conduction. Let's consider a 2DEG in a Hall bar as shown in Fig. 2.6. A strong magnetic field is applied perpendicular to the 2DEG and a negative voltage bias, V_1, is applied to terminal-1 so that electron flow will leave terminal-1 and move to terminal-2. At a specific magnetic field such that Fermi level is at the middle of mobility gap, all states inside the bulk 2DEG are localized and electrons only can travel through edge sates. Due to boundary confinement, the Landau level will bend up rapidly at vicinity of Hall bar edge, as shown in Fig. 2.7. The number of edge state at the Fermi level is the number of occupied Landau levels, that is, the filling factor, v. In a four-terminal measurement, terminal-3, 4, 5 and 6 will carry no net current. Under

applied voltage V_1, the Fermi level at terminal-1 is raised by $-eV_1$ so that electron leave terminal-1 and move into edge states.
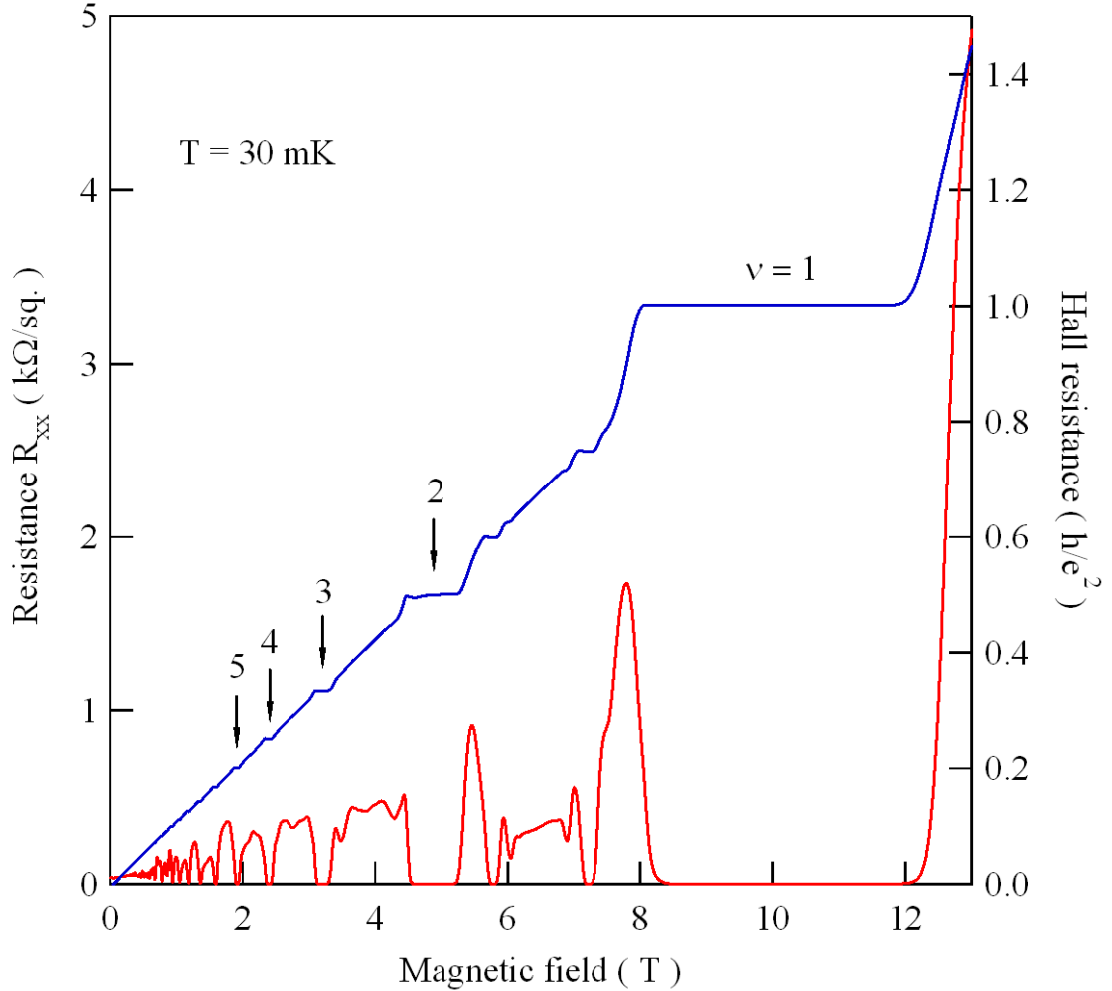
Fig. 0.4 Integer Quantum Hall Effects in a 2DHG, Hall resistance, R_{xy} exhibiting a series of plateaus at integer filling factors while longitudinal resistance, R_{xx} having vanishing values.

Suppose the edge states propagate along counter clockwise, as shown in Fig. 2.6. Thus electrons leaving terminal-1 will travel to terminal-3. As terminal-3 carries no net current, the same amount of electrons shall leave terminal-3 too. This will require the Fermi levelat terminal-3 also to be raised by $-eV_1$; that is, $V_1 = V_3$. In the same way,
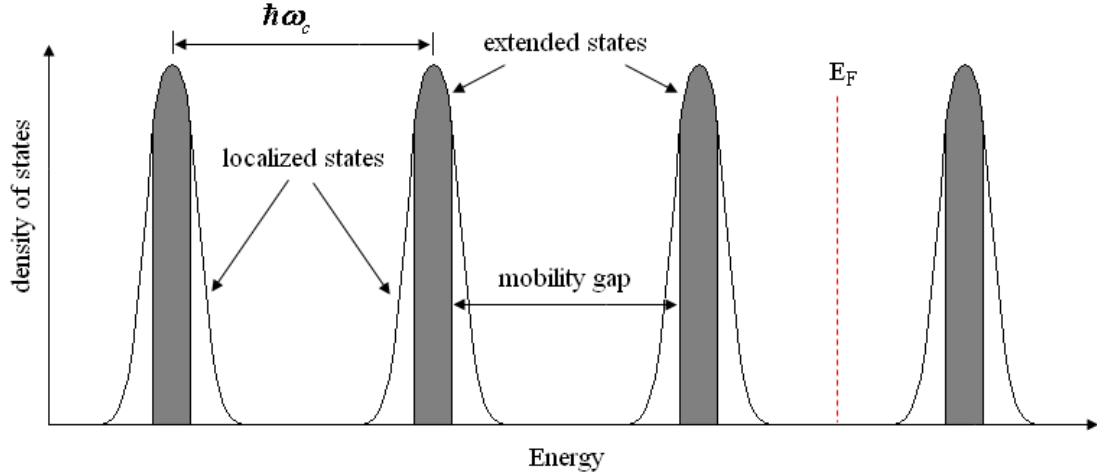
Fig. 0.5 Extended states and localized stated distributed in diagram of density of states of Landau levels.

we can prove $V_3 = V_5$ and $V_2 = V_4 = V_6$. And current carried by each edge state is $-(e^2/h)(V_1 - V_2)$, thus a total current $I = -v(e^2/h)(V_1 - V_2)$ leaves terminal-2 to terminal-1. Therefore the longitudinal and Hall resistances are given by:

$$R_{xx} = (V_5 - V_3)/I = 0$$

$$R_{xy} = \frac{V_3 - V_4}{I} = \frac{V_1 - V_2}{-v(e^2/h)(V_1 - V_2)} = -\frac{1}{v}\frac{h}{e^2}$$

which give the vanishing longitudinal resistance and quantized Hall resistance. When we sweep magnetic field, the Fermi level will move inside mobility gap. The conductance, as well as resistance, will not change because the localized states have no contribution to conduction. Thus plateaus will form in Hall resistance and their width is determined by the width of the mobility gap.
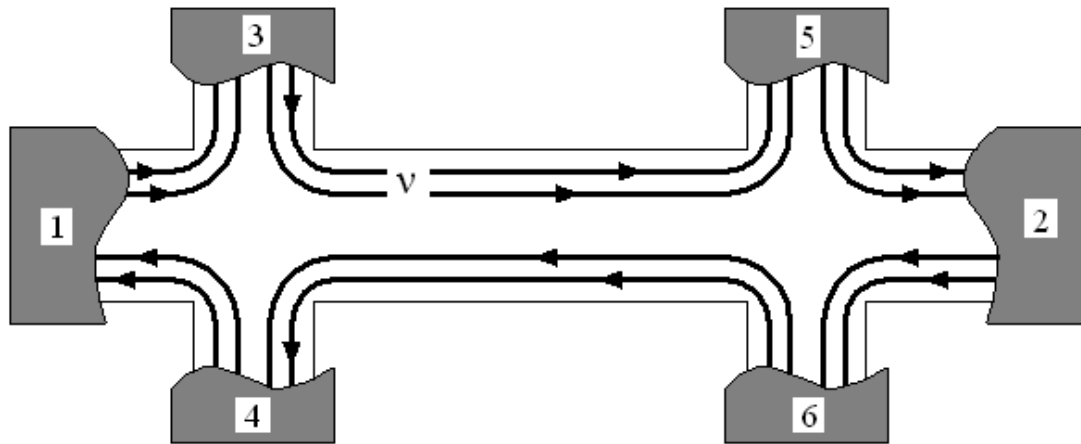
Fig. 0.6 A Hall bar with 6 terminals under strong magnetic field, showing propagation of edge states.
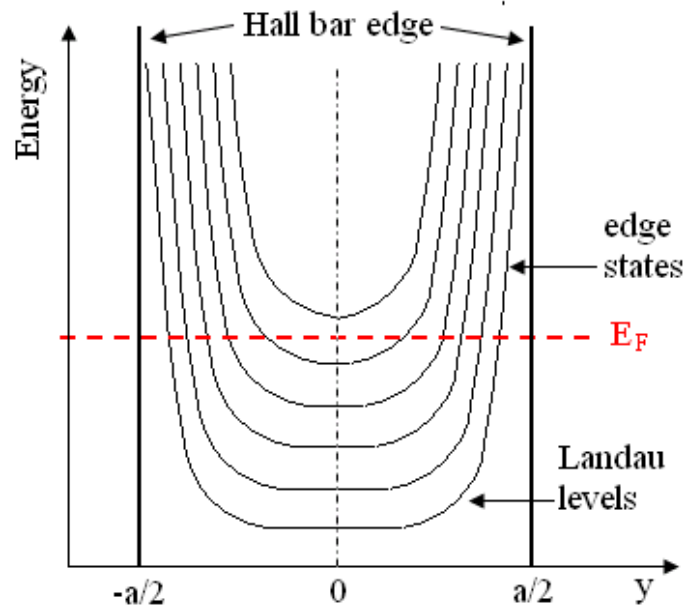
Fig. 0.7 Diagram of edge states in Hall bar with width a. It is clear that number of edge states at the Fermi level is equal to the number of occupied Landau levels.

2.6. Geometric Resonance

To study electron scattering on 2DEG, one-dimensional [4-6] and two-dimensional artificial periodic scatterers were introduced. New magnetoresistance oscillations, namely geometric resonances (GR) were observed at low magnetic field in these two cases. For a 1D periodic modulation potential, the typical oscillations in longitudinal resistances are shown in Fig. 2.8. [4], in which resistivities perpendicular, $\rho_\perp$, and parallel, $\rho_\parallel$ to modulation oscillate out of phase and magnitude of oscillations of $\rho_\perp$ is
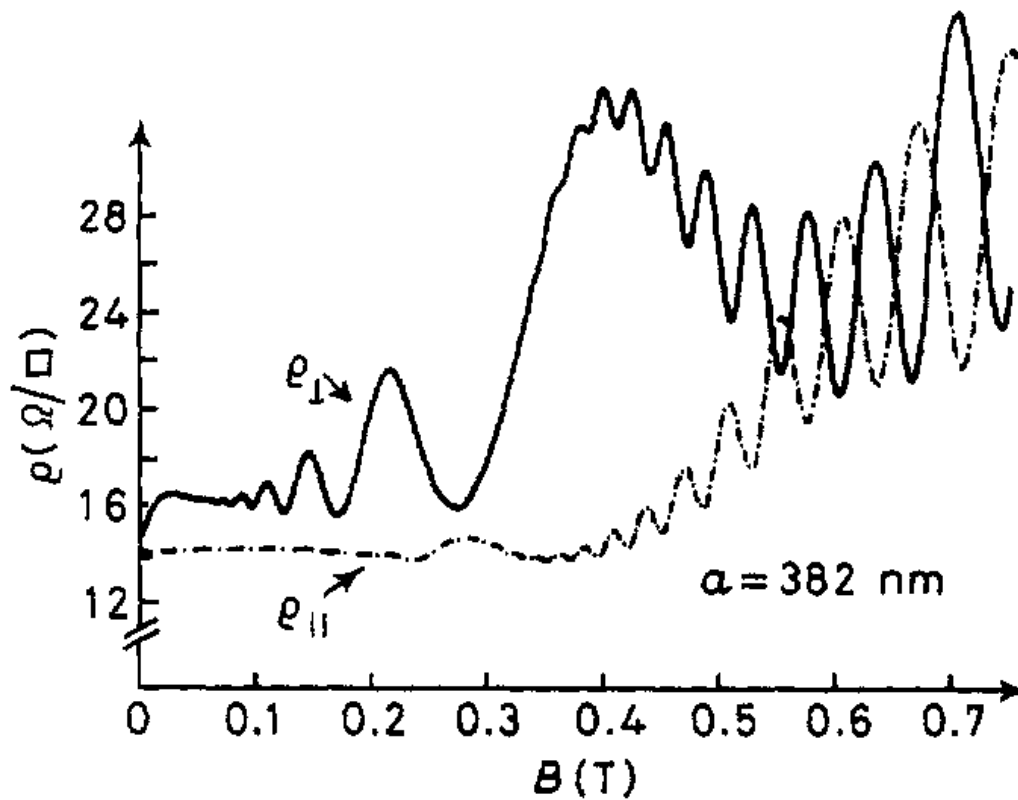
Fig. 0.8 Magnetoreisitance trace of longitudinal resistivity parallel, $\rho_\parallel$, and perpendicular, $\rho_\perp$, to the one dimensional modulations at $T = 2.2$ K of 2DEG with density of $3.16 \times 10^{11} \text{cm}^{-2}$ and mobility of $1.3 \times 10^6 \text{cm}^2$/Vs. Oscillations of geometric resonance are clearly shown. (figure adapted from Ref. 4)

much larger, more than one order, than that of $\rho_\parallel$. The extrema in oscillations of $\rho_\perp$ arise when radius of cyclotron orbit, $R_c = l_B^2 k_F$, is a multiple of the lattice period a such that

$$2R_c = (m + \phi)a, \qquad m = 1, 2, ... \tag{2.23}$$

where ϕ is the phase shift having different values for minima and maxima. In a semiclassical picture, a drift of a guiding center along the 1D modulation [23] gives rise to the oscillations of $\rho_\perp$. Quantum-mechanically, band conduction, resulting from the diffusion contribution, dominates $\rho_\perp$ so that an oscillatory dependence of bandwidth of the modulation-broadened Landau level gives rise to the oscillations [5, 6, 24, 25]. And migration of cyclotron orbit center due to impurities scattering, collision contribution, results in $\rho_\parallel$. This migration is determined by DOS so that an oscillatory DOS due to modulated potential will give rise to oscillations in $\rho_\parallel$ [24, 25].

In 2D modulations, an antidot lattice, the oscillations in longitudinal resistance, GR, are shown in Fig. 2.9 [7]. This GR also stems from a commensurability effect between cyclotron radius and period of potential lattice, a. The first resistance peak occurs at $2R_c \cong a$. After the discovery, further experiments were done in exploring the dependence of GR on the structure of antidot lattices, such as on rectangular lattices with different period [26-30], hexagonal lattice [31], and triangular lattice [13, 32, 33]. Extensive theoretical works were done on understanding this GR [34-45].

Two different semiclassical models were applied to the GR for low and high qualities 2DEG respectively. In low mobility 2DEG with 2D modulation, the GR is caused by a pinned orbit mechanism [7, 36]. This model says when diameter of cyclotron orbit is commensurate with period of antidot lattice, the orbit will be pinned around the antidot,
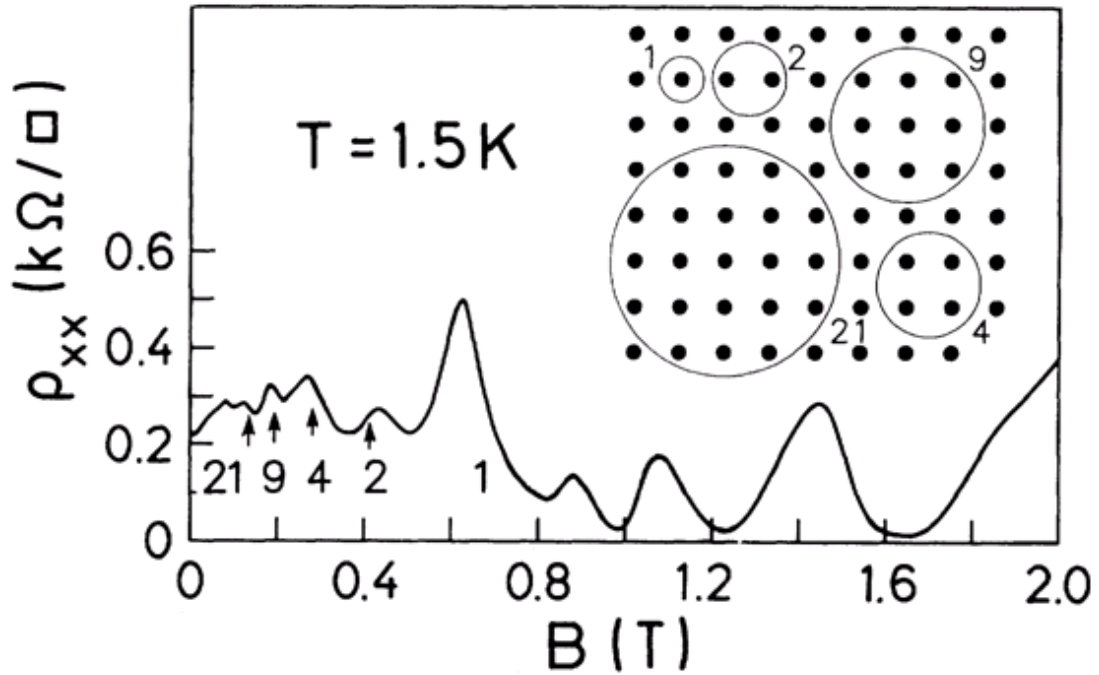
Fig. 0.9 Geometric resonance on a 2DEG with a two dimensional rectangular modulations, rectangular antidot having period a = 300 nm at T = 1.5 K. Inset shows pinned orbits corresponding to resistance peaks. Number indicates number of antidots enclosed by a pinned orbit. (figure adapted from Ref. 7)

as shown in inset of Fig. 2.9, and will not respond to electric field so that the electron will have no contribution to conductance; thereby an increase of resistance will be observed. While in high quality 2DEG situation, a mechanism of runaway orbit of delocalized electrons contributes to the oscillations [35, 39, 40, 43]. When the condition of commensurability between the diameter of cyclotron orbit and period of modulation is satisfied, the orbits will experience more scatterings so that they will be skipping from one antidot to its neighboring antidot, which will cause an increase in conductance as well as in resistance. Typical diagrams of pinned orbits and runaway orbits are shown in Fig. 2.10. Quantum-mechanically, the presence of 2D modulation lifts the degeneracy of

LLs and leads to an oscillatory width of Landau bands and a internal self-similar Hofstadter-type subband structures [37, 38]. This internal subband structure gives rise to an oscillatory behavior of band conductivity, thereby resulting in GR.
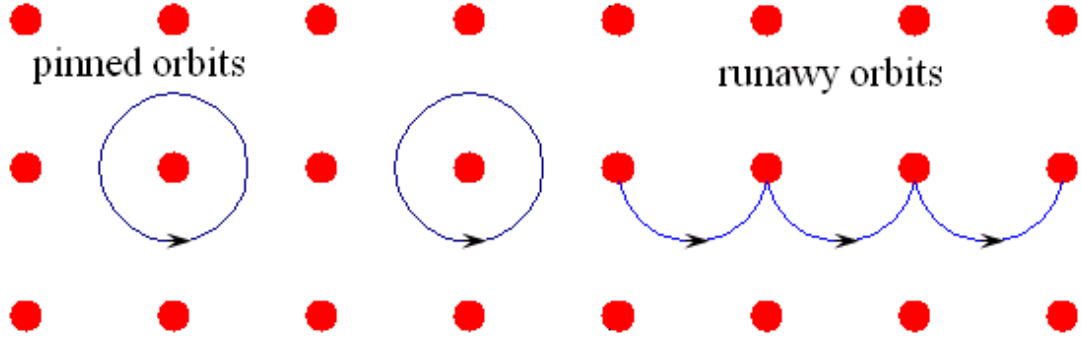
Fig. 0.10 Schematic diagrams of pinned orbits and runaway orbits.

2.7. Microwave Induced Resistance Oscillation and Zero Resistance State

When a high mobility 2DEG is exposed to microwave (MW) irradiation, the microwave photoresistance will show a giant amplitude oscillations [8, 9], namely microwave induced resistance oscillations (MIRO), whose extrema are controlled by the ratio between the MW frequency, ω_{MW}, and cyclotron frequency, ω_c,:

$$\epsilon = \frac{\omega_{MW}}{\omega_c} = \begin{cases} j & max \\ j+1 & min \end{cases} \quad j = 1,2,\ldots \tag{2.24}$$

where j is the difference between the indices of LLs. A typical MIRO trace is shown in Fig. 2.11. These remarkable photoresistance oscillations can be understood in a simple semiclassical picture. In a 2DEG, the presence of short-range scattering, resulting from interface roughness and residual impurities in the spacer, excites transitions between multiple LLs, associated with a finite momentum transfer, $\Delta q = 2k_F$, with k_F the
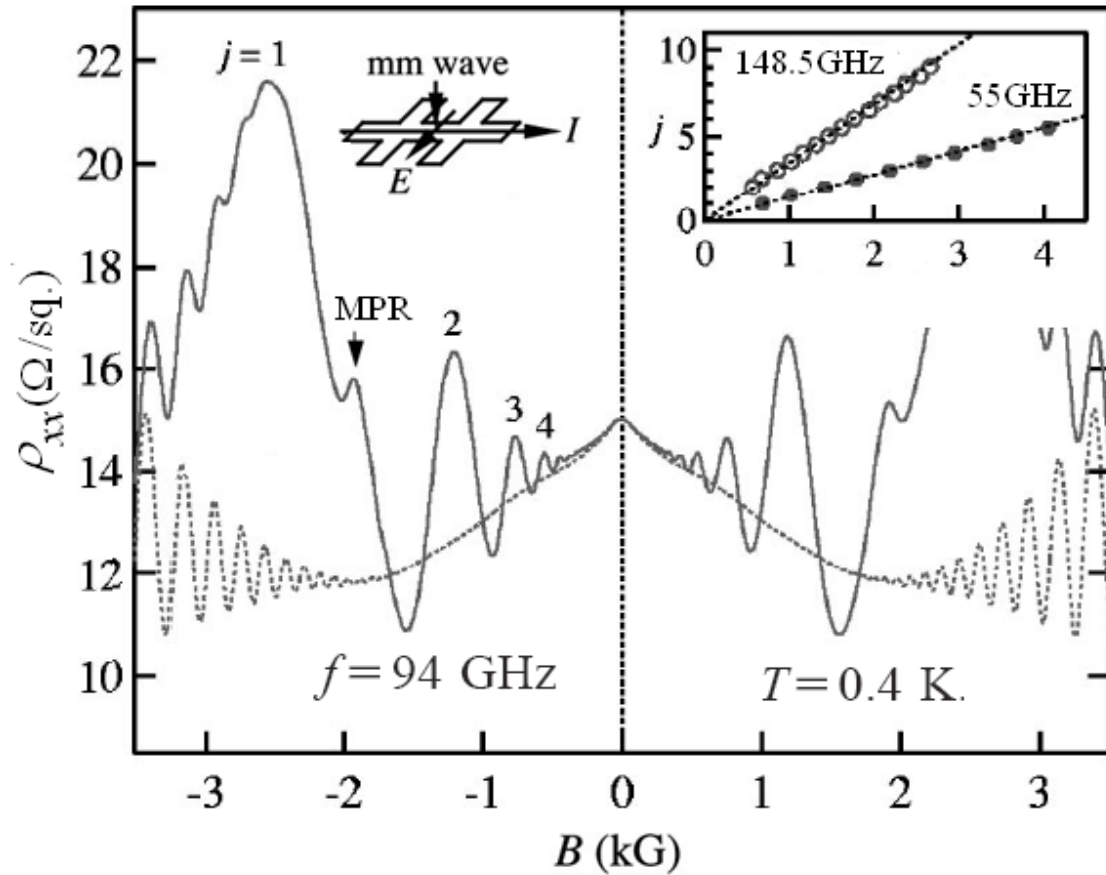
Fig. 0.11 Microwave induced resistance oscillations observed in a 2DEG with mobility $\mu \approx 3.0 \times 10^6 cm^2/Vs$ under MW f = 94 GHz illumination at T = 0.4 K (solid line) and magnetoresistance without MW illumination is shown by dotted line. The left inset shows Faraday geometry for experimental setup and right inset shows a plot of the multiply index j vs $1/B$ for f = 55 GHz and f = 148.5 GHz to reveal an electron effective mass $m^* \approx 0.068 m_e$. The small arrow marks magnetoplasmon resonance signal. (figure adapted from Ref. 8)

electron Fermi wave vector. This momentum transfer is equivalent to a jump of an electron cyclotron orbit center along the transverse direction so that a conductivity peak can be observed. Qualitatively, based on the toy radiation induced scattering model [46, 47] and an assumption of uniform probability of photon-assisted scattering for all harmonics, MW induced photoresistance can be calculated by formula [48]:

23

$$\Delta R_{xx}^\omega(B) = A \int d\varepsilon [n_F(\varepsilon) - n_F(\varepsilon + \hbar\omega_c)] v(\varepsilon)\, \partial_\varepsilon v(\varepsilon + \hbar\omega_c) \tag{2.25}$$

where A is a field independent coefficient, $n_F(\varepsilon) = 1/\{1 + exp[(\varepsilon - \varepsilon_F)/k_B T]\}$ is the Fermi distribution function and

$$v(\varepsilon) = \sum_{i=0}^{\infty} \frac{eB}{\pi^2 \hbar \Gamma} \cdot \frac{\Gamma^2}{\Gamma^2 + [\varepsilon - (i + 1/2)\hbar\omega_c]^2} \tag{2.26}$$

is the density of states with Γ the width of the LL.

Additionally, a magnetoplasmon (MP) resonance signal is also shown in Fig. 2.10, marked by a small arrow. MP resonance occurs at a magnetic field satisfying condition:

$$\omega_{MW}^2 = \omega_p^2 + \omega_c^2 \tag{2.27}$$

where ω_{MW} is the MW frequency, ω_c is the cyclotron frequency, and ω_p is the 2D plasmon frequency, which is given by [49, 50]:

$$\omega_p^2 = \frac{n_e e^2 k}{2\epsilon\epsilon_0 m^*} \tag{2.28}$$

where wave vector $k = \pi/w$ with w the lateral width of 2DEG and ϵ is effective dielectric constant of the material.

When a higher mobility 2DEG is exposed to sufficiently strong MW irradiation, MIRO will develop into a novel zero-resistance-state (ZRS) [10, 11], as shown in Fig. 2.12, at which transverse resistance vanishes within experimental uncertainty while Hall resistance remains at its classical value. A later measurement of photoconductance in the Corbino geometry proved the existence of zero-conductance-state (ZCS) [12] as well.
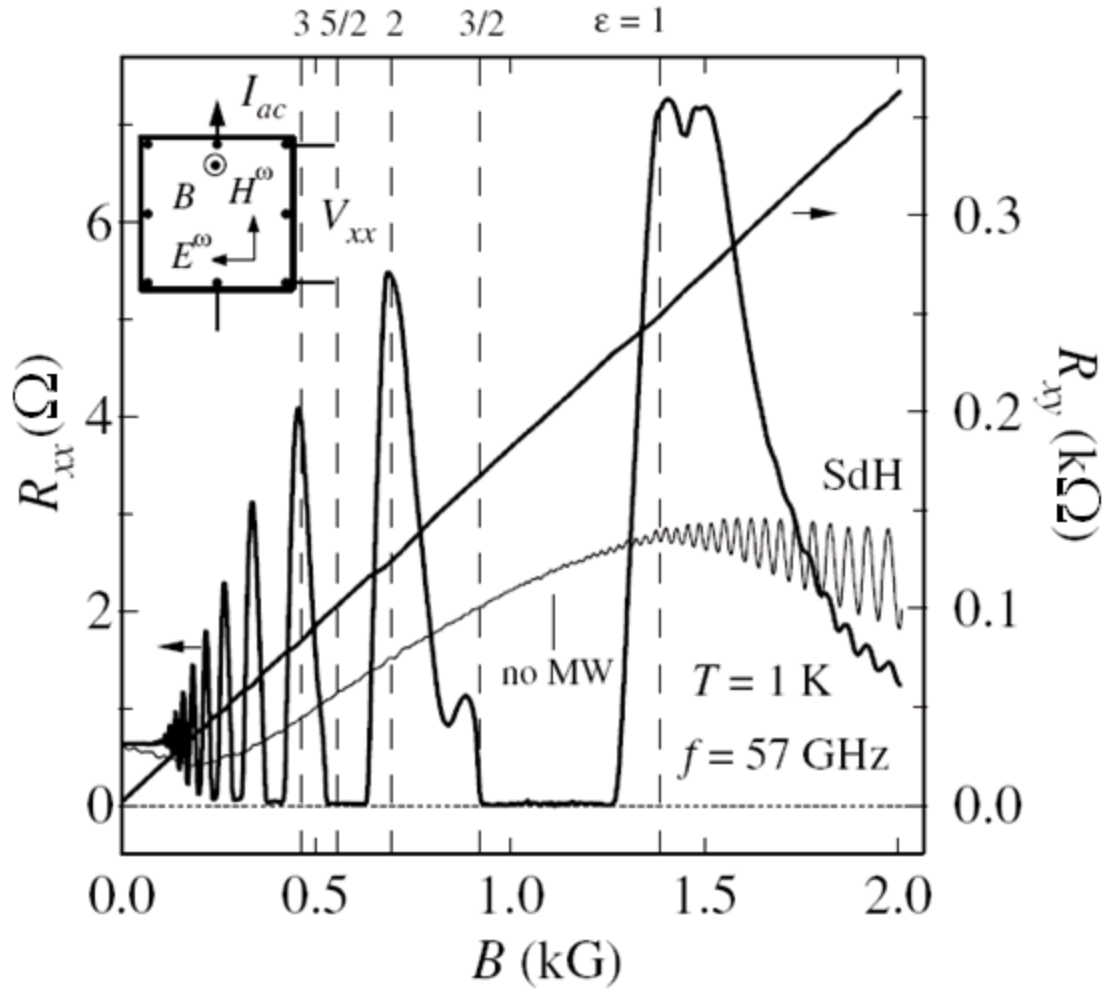
Fig. 0.12 Longitudinal resistance R_{xx} (left axis) shows vanishing resistance values, zero-resistance-state, under MW (f = 57 GHz) illumination at T = 1 K and Hall resistance R_{xy} (right axis) has classical value (thick line). And R_{xx} without MW illumination is shown by thin line. Vertical dashed lines indicate values of ε calculated by Eq. (2.24). The inset depicts the layout of experimental setup, Faraday geometry. (figure adapted from Ref. 11)

After they were discovered, these novel ZRS and ZCS stimulated intense experimental attentions. Refs. [13, 48, 51-71] explored ZRS from various angles, such as experiments on phase shift analysis of ZRS [54, 57], effect of multiple photons process [64, 65] and MW polarization [60], interactions with edge-magnetoplasmon [53, 70, 71],

and influence of presence of in-plane magnetic field [59, 63] or 2D spatial modulation [13] or DC bias [62, 68, 69].

At the same time, many theoretical works [14, 46, 72-111] have been done on understanding ZRS. Works have been done on exploring effects of MW polarization [108, 111], procedure involving multiple photons [88, 104], and the influence of the induction at a 1D or 2D modulation [94, 95, 97]. Most other works proposed mechanisms to explain this novel phenomenon. It was theoretically suggested [14] that high MW irradiation on ultraclean 2DEG would cause absolute negative conductivity (ANC) whose instability would lead to formation of electron current domains. Across these domains, transverse voltage drop is zero, resulting in a zero measured transverse resistance. Two microscopic mechanisms may be responsible for ANC. One is the so-called "displacement" mechanism [42, 46, 78, 79, 81, 82, 86, 87, 89, 91, 96, 101, 105, 107, 110], in which MW photon-assisted impurity scattering triggers transitions between different LLs and reduces the conductivity. When the scattering is strong enough, it will drive conductivity to zero or even to absolute negative values. Another mechanism is "electron distribution function" mechanism [72, 83, 94, 95, 103], in which ANC arises from MW-induced non-equilibrium oscillation of electron distribution function in the density of states (DOS). These two models can explain some aspects of the effect and reproduce the observed period, phase and magnetic field damping. However, so far, the exact microscopic nature of ZRS has not been conclusively established.

Chapter Three Quantum Transport in 2DEG with Triangular Antidot Lattice

3.1. Geometric Resonance in high mobility 2DEG with triangular antidot lattice

In our experiments, a 2D triangular antidot lattice was patterned on an ultraclean 2DEG, and very sharp GR oscillations peaks were resolved due to high mobility of 2DEG after introduction of antidot lattice.

The 2DEG is cleaved from a high-mobility GaAs/$Al_{0.3}Ga_{0.7}As$ heterostructure wafer
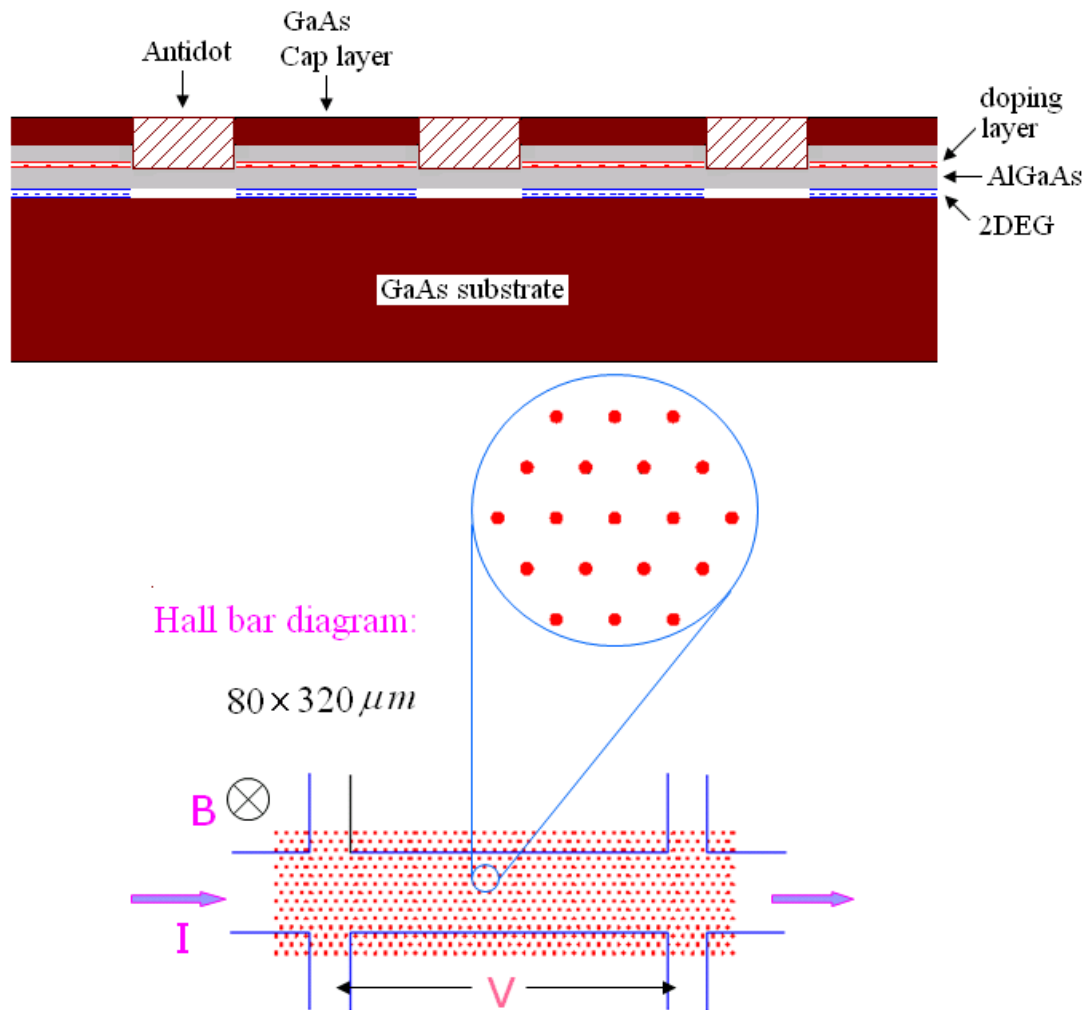
Fig. 0.1 Diagrams of cross section of sample and Hall bar with triangular antidot lattice

grown by molecular beam epitaxy, with a $T = 0.3$ K mobility $\mu \approx 1 \times 10^7 \, cm^2/Vs$ before

the antidot lattice is patterned. An 80-μm-wide, 320-μm-long Hall bar was first defined

on the sample by optical lithography and wet etching. Then a triangular antidot lattice,

with period of $a = 1500$ nm and dot diameter of $d = 300$ nm, was patterned on the Hall

bar by e-beam lithography and reactive ion etching. The detailed procedure of the

fabrication can be found in Appendix A4. The diagrams of sample cross section and Hall

bar with antidot lattice are shown in Fig. 3.1 and SEM image of sample surface after

introduction of antidot lattice is shown in Fig. 3.2. After the lithographical processing,
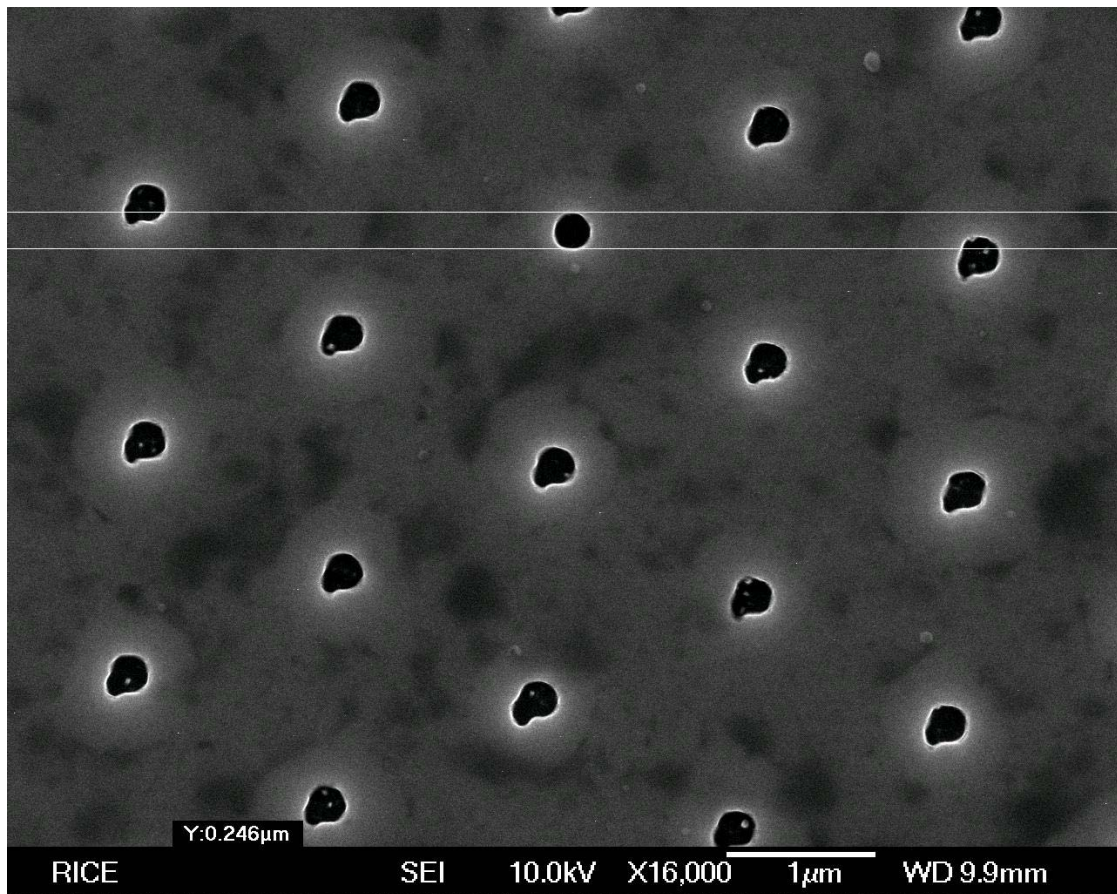
Fig. 0.2 Image of triangular antidot lattice with $a = 1500$ nm and $d = 300$ nm.

the 2DEG has an electron density $n = 2.83 \times 10^{11} \text{cm}^{-2}$ and a zero field mobility $\mu = 2.5 \times 10^6 \text{cm}^2/\text{Vs}$. The electron density was calculated from period of SdH oscillations and mobility was calculated from zero field resistivity. Such parameters were obtained after a brief illumination from a red light-emitting diode at temperature $T = 4$ K. Note that the introduction of an antidot lattice reduced mobility fourfold. However, the transport mean free path corresponding to this mobility, $l = m^* v_F \mu / e$, where m^* is electron effective mass and v_F is the Fermi velocity, is equal to 21.9 μm, exceeding the lattice period a by at least one order. This indicates a much cleaner system than previously reported [7, 30, 32]. Moreover, as the dimension of Hall bar is still much larger than mean free path, we can treat the Hall bar as macroscopic.

Our measurement was performed in a He^3 refrigerator equipped with an 11-T superconducting magnet. The magnetoresistance R_{xx} is measured with standard low frequency lock-in techniques (frequency 23 Hz and excitation current 1 μA). A R_{xx} trace is shown in Fig. 3.3, in which a set of sharp peaks were resolved and are attributed to geometric resonance. Note that in the magnetic field regime of all these peaks, the condition $\omega_c \tau_{tr} > 2\pi$ is satisfied, where τ_{tr} is the intrinsic momentum relaxation time, or transport lifetime, determined by mobility, $\tau_{tr} = \mu m^* / e$, so that a full cyclotron orbit can be completed between two sequential scattering events.

From Fig. 3.3, the observed GR are much sharper than previously reported results [7, 26-33] and up to seven distinct resistance peaks are resolved, attesting to the extraordinary quality of our sample. Remarkably, the GR peaks exhibit an alternating strength in a B sweep, with the "even" peaks (i.e., 2, 4, 6) standing out as compared to
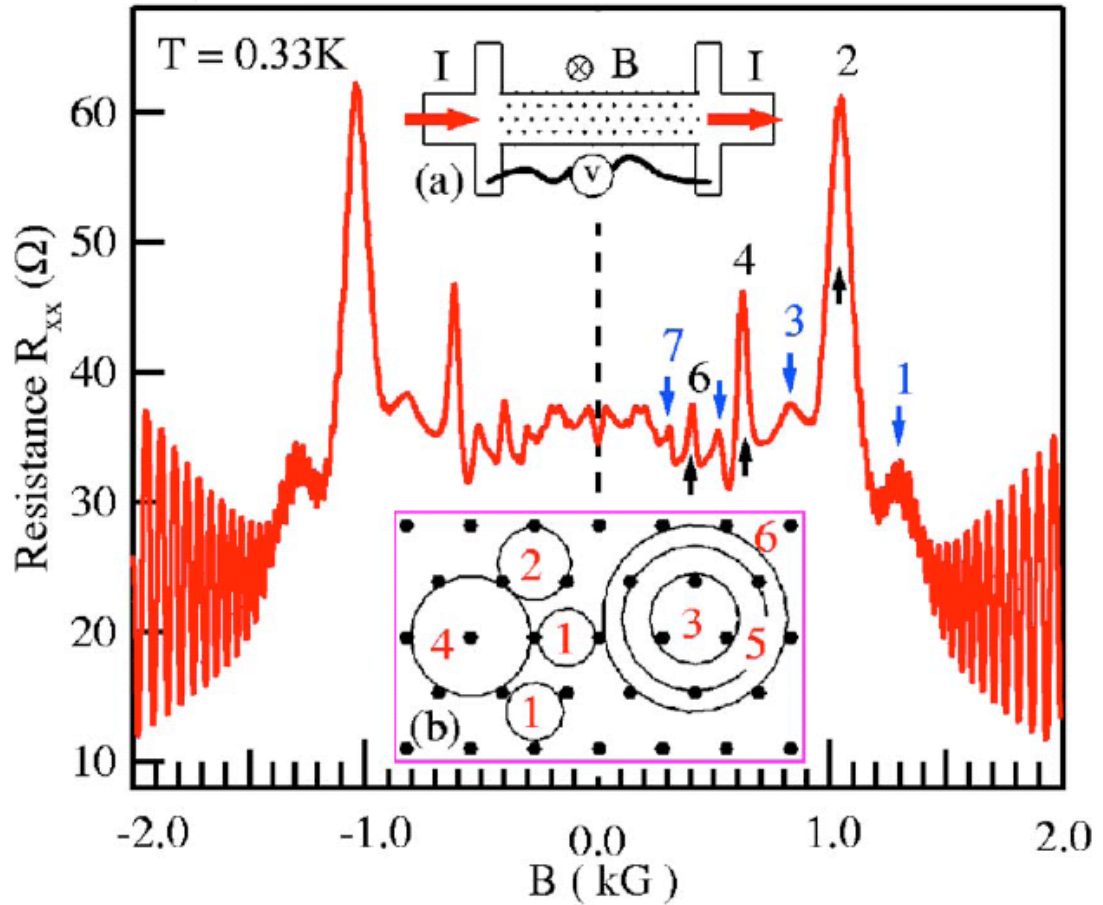
Fig. 0.3 Geometric resonance peaks in low field of resistance R_{xx} on 2DES with triangular antidote lattice (a = 1500nm, d = 300nm) at T = 0.33 K. The peaks from 1 to 7 correspond to ratio R_c/a = 0.45, 0.56, 0.7, 0.94, 1.13, 1.45 and 1.9, respectively, where R_c is the cyclotron radius. Inset (a) is the schematic experimental setup of sample and (b) is a sketch of commensurate orbits corresponding to the peaks.

the "odd" peaks (1, 3, 5, 7). Moreover, the peak position in B does not conform to the set of ratio R_c/a in previous reports [7, 32, 33]. For example, according to Ref. 32, the strongest peak occurs at R_c/a = 0.5 corresponding to a first-pinned semiclassical orbit in a triangular lattice of period a, whereas in Fig. 3.3 the strongest peak (labeled by 2)

occurs at $R_c/a = 0.56$. A similar observation can be found for the second-strongest peak (4 in Fig. 3.3), where R_c/a is found to shift from ~ 0.85 to 0.94 in the present case. The $\sim$ 10% increase of the ratio R_c/a indicates that in high mobility samples, major resistance peaks may not correspond to pinned orbits. Rather, they correspond to those commensurate orbits, which dynamically experience most frequent scattering events, and hence higher conductance. Since in our high-mobility sample the GR occur in the regime $\rho_{xy} \gg \rho_{xx}$, and so $,\sigma_{xx} = \rho_{xx}/(\rho_{xx}^2 + \rho_{xy}^2) \propto \rho_{xx}$, these states give rise to the high-resistance peaks in the Hall bar geometry. This scenario requires that the electron orbit of radius R_c be scattered sequentially by multiple antidots. The orbital dynamics described here is equivalent to the theoretically studied runaway trajectories of delocalized electrons skipping from one antidot to its neighboring antidot [35, 39, 40, 43]. These orbits are drawn schematically in inset (b) of Fig. 3.3. The exceptional sharpness of the peak can be attributed to the small aspect ratio of *d/a* in the present sample.

The temperature-dependent measurements show that the major resistance peaks (2, 4, 6) persist up to above 10 K whereas the minor peaks (1, 3, 5) essentially diminish at $T > 6$ K. From these temperature dependences, we can roughly estimate the height of antidot potential for the electron orbits involved, which is much less than the Fermi energy of the 2DEG (~ 100 K).

To get more understanding on the geometric resonance, temperature dependence of the GR was measured from $T = 0.33$ to 10 K; the results are shown in Fig. 3.4 and 3.5. At $T < 1.5$ K, the amplitude of the GR shows very little change with temperature, while the SdH oscillations dampen quickly with increasing temperature. At $T > 1.5$ K, the GR
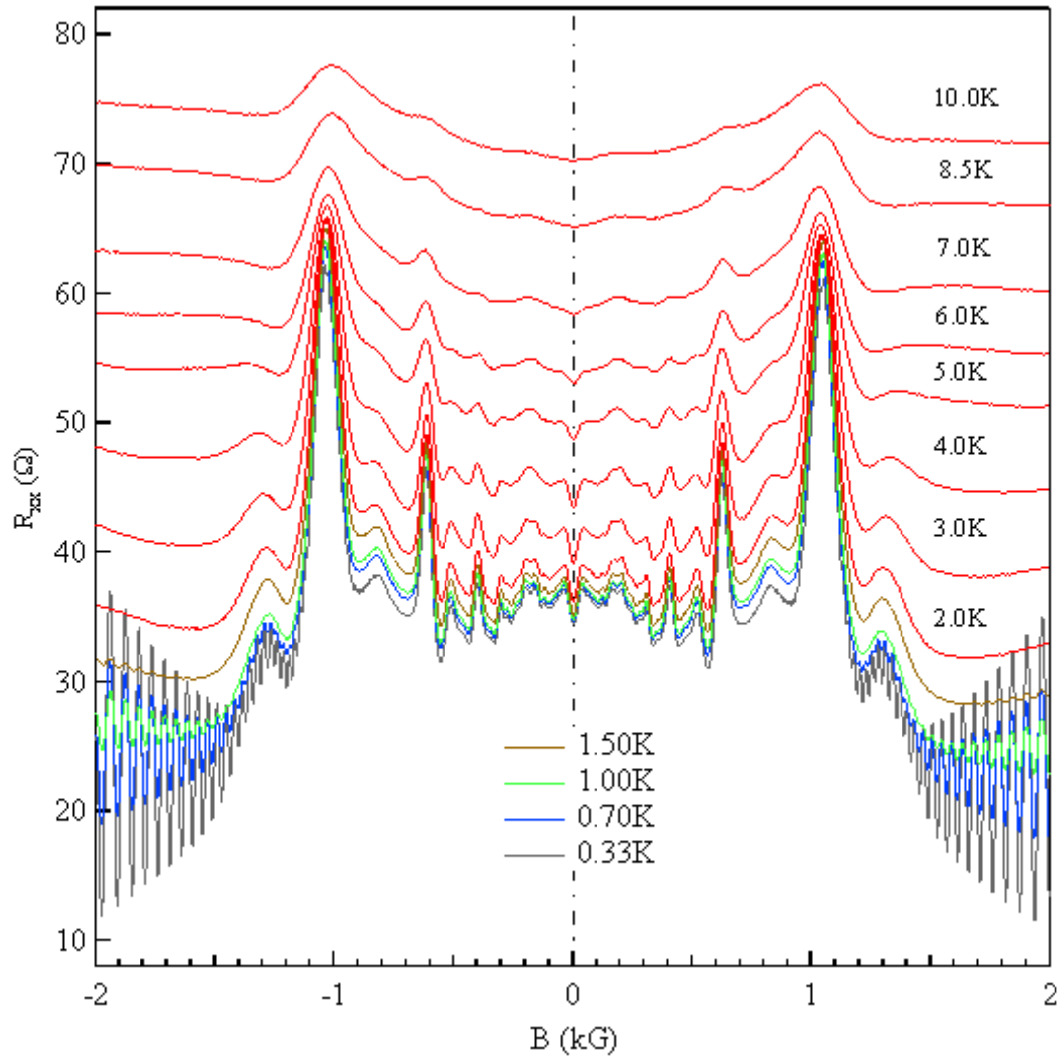
Fig. 0.4 Temperature dependence of geometric resonance for temperature T = 0.33K to 10 K. The GR peaks can persist up to above 10 K.

peaks are greatly damped by raising the temperature. This is clearly depicted in inset (c) of Fig. 3.5. This temperature dependence is consistent with the dominance of thermally excited phonon scattering at this temperature range [112], rather than the mechanism of smearing of Fermi surface [113] taking place at $T > 100$ K in our sample, determined by
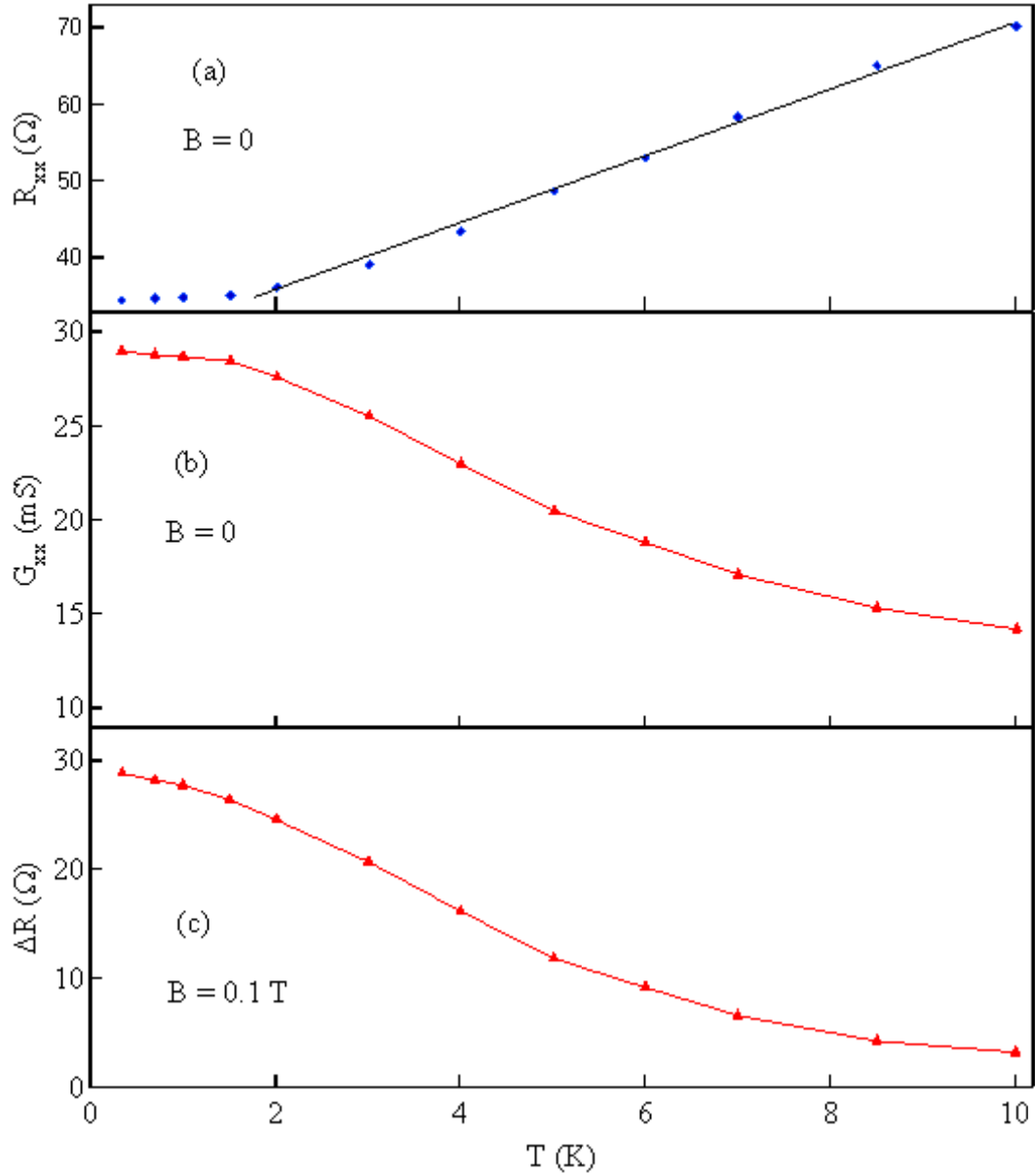
Fig. 0.5 (a) and (b) are the resistance R_{xx} and conductance G_{xx} vs T, respectively, at B=0; (c) is the temperature dependence of the amplitude of GR peak 2 in Fig. 3.3.

condition $k_B T \leq \hbar\omega_c k_F a/2$, where $k_F = \sqrt{2\pi n_e}$ is the Fermi wavevector of the 2DES

and a is period of the lattice. Interestingly, this behavior is similar to the temperature

dependence of the $B = 0$ conductance, shown in inset (b), which is characteristic for the thermally excited phonon-scattering model [112]. From insets (a), (b), and (c) of Fig. 3.5, we can see that this regime transition happens at about $T = 1.5 - 2$ K.
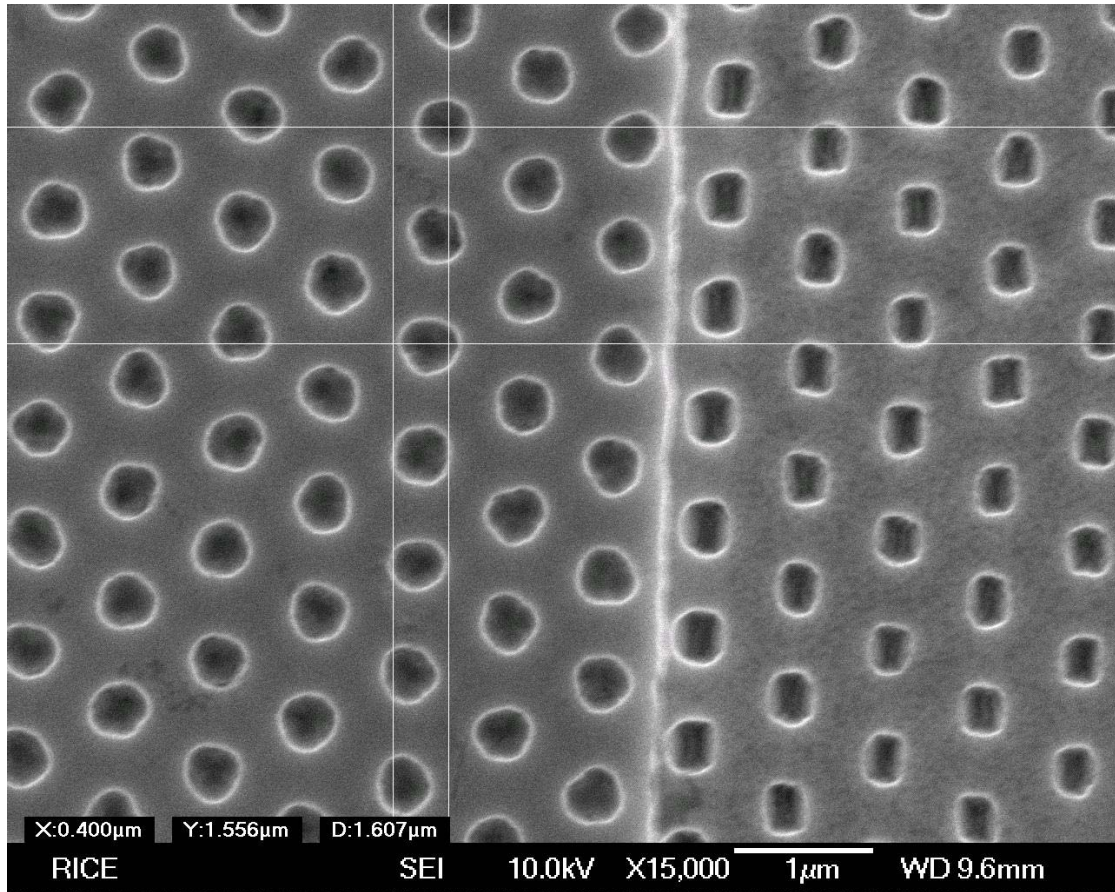
Fig. 0.6 SEM image of antidot lattice with period $a = 800$ nm and diameter $d = 400$ nm which is larger than the designed value $d = 300$ nm.

For comparison, another sample was cleaved from the same sample wafer and patterned a triangular lattice with period $a = 800$ nm. The antidot lattice was introduced by e-lithography and wet etching and its SEM image is shown in Fig. 3.6. The image clearly shows that the diameter of each antidot is around 400 nm which is larger than the

designed value, d = 300 nm. This enlargement of antidots results from wet etching process. Magnetoresistance trace, shown in Fig. 3.7, shows very strong GR whose amplitude is about three orders larger than that of GR in Fig. 3.3. And after introduction of antidot, mobility of 2DEG is more two orders smaller than its original value.

Magnetoresistance measurements on 2DEG with antidot lattice indicate that our first
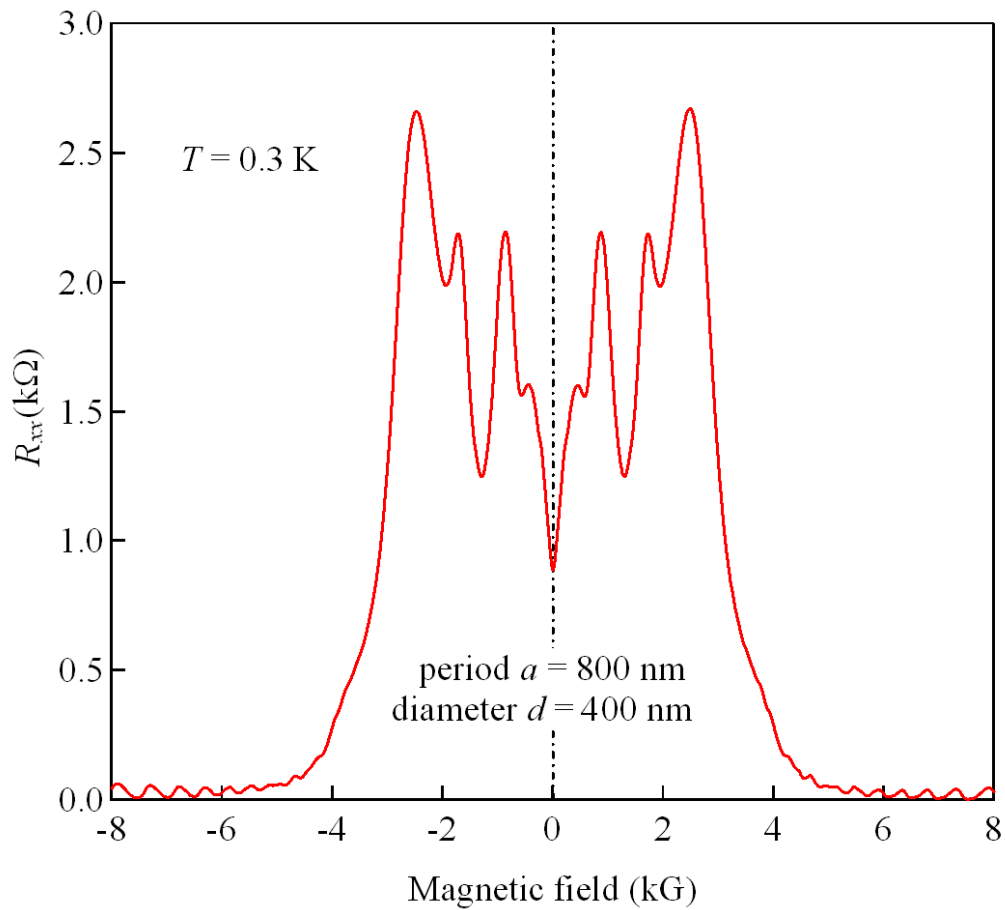
Fig. 0.7 Geometric resistance peaks in a low field of resistance R_{xx} on 2DEG with triangular antidot lattice (a = 800 nm, d = 400 nm) at T = 0.3 K. The amplitudes of GR are around three orders larger than those in Fig.3.3.

sample still has extraordinary quality after introduction of triangular lattice, which make it an appropriate system to explore influence of 2D modulation on microwave induced resistance oscillations.

3.2. MIRO on 2DEG with triangular antidot lattice

The MIRO and ZRS in a modulated 2DEG have been studied in recent theoretical works [94, 95, 97]. In particular, for 1D modulation [94, 95], the displacement model and the distribution function model are found to contribute to MIRO in an anisotropic In principle, experiments in such a system can help to distinguish the relative contributions from each mechanism. For 2D modulation [97], different features can be expected on an ultraclean 2DEG. Moreover, a periodical modulation with period a breaks translational symmetry of the 2DEG allowing studies of photoresistance with a finite momentum transfer $\Delta q = 2\pi/a$ in this system.

Our previous magnetoresistance measurement proved a high quality 2DEG after patterned triangular antidot lattice. This provides us an appropriate system for experimental study of MW photoresistance in a 2D periodically modulated 2DEG. MIRO are observed in the 2DEG and retain a $1/B$ periodicity as in unmodulated 2DEG, but their amplitude is strongly damped. We also found the photoresistance peaks corresponding to long-wavelength magnetoplasmon (MP) resonance; the dispersion of MP is controlled by the width of the Hall bar rather than the period of potential modulation. We conclude that the MIRO, MP, and DC geometric resonance (GR) are decoupled from each other in our experiments. While MW photoconductivity has been reported for antidot arrays in a modest-mobility 2DEG [30], our work on a high-mobility system reveals different

features, including MIRO, and opens a window for studies of nonequilibrium quantum transport.

The sample used for photoresistance measurement is the same one used in the GR measurement. It is an 80 μm × 320 μm Hall bar with a 2DEG having an electron density $n = 2.83 \times 10^{11} \text{cm}^{-2}$ and a zero field mobility $\mu = 2.5 \times 10^{6} \text{cm}^{2}/\text{Vs}$ after patterned a triangular antidot lattice, with period of $a = 1500$ nm and dot diameter of $d = 300$ nm. Our measurement was performed in He^3 refrigerator equipped with an 11-T superconducting magnet. The magnetoresistance R_{xx} is measured with standard low frequency lock-in technique (frequency 23 Hz and excitation current 1 μA). For the photoconductivity measurement, the mutual orientation of the waveguide, sample, and the magnetic field corresponds to Faraday configuration in which the excitation current flows perpendicularly to the microwave polarization.

We measured the MW photoresistance on a 2DEG with antidot lattice. Here the MW photoresistance is defined as the change of resistance due to MW irradiation, *i.e.* $\Delta R_{xx}^{\omega}(B) = R_{xx}^{\omega}(B) - R_{xx}^{0}(B)$, with $R_{xx}^{\omega}(B)$ and $R_{xx}^{0}(B)$ being the magnetoresistance with or without MW irradiation, respectively. As an example, Fig. 3.8 shows traces with and without continuous MW irradiation at $f = 55.8$ GHz. In this measurement, the environment temperature was kept at $T \sim 1$ K.

The R_{xx} trace with MW irradiation looks quite complicated because GR and MIRO overlap in this low magnetic field regime. And as can be seen in Fig.3.8, the GR dominate this regime and make the MIRO difficult to resolve. Our analysis shows that under MW irradiation, both the electron-heating effect and MIRO contribute to the ΔR_{xx} of the patterned 2DEG. The heating effect originates from the strong T dependence of GR

37
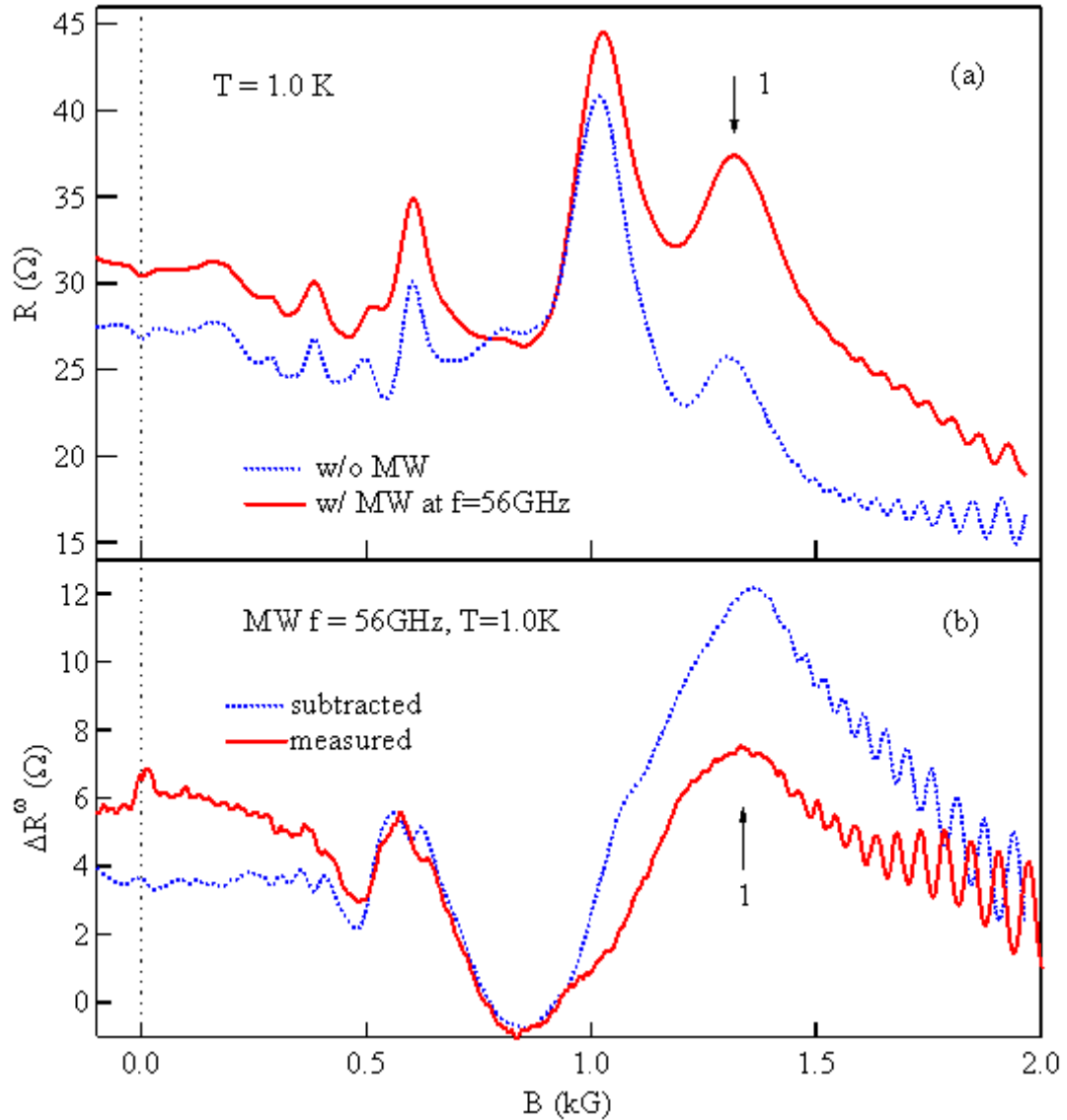
Fig. 0.8 (a) Magnetoresistance traces with and without continuous MW irradiation. (b) The difference (dotted line) between the two traces shown in (a), and the MW-induced signal (solid line) measured with the double-modulation technique. The arrows indicate the first peak of MW-induced oscillation.

peaks in the temperature range $T > 1.5$ K, as shown in Fig. 3.4 in section 3.1. Since GR peaks exhibit a negative temperature coefficient, $dR_{xx}/dT < 0$, electron heating results

in a reduction of R_{xx} in the sample. Our main purpose in this experiment is to recover the photoresistance ΔR_{xx}^{ω} from the background of the electron-heating signal.

It is possible to deduce the ΔR_{xx}^{ω} by numerically substracting R_{xx}^0 from R_{xx}^{ω}, as shown by the dotted line in Fig. 3.8 (b). The ΔR_{xx}^{ω} obtained in this way shows an oscillatory structure roughly periodical in 1/B, similar to the MIRO observed in unpatterned 2DEG. On the other hand, significant distortion of the R_{xx}^{ω} can be anticipated owing to the contribution from the electron heating effect. While both the R_{xx}^0 and R_{xx}^{ω} data were taken at approximately the same environment temperature $T \sim 1.0$ K, the electron temperature is expected to be considerably higher in R_{xx}^{ω}, leading to a large heating component.

The ΔR_{xx}^{ω} can also be measured directly by a double modulation technique [114] in the following fashion. The MW was chopped at a frequency $f = 11.5$ Hz, and the sample excitation current is synchronized at the double frequency $2f = 23$ Hz. Using the frequency f as a lock-in reference, it can be shown that the ΔR_{xx}^{ω} can be attained from the 90° lock-in signal [114]. The ΔR_{xx}^{ω} at the same MW frequency $f = 56$ GHz, measured with a double-modulation method, is shown in Fig. 3.8 (b). We note that the ΔR_{xx}^{ω} obtained by both methods coincide reasonably well in their oscillatory structure in B, indicating the equivalence of these two methods in obtaining the ΔR_{xx}^{ω}.

The following observations can be made for the MIRO in a modulated 2DEG, as measured here, in comparison to the MIRO in an unpatterned 2DEG (8). First, the MIRO in modulated 2DEG retain the characteristic period in 1/B determined by $\epsilon = \omega_{MW}/\omega_c$. Second, the damping of MIRO is much steeper in the modulated sample even though the mobility is comparable. The mobility of the unpatterned sample in Ref. 8 is about

$3 \times 10^6 \text{cm}^2/\text{Vs}$, where up to ten MIRO peaks can be observed, whereas in the present

sample of a mobility $2.5 \times 10^6 \text{cm}^2/\text{Vs}$, only two peaks are clearly resolved. Of course,

mobility is directly proportional to the transport lifetime τ_{tr}, which is only relevant at $B =$

0. In a small magnetic field, the electron orbital dynamics are strongly influenced by the

modulation. The above observations may point to an interesting theoretical question as to

how such a modulation will affect the electrical current distribution in the MIRO regime.

On a side note, our results could also support the notion that MIRO is a bulk, rather than

an edge, effect.

Using the double-modulation method, we have measured the MIRO in a wide range

of frequencies between 32 and 130 GHz, and qualitatively the same conclusion can be

drawn throughout this range: MIRO can be clearly observed in a 2DEG with a shallow

triangular antidots modulation, but with strongly damped amplitude.

We observed an additional single-resistance peak in the high-frequency regime $f > 85$

GHz, and identified it as the signal of magnetoplasmon resonance [8, 50]. Since the

MIRO and MP resistances are superposed, we rely on the following empirical procedure

to extract the MP signal.

It is shown empirically in Ref. 48 that the periodicity and the shape of ΔR_{xx}^{ω} in the

MIRO can be reasonably fitted by a model based on the oscillatory electron-distribution

function at a given temperature T, Eq. (2.25), with the Landau level width Γ being a

fitting parameter. In Fig. 3.9, we fit the 120 GHz experimental ΔR_{xx}^{ω} (solid line) with a

calculated curve (dotted line). Both the zero line and the amplitude of the curve were

adjusted such that the envelops of both coincide. From the fit, we obtain a LL width of ~
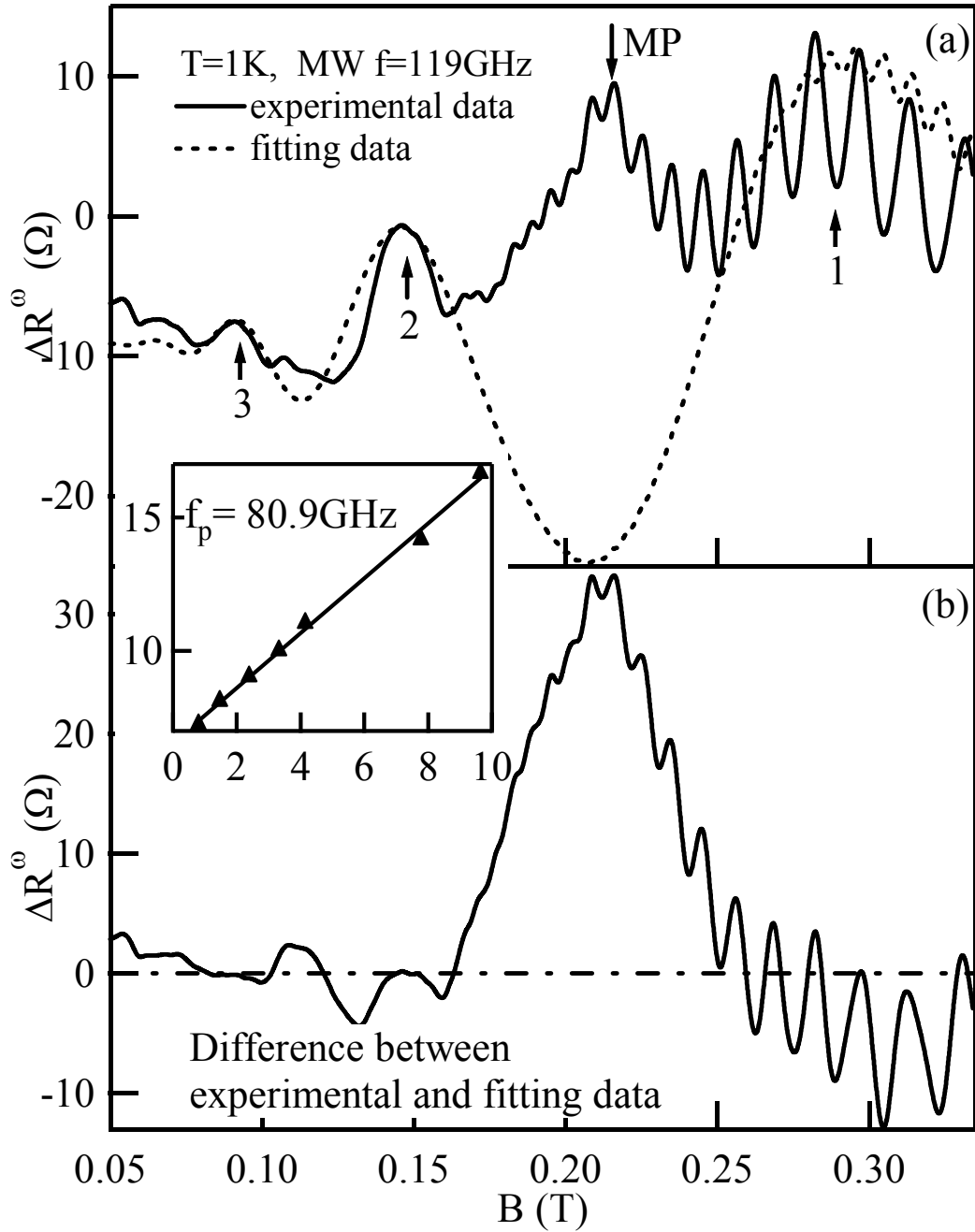
Fig. 0.9 A selected photoresistance trace at MW frequency f =120 GHz and the numerical fitting for MW-induced oscillations. The little upwards arrows indicate peaks of microwave induced resistance oscillations and the downwards arrow indicates the magnetoplasmon peak. The difference between these two traces gives the clear magnetoplasmon signal [see (b)]. The inset shows the typical relation between the microwave frequency and magnetoplasmon peak position with the fitting curve based on Eq. (2.27). The unit of axes in inset is $(100 \text{ GHz})^2$.

56 μeV ~ 0.65 K corresponding to a quantum scattering time of $\hbar/\Gamma$ ~ 12 ps. It is interesting to compare the fitted LL width Γ in the MIRO of unpatterned 2DEG from the same wafer, which is 41 μeV (16 ps).

Subtracting the fitting curve from the experimental trace, we arrive at a trace which is dominated by a strong MP peak taking place at magnetic field given by Eq. 2.27: $\omega_{MW}^2 = \omega_p^2 + \omega_c^2$. This relation of Eq. 2.27 is well revealed in the inset of Fig. 3.9, and a slope of linear fitting gives a 2D plasmon frequency of 80.9 GHz. For our GaAs sample, taking into account the fact that the 2DEG is very close to the surface, the effective dielectric constant is 6.9 [50]. Using $m^* = 0.068\ m_e$ and the width of Hall bar, 80 μm, with formula (2.28): $\omega_p^2 = n_e e^2 k / 2\epsilon\epsilon_0 m^*$, we arrive at a 2D plasmon frequency 98 which is about 20% larger than the measured one. This result is consistent with that in Ref. 50, in which the measured 2D plasmon frequency is smaller than the calculated one. The main reason for this discrepancy should come from the fact that formula (2.28) is derived for infinite 2D Plasmon. On a Hall bar sample, the electromagnetic field in the finite region surrounding the bar shall be quite different from the one in infinite plane [50], *i.e.* formula (2.28) is not accurate for Hall bar geometry.

Chapter Four Quantum Transport in 2D Hole Gas (2DHG)

Two-dimensional hole gas (2DHG) in modulation doped GaAs/AlGaAs has attracted much attention for recent years because of its unique charge and spin properties derived from valence band structure. Typical band structure of bulk GaAs is shown in Fig. 4.1(a), in which the hole band has four fold degeneracy at $k = 0$ (light and heavy holes, spin up and down). Under confinement of quantum well, due to difference in effective masses of heavy and light holes ($m_H^* = 0.5\ m_e$, $m_L^* = 0.08\ m_e$ are effective masses of heavy and light holes in bulk GaAs, respectively, with m_e the bare electron mass), heavy and light holes have different ground state energies so that their bands are separated, as shown in Fig. 4.1(b). Mainly because of inversion asymmetry of quantum well (Rashba effect) [115], the heavy band has further splitting at non-zero k even at zero magnetic field, named as zero field spin splitting, as shown in Fig. 4.1(b).
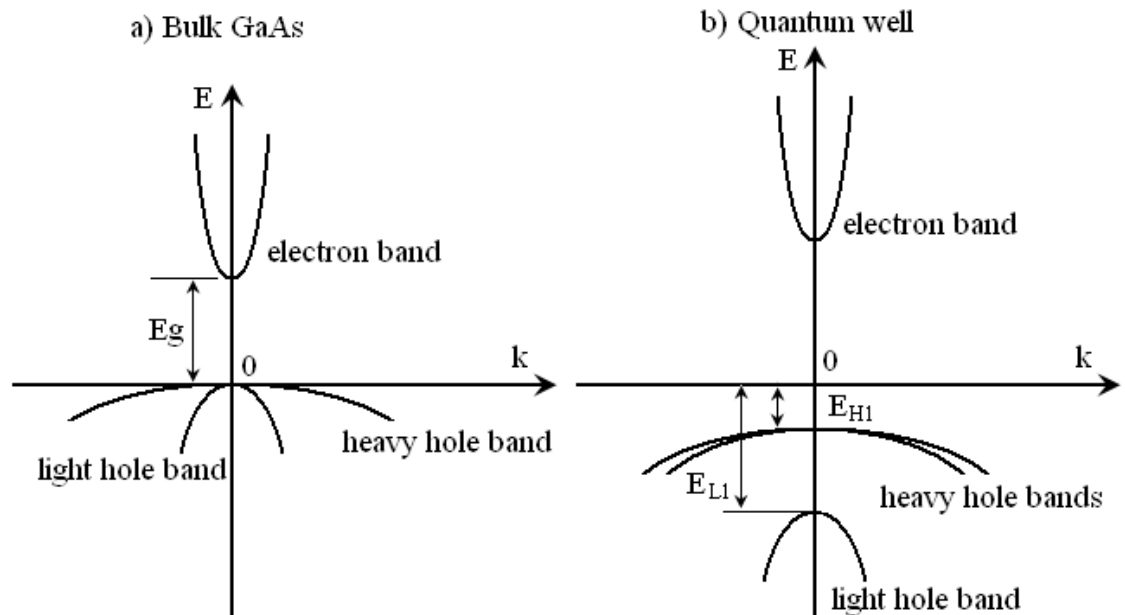
Fig. 0.1 Band structure diagrams of (a) bulk GaAs and (b) GaAs in quantum well. E_{HI} and E_{LI} are ground state energies of heavy and light hole in the quantum well.

Many theoretical works have been done on calculating subbands structure and effective mass of 2DHG [116-122]. Extensive experimental research also has been reported on exploring properties of 2DHG formed in different structures [15, 123-139]. Until recently, the 2DHG materials have been provided by Be or Cr-doped (100), or Si-doped (311)A GaAs structures. 2DHG in (100) GaAs is simpler than that in (311)A GaAs because of higher symmetry of the material. However, diffusion of Be dopants during the molecular beam epitaxial (MBE) procedure greatly limits mobility of 2DHG in Be-doped (100) GaAs. Wieck and Reuter [135], Manfra *et al* [136], and Gerl *et al* [137] reported a carbon (C)-doped (100) GaAs/AlGaAs MBE technique, which has led to a steady improvement in low temperature carrier mobility. Due to its unprecedented cleanliness, the C-doped GaAs/AlGaAs quantum structures become an increasingly important system for studies of strongly correlated carriers in which Coulomb interaction, disorder, and spin-orbital coupling parameters can be controlled. In the following sections, results of magnetotransport measurement conducted on 2DHG in C-doped (100) GaAs/Al$_x$Ga$_{1-x}$As square quantum well will be reported, which will include effective mass measurement with microwave (MW) cyclotron resonance (CR), gate characterization, zero field spin splitting and effective *g*-factor investigation with tilted magnetic field, geometric resonance (GR) on 2DHG with triangular antidot lattice, and microwave induced resistance oscillations on 2DHG.

4.1. Effective mass of 2DHG

Effective mass of 2DHG was measured by detecting microwave (MW) cyclotron resonance (CR). When MW cyclotron resonance happens, MW frequency ω_{MW} shall be equal to cyclotron frequency ω_c, *i.e.*

$$\omega_{MW} = \omega_c = \frac{eB}{m_e m^*} \tag{4.1}$$

where m_e, m^* are bare electron mass and effective mass of hole, respectively. Thereby once MW frequency and magnetic field position of CR are known, the effective mass can be calculated.

In MW CR, the sample will absorb microwave irradiation energy so that its temperature rises. So cyclotron resonance can be located by monitoring the change of sample temperature, the CR signal [133]. Moreover, in the linear response regime, where measurement was performed, CR signal is proportional to absorbed MW power which is determined by the real part of photoconductivity of 2DEG. Therefore, the line shape of CR signal can be described by Drude model:

$$\frac{Re\{\sigma_{xx}\}}{\sigma_0} = \frac{1 + (\omega_c \tau_{CR})^2 + (\omega_{MW} \tau_{CR})^2}{[1 + (\omega_c \tau_{CR})^2 - (\omega_{MW} \tau_{CR})^2]^2 + 4(\omega_{MW} \tau_{CR})^2} \tag{4.2}$$

where σ_o is conductivity at zero field, τ_{CR} is the CR relaxation time which describes the effect of collisions of holes with scattering centers presented in 2DHG [140].

4.1.1. Experiment setup

The sample for MW CR measurement is 1 mm × 1 mm square without any contacts. It was cleaved from a sample wafer (wafer 10-21-03.1) which consists of 15 nm wide GaAs/Al$_{0.4}$Ga$_{0.6}$As quantum well grown by MBE on direction (001) and has Carbon δ-doping layer situated 50 nm above from the well. It has a hole density of $p \approx 2.2 \times 10^{11}$ cm^{-2} and a mobility of $\mu \approx 0.7 \times 10^6$ cm^2/Vs at 300 mK. The experiment was performed at 4.2 K in a liquid helium dewar equipped with 9-T superconducting magnet. Measurement setup is shown on Fig.4.2. A long sapphire bar, about 1 mm wide and 0.5 mm thick, goes through a hole on one wall of a brass cavity. Then the hole is filled
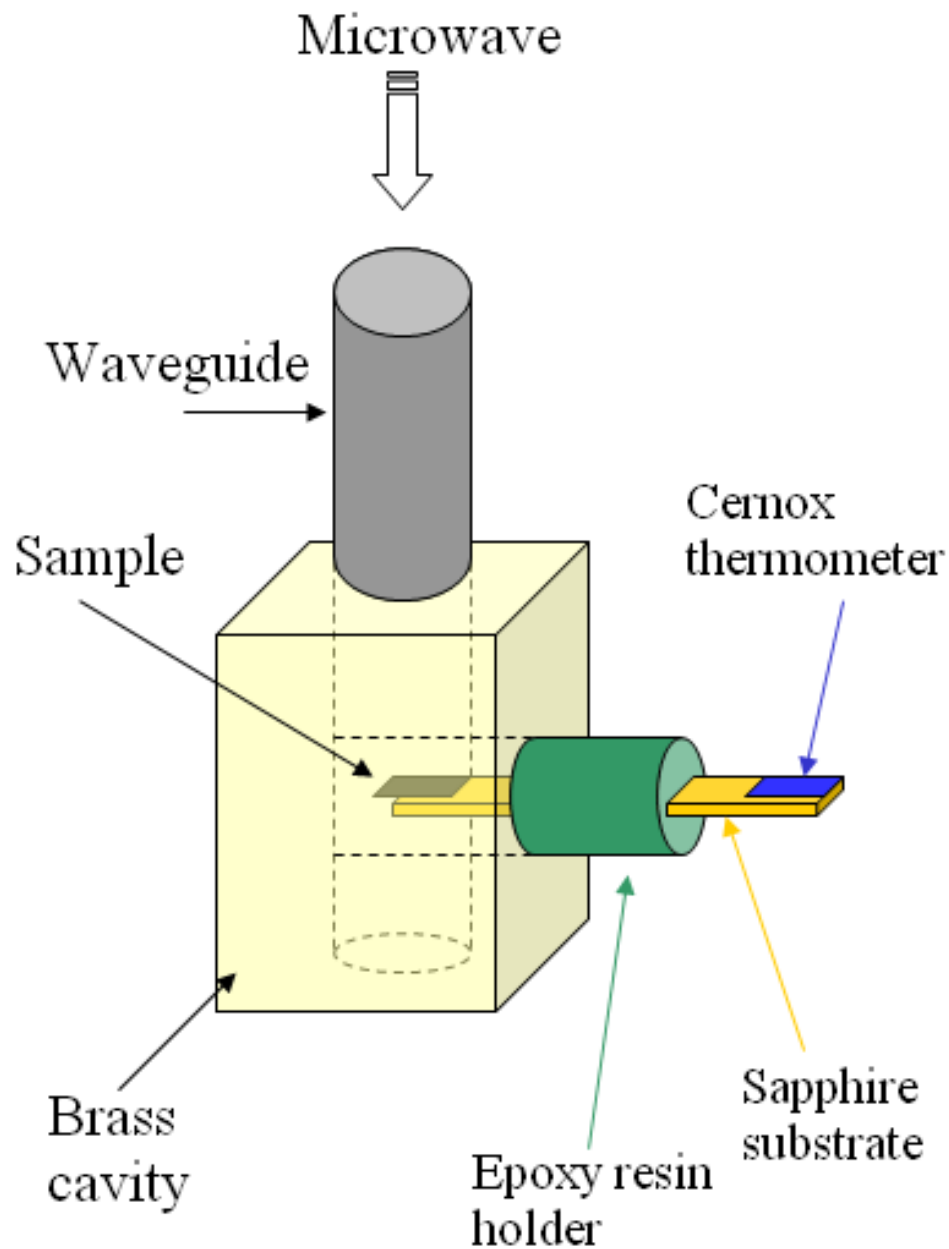
Fig. 0.2 Experimental setup for measuring effective mass of 2DHG by detecting microwave cyclotron resonance.

with Stycast 1266 Epoxy so that the sapphire bar can be held by the cavity but remains thermally isolated within the cavity. A Cernox thermometer (Lakeshore CX-1070-BG) is

glued on the sapphire bar outside the cavity by G-vanish and sample is attached on the inside part of the sapphire bar by low temperature grease so that the sensor can sensitively detect the temperature change of the sample. Then the brass cavity is vacuum sealed and filled with small amount of He^4 gas as exchange gas so that we can keep the temperature inside cavity as the same as the environment, 4.2 K. On the top of cavity, there is a window connected with MW waveguide. In the measurement, MW irradiation with fixed frequency goes down through waveguide and hits the sample, while the magnetic field is swept to get CR, which is then detected by the Cernox thermal sensor. In this setup, as the Cernox thermal sensor just needs to detect the change of temperature of sample, no calibration for Cernox sensor is needed.

4.1.2. Experiment results

In our measurements, CR in range between MW frequency, f = 25 and 55 GHz was detected. Five selected CR signals of f = 25.5, 31.6, 39.2, 44.7 and 50.1 GHz are shown in Fig. 4.3. A simple fitting with equation $\omega_c = eB/m^*m_e$ gives $m^* \cong 0.42$, shown in inset of Fig. 4.3. The result that only one effective mass was detected implies that, roughly speaking, spin splitting in this structure is smaller than the Landau level broadening of Landau levels in this quantum well.

We fitted the CR signal of f = 39.2 GHz with the Drude formula (4.2) by using σ_0, τ_{CR} and m^* as fitting parameters, shown in Fig. 4.4. We determine simultaneously the m^* $\cong 0.42$ and $\tau_{CR} \cong 14\ ps$. On the other hand, from $\mu = e\tau_{tr}/m_e m^*$, and with $m^* \cong 0.4$, we arrive at a transport scattering time, $\tau_{tr} \approx 160\ ps$. The ratio $\tau_{tr}/\tau_{CR} > 10$ indicates that in our modulation C-doped (100) GaAs/AlGaAs quantum well, long range scattering
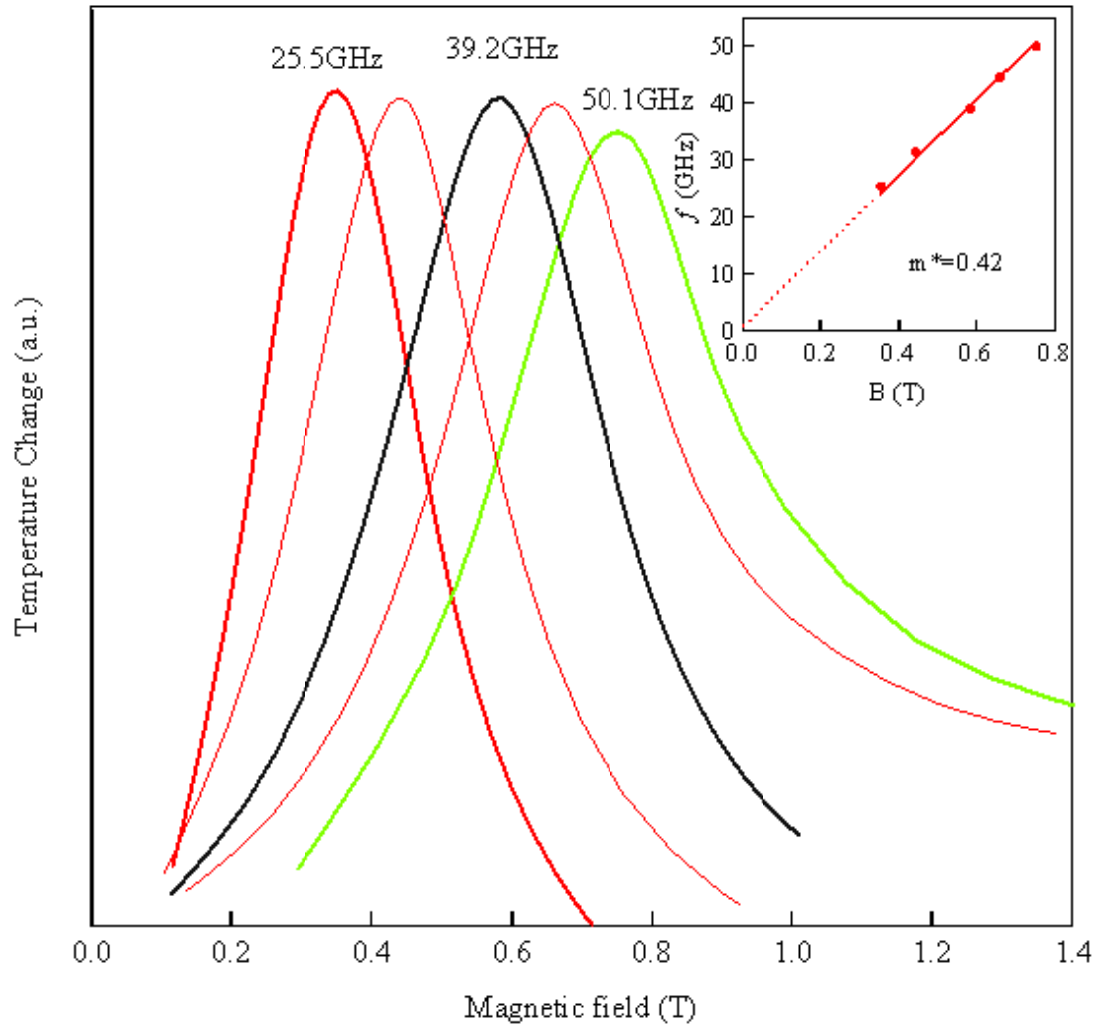
Fig. 0.3 Cyclotron resonance signals of microwave frequencies f = 25.5, 31.6, 39.2, 44.7 and 50.1 GHz are shown. Linear fitting in inset gives $m* \approx 0.4$.

from ionized impurities in C-doping layer is dominant [18]. It is interesting to note that the value $\tau_{tr} \approx 160\,ps$ is corresponding to a mobility of 4 x 10^6 cm^2/Vs in a GaAs 2D electron gas (2DEG), taking into account the electron effective mass 0.067. We therefore conclude that the 2DHG measured here exhibits high quality compatible with high-mobility 2DEG.
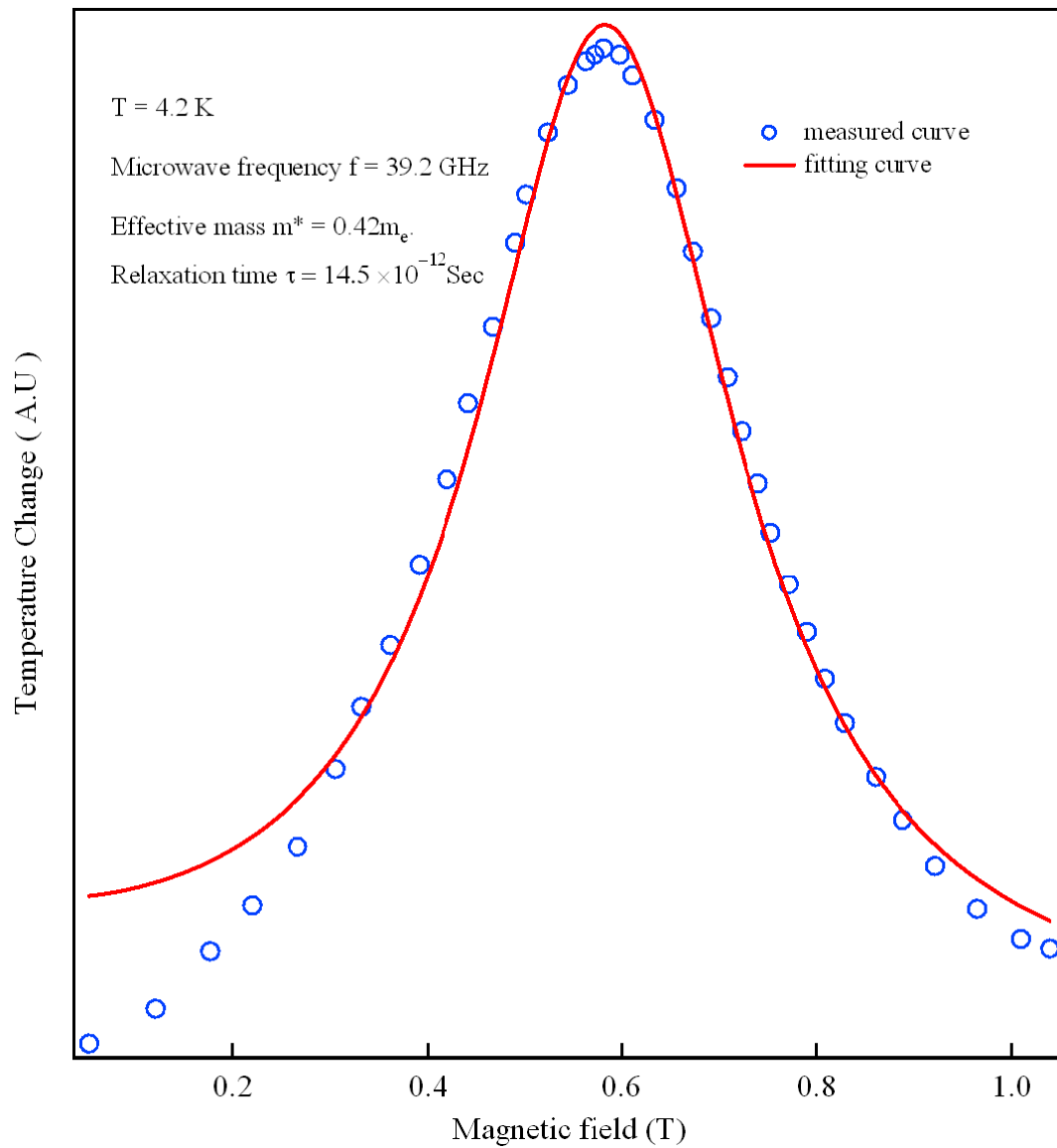
Fig. 0.4 Fitting to Drude formula for f = 39.2 GHz cyclotron resonance signal gave m^* = 0.42 and CR relaxation time τ_{CR} = 14.2 ps.

The figure contains the following annotations:

T = 4.2 K

Microwave frequency f = 39.2 GHz

Effective mass m* = 0.42m$_e$.

Relaxation time τ = 14.5 $\times 10^{-12}$ Sec

○ measured curve
— fitting curve

Axis labels: Temperature Change (A.U), Magnetic field (T)

4.2. Magnetoresistance measurement in 2DHG

4.2.1. 2DHG with Gate

The sample for magnetotransport measurement was cleaved from the same 2DHG wafer (10-21-03.1) as the one for effective mass measurement. The sample piece has size of 3 mm × 5 mm, on which a 20 squares 100 μm Hall bar was defined by photolithography. And a 100-nm-thick NiCr gate was patterned to cover the Hall bar by using thermal evaporation. After fabrication, the 2DHG still has a hole density of $p \approx 2.2 \times 10^{11}$ cm^{-2} and a mobility of $\mu \approx 0.7 \times 10^6$ cm^2/Vs at 300 mK. The magnetoresistance measurements were performed in Oxford He^3 refrigerator, equipped with a 12 T superconducting magnet, with base temperature of 300 mK. DC gate voltage ranging from 5 to -1.2V was applied to the gate to change density of 2DHG. Three SdH traces of different gate voltages are shown in Fig. 4.5.

Main features of the gate are following:

1). The gate doesn't work at gate voltage with range from 5 to -1V. At the moment of applying gate voltage, the density of 2DHG does change, however, this change can't be held and the density drifts back.

2). When gate voltage is larger than 5V, the 2DHG totally dies out and has to be warmed up to recover.

3). Once the gate voltage goes beyond -1V, the density of 2DHG can be changed from 2.1 to 3.6×10^{11}cm^{-2} and held, as shown in Fig. 4.5. At gate voltage -1.2V, density increases by more than twice to 4.5×10^{11}cm^{-2}. The inset shows relation of density vs gate voltage. The nonlinearity of curve is obvious.

50
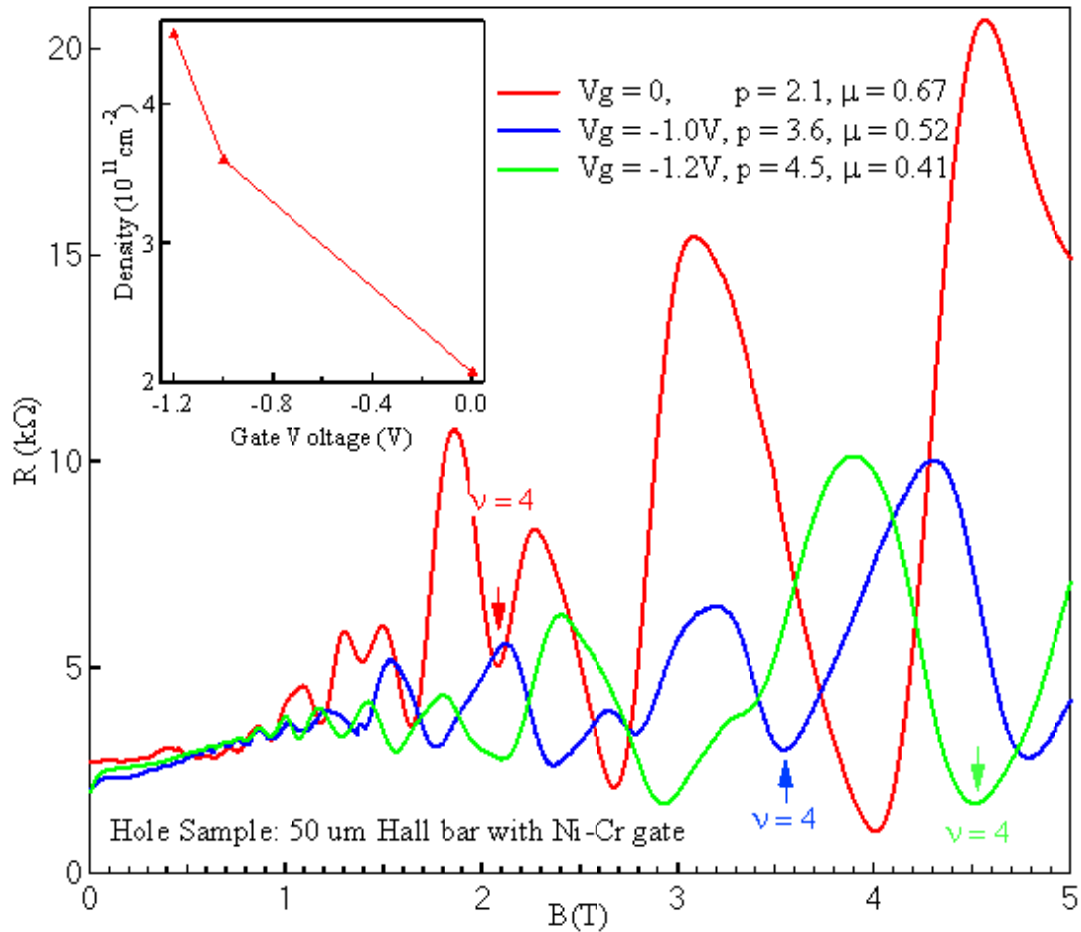
Fig. 0.5 SdH traces of 2DHG under different gate voltages, V_g. Density can be changed just after V_g < -1 V. Density vs V_g indicates that density doesn't change linearly with gate voltage.

4). When gate voltage goes beyond -1.2V, leakage current, about 10 nA, can be detected.

Hence overall, the gate on this 2DHG sample is not working reliably. Based on the behaviors of the gate, it looks that there is a threshold gate voltage, about -1V with electric field about 4×10^6 V/m, above which the density can be changed and held. This implies that it is the structure of material, rather than the fabrication procedure,

preventing the gate from working well. In this GaAs/AlGaAs quantum well structure, there is a front C δ-doping layer situated 50 nm away from the well. This doping layer has a few carriers but has a very low mobility. When we do transport measurements, we only see the 2DHG in the quantum well because of its much higher mobility so much lower resistance. However, when we apply a gate voltage, the doping layer would screen the 2DHG layer. Therefore, all the density change is happening in the doping layer. When we see a change in density which slowly drifts back, it means that the doping layer has a so high resistance that it takes time to charge up and fully screen the gate.

4.2.2. Zero field spin splitting and g-factor of 2DHG

The sample for magnetoresistance measurement is a 100 μm Hall bar with 20 squares lithographically defined on a 3 mm × 5 mm piece which was cleaved from a same wafer as the sample for effective mass measurement. The measurement was performed in a top-loading dilution refrigerator equipped with an *in situ* rotator placed inside an 18-T superconductive magnet. With the rotator, the magnetic field could make a titled angle, θ, ranging from 0 to $90°$ with respect to the normal to the 2DHG plane. The magnetoresistance, R_{xx}, and Hall resistance, R_{xy}, are recorded by using standard low frequency, 17 Hz, lock-in technique with a 50 nA excitation current.

Magnetoresistance of 2DHG was measured in the Hall bar sample. A typical Shubnikov de Haas (SdH) trace is shown in Fig.4.6, in which two main features should be emphasized. First, in low field regime, $B_\perp \leq 1T$, clear beating pattern indicates existence of two SdH periods in 1/B. Spectrum of Fourier Transform (FT) of R_{xx} vs 1/B in range of 0.2 ~ 3 T, shown in Fig.4.7, indicates three frequencies f_-, f_+ and f_T
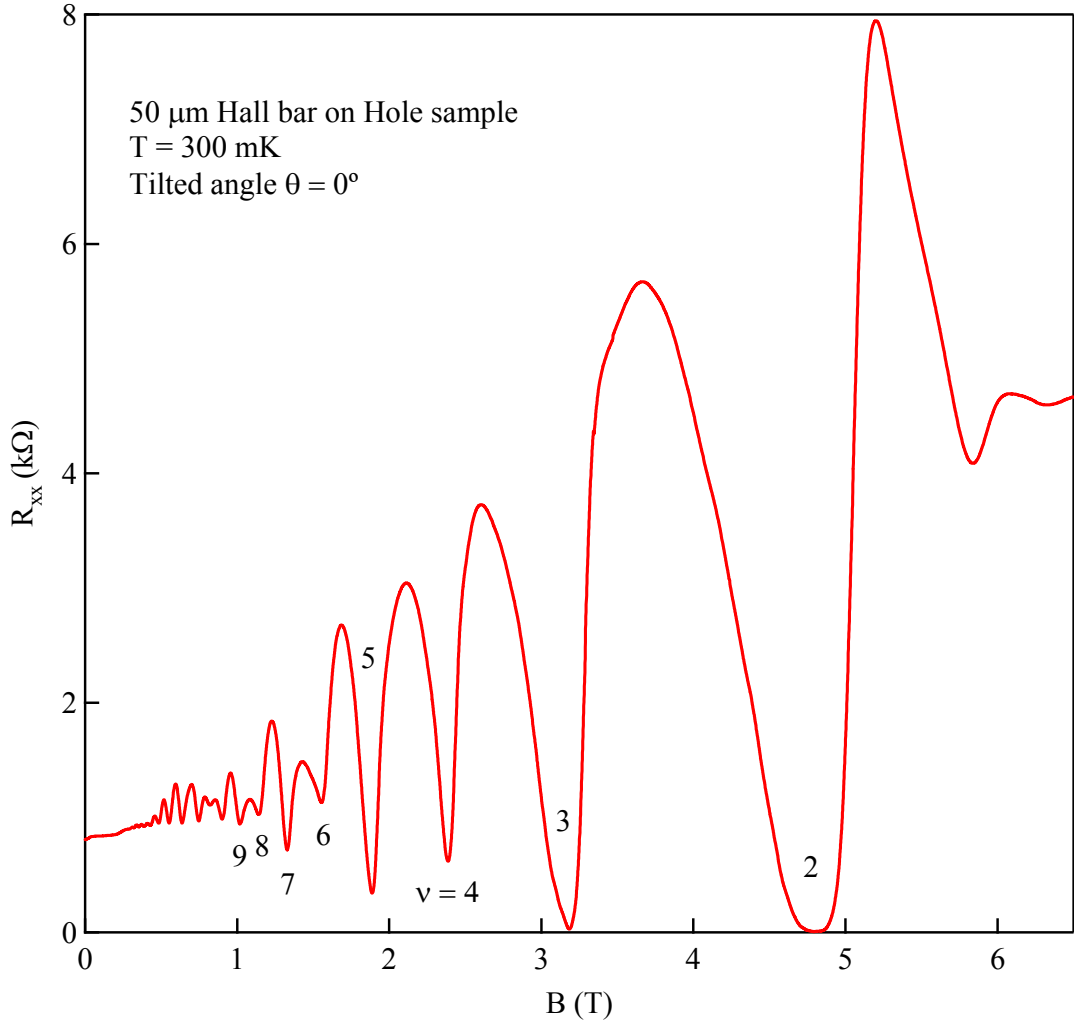
Fig. 0.6. Magnetoresistance of 2DHG in C-doped GaAs/AlGaAs quantum well. Clear even-odd reversal of minima of $v = 3, 4, 5, 6, 7$ is shown.

with $f_T \cong f_- + f_+$ corresponding to total hole density. As in previous work reported for (001) GaAs/AlGaAs square quantum well, we can rely on the relation $p_\pm = (e/h)f_\pm$ to estimate hole populations [141], with $p_{-(+)}$ the density of lower (higher) populated subband: $p_- \cong 0.94 \times 10^{11} \text{cm}^{-2}$ and $p_+ \cong 1.09 \times 10^{11} \text{cm}^{-2}$. A population difference $\Delta p = 2(p_+ - p_-)/(p_+ + p_-) \sim 15\%$ indicates existence of a finite zero field spin splitting due to spin-orbital interaction in the 2DHG. Such value is considerably smaller
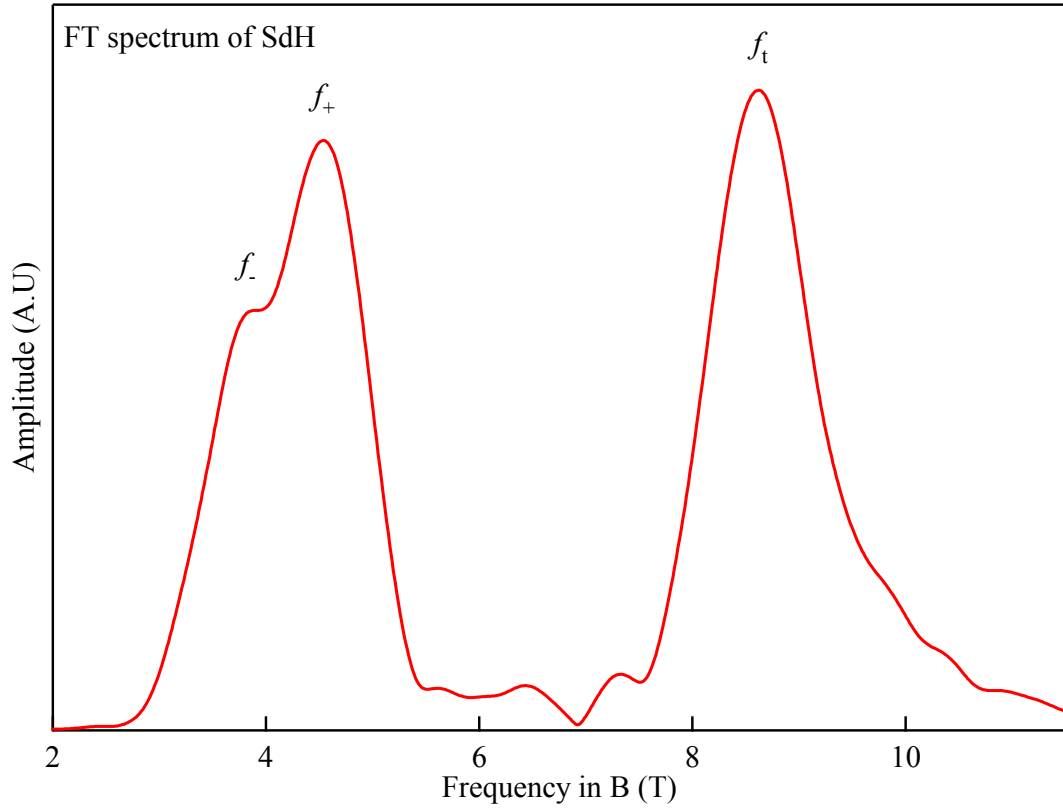
Fig. 0.7. Fourier Transform spectrum of SdH oscillations in magnetic field range of 0.3 to 3 T, in which three peaks were shown.

than that being reported for 2DHG in (100) single-interface heterostructure [134], where $\Delta p \sim 67\%$ presumably due to strong Rashba effect in triangular potential quantum confinement.

Second, in high field regime, $B_\perp > 1T$, SdH oscillations show clear reversion of even-odd minima pattern from filling factors $\nu = 3$ to 9. In contrast to standard transport in GaAs/AlGaAs 2DEG, here odd minima are deeper than their adjacent even ones. A simple model based on spin-splitting Landau level diagram would suggest that the
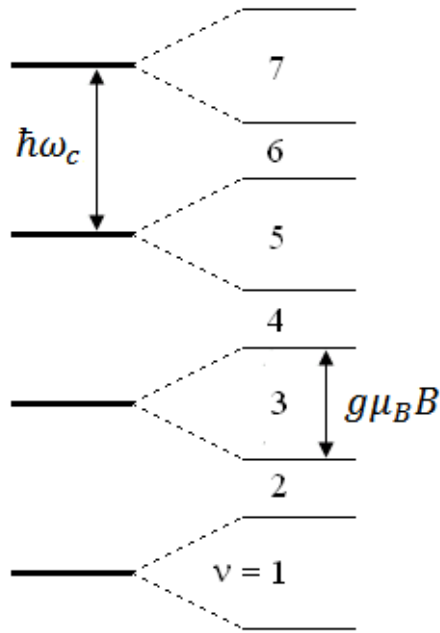
(a) without level crossing   (b) with level crossing
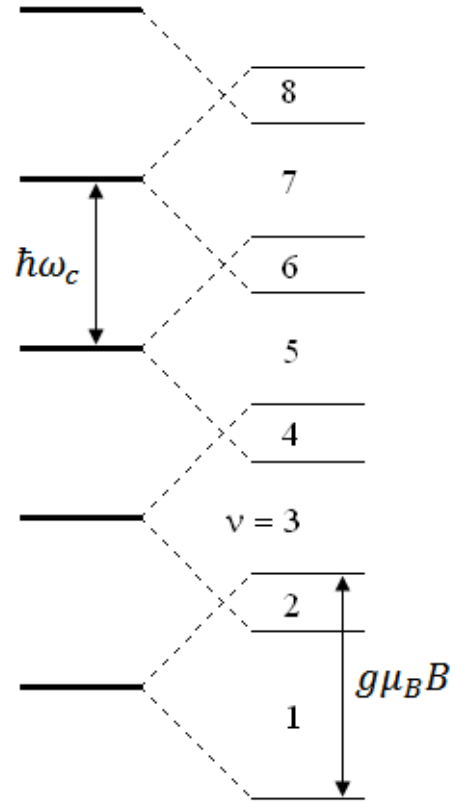
Fig. 0.8. Diagrams of possible Landau level configurations causing reversion of even-odd minima in SdH trace.

Zeeman energy is comparable to cyclotron energy, as depicted in either (a) or (b) in Fig. 4.8 with or without level crossing. To understand this reversion phenomenon, we measured the magnetoresistance under titled magnetic field with θ ranging from 0 to 86°. SdH traces of selected tilted angles and the evolutions of minima of $v = 4, 5, 6,$ and 7 with tilted angle are shown in Fig. 4.9 (a) and (b), respectively. From Fig.4.9 (b), we observe that for $\theta > 80°$, the even minima of $v = 4, 6$ become, respectively, deeper than the minima of $v = 5, 7$. In particular, from Fig. 4.9 (a), the minimum of $v = 9$ disappears

at $\theta = 85°$, indicating a coincidence of levels. The fact that such coincidence pattern occurs at $v = 9$ requires, for $B_\perp \sim 1T$, a level diagram as the one shown in Fig. 4.8 (b) in which the Zeeman splitting is large enough to cause Landau level crossing even at zero tilt. This Landau level crossing requires $\frac{3}{2}\hbar\omega_c > g\mu_B B > \hbar\omega_c$, where $\mu_B = e\hbar/2m_e$ is Bohr magneton. Simple calculation gives $3 > gm^* > 2$. With $m^* \cong 0.4$, we constrain $7.2 > g > 5$, which is close to g-factor of bulk hole ($g = 7.2$) [142], while is much bigger than previous results [142, 143], in which $g \sim 2$ for 15nm quantum well.

It is known that the Landau level of 2DHG is hightly nonlinear with $B_\perp$ mainly due to the magnetic field dependence of the effective mass of 2DHG [144]. Moreover under tilted magnetic field, the presence of in-plane magnetic field $B_\parallel$ is likely to increase the effective mass [145-147]. Despite these complications in 2DHG, for specific magnetic field at which coincidence occurs at $v = 9$, we still have coincident conditions: $2\hbar\omega_c = g\mu_B B$ according to Landau level diagram Fig. 4.8 (b). It was reported that g-factor of 2DHG in GaAs/AlGaAs structure is strongly anisotropic [130, 131], and its in-plane component is close to zero [131], i.e., $g = g_\perp$ so that in-plane magnetic field $B_\parallel$ has no contribution to Zeeman splitting. Therefore the coincident condition become $2\hbar\omega_c = g\mu_B B_\perp$. Simple calculations give $gm^* = 4$ which is larger than the initial value without in-plane magnetic field $B_\parallel$. Previous measurements [142, 143] showed that $g_\perp$ is nearly independent on magnetic field. Assuming a constant $g_\perp$ in this QW, we can get the range of m^* under high tilted magnetic field, $0.53 < m^* < 0.8$, which is larger than its initial value, $m^* \cong 0.4$. This increase in m^* verifies the enhancement effect of in-plane magnetic field on the effective mass of 2DHG.
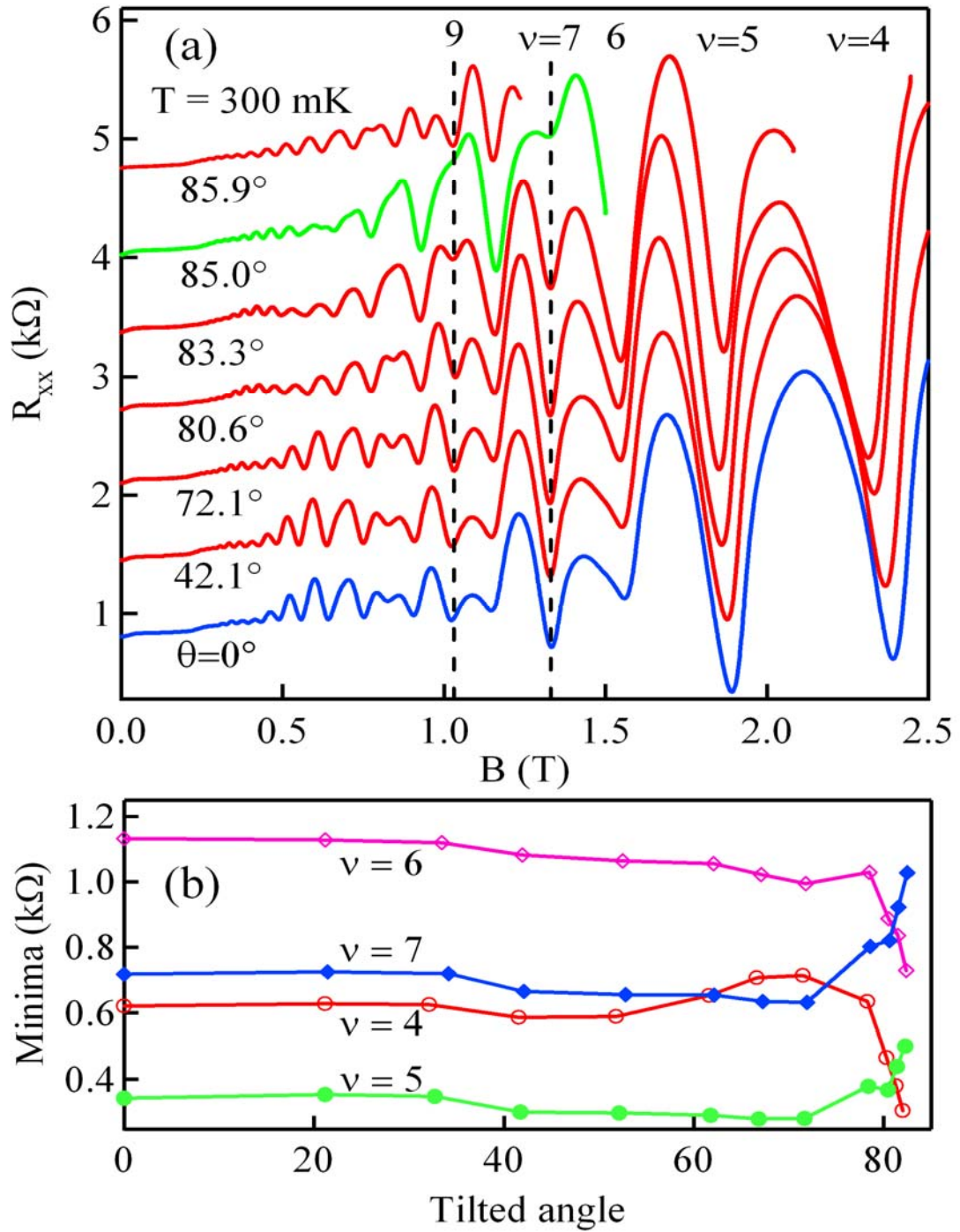
Fig. 0.9 (a) Magnetoresistance traces of selected tilted angles. Traces were shifted up vertically for clarity. Coincidences for minima of $v = 9$ occur at tilted angle $\theta = 85.0°$. (b) Development of minima of R_{xx} of $v = 4, 5, 6, 7$ with increasing tilted angle, in which odd minima increase while even ones decrease.

4.3. GR on 2DHG with triangular antidot lattice

The sample is also cleaved from 2DHG wafer 10-21-03.1, having size of 3 mm × 5 mm and following the same procedure of introducing an antidot lattice on a 2DEG sample. After an 80-µm-wide, 320-µm-long Hall bar was defined on the sample, a triangular antidot lattice, with period of a = 1500 nm and dot diameter of d = 300 nm, was patterned on the Hall bar. After the lithographical processing, the 2DHG has a hole density of $p \approx 2.1 \times 10^{11}$ cm^{-2} and a mobility of $\mu \approx 0.3 \times 10^6$ cm^2/Vs at 300 mK. The hole density was calculated from period of SdH oscillations and mobility was calculated from zero field resistivity. Note that the introduction of antidot lattice reduced mobility more than twice. However, the transport mean free path corresponding to this mobility, $l = m^* \upsilon_F \mu / e$, where m^* is hole effective mass and υ_F is the Fermi velocity, is equal to 2.4 µm, larger than the lattice period a.

Our measurement was performed in He^3 refrigerator equipped with an 12-T superconducting magnet. The magnetoresistance R_{xx} is measured with standard low frequency lock-in technique (frequency 23 Hz and excitation current 1 µA). A R_{xx} trace is shown in Fig.4.9, in which clear GR peaks were resolved. Note that in the magnetic field regime of all these peaks, $\omega_c \tau_{tr} < 2\pi$ indicates that no full cyclotron orbit can be completed between two sequential scattering events.

Experimental data show that the first three resolved GR peaks occurs at aspect ratio R_c/a = 0.58, 0.98 and 1.48, respectively. These aspect ratios are consistent with those of "even" peaks in Fig. 3.3, the GR oscillations on 2DEG patterned antidot lattice with same parameters. This consistency implies that runaway orbit mechanism is the dominant contribution to GR oscillations in 2DHG. And the fact that weaker "odd" GR peaks can't

be resolved in 2DHG should result from much lower mobility, about 10 times lower, than 2DEG.
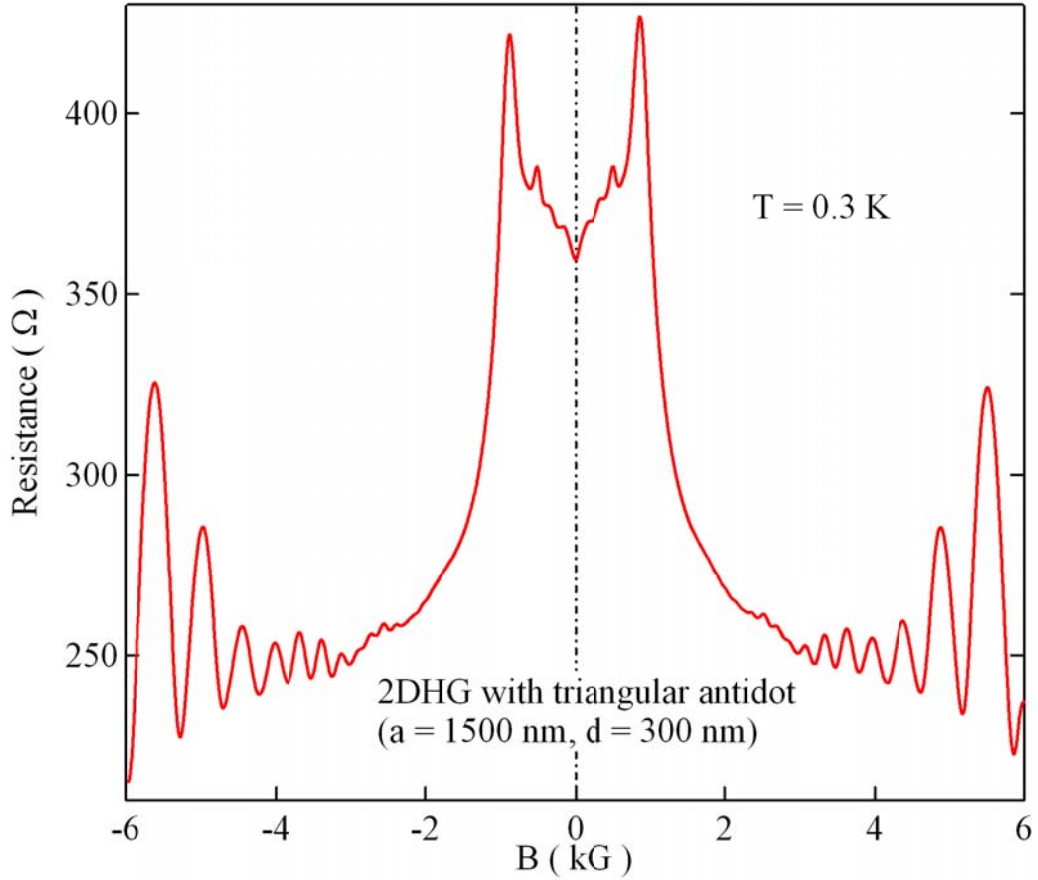
Fig. 0.10 GR on 2DHG with triangular antidot lattice with period a = 1500 nm and dot diameter d = 300 nm. The first two peaks correspond to aspect ratio R_c/a = 0.59 and 1.0, respectively.

4.4. Microwave induced resistance oscillations on 2DHG

The 2DHG sample for MW photoresistance measurement is the same one used for gate characterization. It's a 20 squares 100 μm Hall bar with a 100-nm-thick NiCr front gate and has a hole density of $p \approx 2.2 \times 10^{11}$ cm^{-2} and a mobility of $\mu \approx 0.7 \times 10^6$ cm^2/Vs

at 300 mK. The measurements were performed in an Oxford He^3 refrigerator, equipped with a 12 T superconducting magnet, with base temperature of 300 mK. DC voltage can be applied to the gate to change density of 2DHG. For the photoresistance measurement, the mutual orientation of the waveguide, sample, and the magnetic field corresponds to Faraday configuration in which the excitation current flows perpendicularly to the microwave polarization. As the Cr-gate is not transparent for MW, MW irradiation has to hit on 2DHG from backside of sample. The magnetoresistance R_{xx} is measured with standard low frequency lock-in technique (frequency 23 Hz and excitation current 1 µA).

Without applying gate voltage, MIRO were hardly resolved. After negative gate voltage was applied on the gate, resulting in an increase on hole density and decrease on mobility, MIRO could be observed with a heavily damped amplitude [17]. The magnetoresistance traces without and with MW irradiation at $f = 26.5$ GHz are shown in Fig.4.10. The parameters of hole density $p \approx 3.5 \times 10^{11}$ cm^{-2} and mobility of $\mu \approx 0.35 \times 10^6$ cm^2/Vs were achieved by applying -1 V gate voltage. From position of the first-order MIRO peak, a hole effective mass, $m^* \cong 0.26$, can be deduced from formula (2.24) $\omega_{MW} = \omega_c$. Two features of MIRO on 2DHG shall be emphasized.

First, the deduced hole effective mass, $m^* \cong 0.26$, is much smaller than the value, $m^* \cong 0.4$ measured by cyclotron resonance. The possible reason for the discrepancy is that under applied gate voltage, inversion symmetry of the square quantum well is totally broken, resulting in a larger zero field spin splitting. Thereby the difference between effective masses of heavy and light holes will increase. The light hole shall be responsible for the observed MIRO peak because of its higher mobility.

Second, it is puzzling that MIRO is very weak on 2DHG which has transport time of $\tau_{tr} \sim 50$ ps, comparable with that of 2DEG with mobility 1.0×10^6 cm^2/Vs. A 2DEG with that mobility value will show much stronger MIRO. This fact implies that the complicated band structure of 2DHG might have suppressing effect on MIRO.
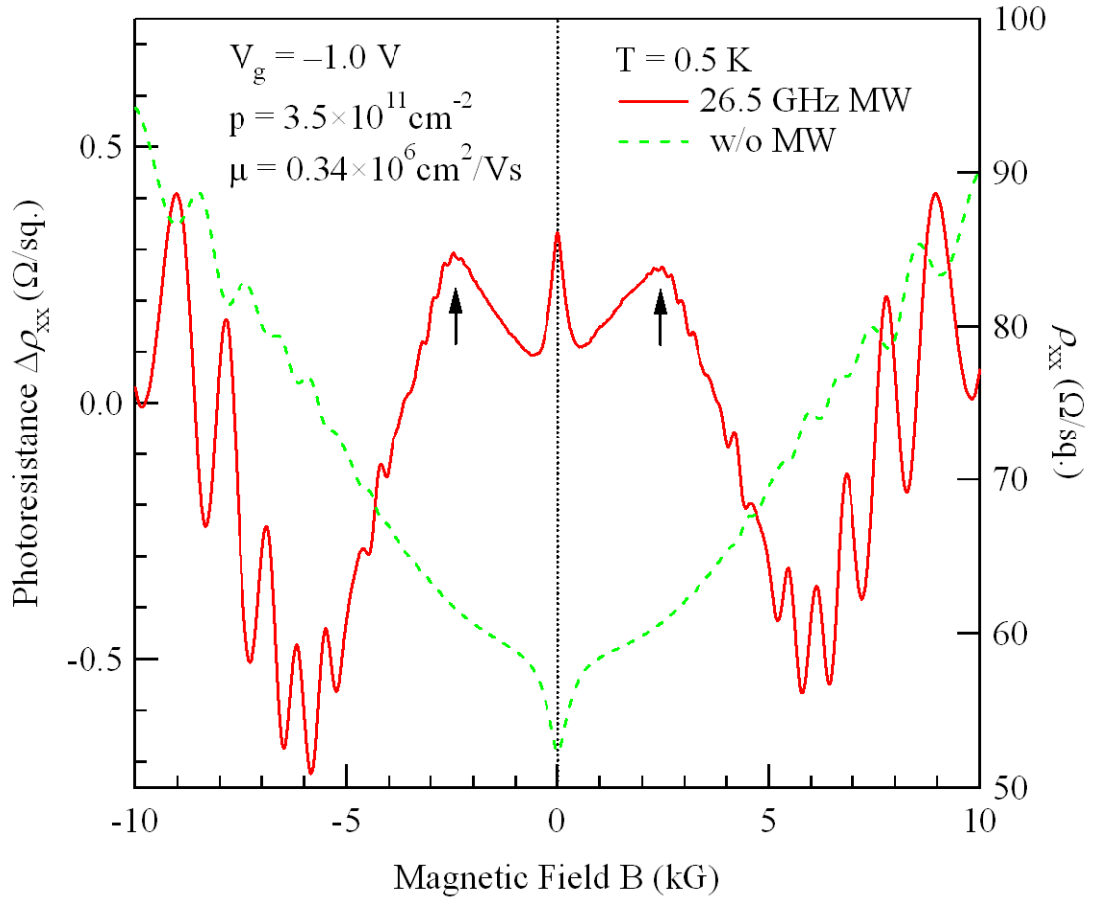
Fig. 0.11. Microwave induced oscillation on 2DHG (solid line). Only one MIRO peak is resolved, marked by arrows. Hole effective mass $m^* \cong 0.26$ can be deduced from position of MIRO peak. Dashed line is magnetoresistance without MW irradiation.

Chapter Five Imaging charge flow distribution

5.1. Motivation and problems

To understand the novel zero-resistance state [10, 11], Andreev *et al* suggested that the ZRS should directly result from absolute negative conductivity (ANC) whose instability would cause a development of local current density with specific magnitude j_0 circulating almost everywhere of the system except some small volume singular regions, such as domains, or vortices of current. The magnitude j_0 is determined by the condition that the component of electric field parallel to local current vanishes. Consider magnetoresistance measurement on a Hall bar geometry. Excitation current, I, passes along x direction, and longitudinal and Hall voltages are measured by V_x and V_y, respectively. Fig.5.1 shows the simplest possible pattern of singular regions:
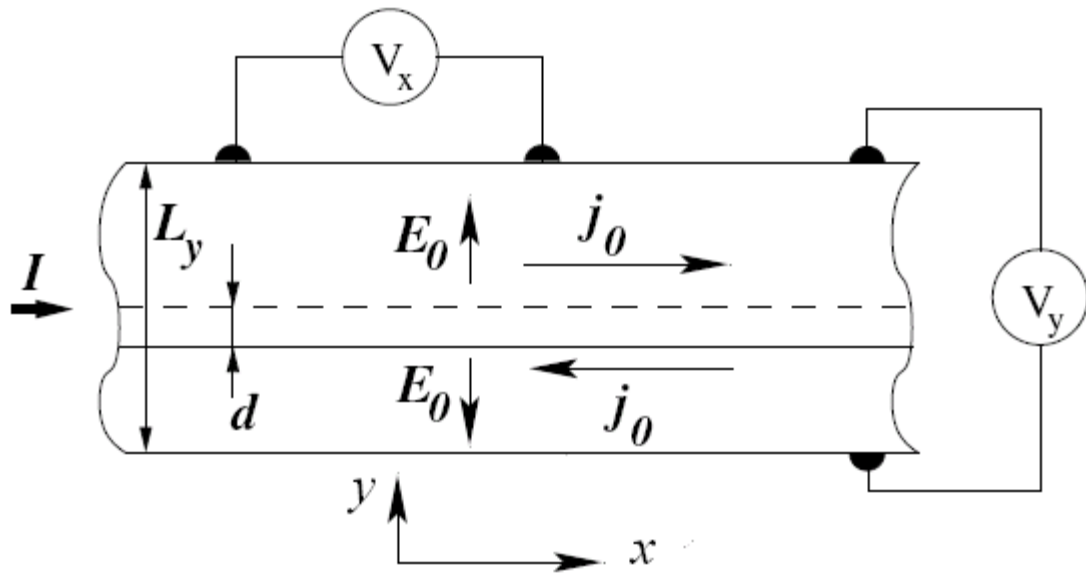
Fig. 0.1. Diagram of the simplest possible pattern of the current distribution: domain wall. The net current, I, is accommodated by a shift of the position of the domain wall by the distance d. (figure adapted from Ref.14)

two current domains separated by a domain wall, located at position d relative to the center of Hall bar. Thus the net current I can be obtained by $I = 2j_0d$. The condition of formation of current domains, $\rho_L(j_0^2) = 0$ with ρ_L the longitudinal resistivity, naturally gives $V_x = 0$ and Hall voltage is given by $V_y = \rho_H[(L_y/2 - d)j_0 + (L_y/2 + d)j_0] = -\rho_H j_0$ with ρ_H the Hall resistivity, which is the classical Hall voltage.

Based on the current domain picture, understanding of ZRS will involve two following tasks: (a) microscopic mechanism giving rise to ANC; (b) proof of existence of current domains. The knowledge of the current distribution of ZRS is the key to solve these two problems. And imaging of current distribution is thought to be the most straightforward method to achieve information of current distribution while is proven to be experimentally very challenging. In the following sections, an introduction of developing a method to image current distribution by using low temperature (0.3 K) scanning Hall probe microscopy will be presented.

5.2. Algorithm of rebuilding current distribution from magnetic field

So far, there is no direct method to measure current distribution. One feasible method is to measure the magnetic field produced by the current density and recover the current distribution from the measured magnetic field. In three dimensional case, there is no unique solution for problem of determination of current distribution from measured magnetic field. Fortunately, if current is confined to a two dimensional system, the problem can be solved uniquely. B. J. Roth *et al* [148] developed a mathematical algorithm based on the Fourier transform technique to obtain the 2D current distribution from measured perpendicular component of the magnetic field.

Assume that a static current density $J(r)$ lies entirely in a very thin sheet of thickness d lying in the x-y plane and the magnetic field produced by the current density is $B(r)$. The thickness d shall be small enough so that we can treat the current distribution as two dimensional. As no current sink and source exist in the region, the current density shall obey the equation of continuity:

$$\nabla \cdot J(r) = 0 \tag{5.1}$$

And the magnetic field produced by the current density is given by:

$$B(r) = \frac{\mu_0}{4\pi} \int \frac{J(r') \times (r - r')}{|r - r'|^3} d^3 r' \tag{5.2}$$

Then the z component of the magnetic field is given by:

$$B_z(x, y, z) = \frac{\mu_0 d}{4\pi} \int_{-\infty}^{+\infty} \int_{-\infty}^{+\infty} \frac{J_x(x', y')y - J_y(x', y')x}{[(x - x')^2 + (y - y')^2 + (z - z')^2]^{3/2}} dx' dy' \tag{5.3}$$

With the convolution theorem [149], we can get the Fourier transform of Eq. (5.1) and Eq. (5.3) as following:

$$k_x j_y(k_x, k_y) + k_y j_x(k_x, k_y) = 0 \tag{5.4}$$

$$b_z(k_x, k_y, z) = -\left(\frac{\mu_0 d}{2}\right) e^{-z\sqrt{k_x^2 + k_y^2}} \cdot \frac{k_y j_x(k_x, k_y) - k_x j_y(k_x, k_y)}{\sqrt{k_x^2 + k_y^2}} \tag{5.5}$$

where k_x, k_y are x, y components of wave vector and j_x, j_y, b_z are the Fourier transforms of J_x, J_y and B_z respectively. Theoretically, j_x, j_y can be solved uniquely from Eqs. (5.4) and (5.5), and then J_x, J_y can be obtained by performing inverted Fourier transformation of j_x, j_y.

To apply this mathematical algorithm to numerical calculation, we did not use the infinite sheet. Instead we considered a L x L square area in which there are N sampled points in each x, y direction. Thereby the distance between adjacent points in real space is $\Delta x = \Delta y = L/N$ and in k-space is $\Delta k_x = \Delta k_y = 2\pi/(N\Delta x)$. The one dimensional discrete form of Fourier Transformation is given by:

$$b_z(k_m) = FFT[B_z(x)] = \sum_{n=1}^{N} B_z(x_n)e^{-\frac{2\pi i}{N}(n-1)(m-1)} \qquad (5.6)$$

$$B_z(x_n) = iFFT[b_z(k)] = \frac{1}{N}\sum_{m=1}^{N} b_z(k_m)e^{\frac{2\pi i}{N}(n-1)(m-1)} \qquad (5.7)$$

where FFT and iFFT are Fast Fourier and inverted Fast Fourier Transformations. Choose N as an even number and x_n, k_m as following forms:

$$x_n = \left(n - 1 - \frac{N}{2}\right) \cdot \Delta x \qquad (5.8)$$

$$k_m = \left(m - 1 - \frac{N}{2}\right) \cdot \Delta k \qquad (5.9)$$

Thus summation can be used as an approximation of the integral of the Fourier Transform:

$$b_z(k_m) = \int B_z(x)e^{ikx}dx = \sum_{n=1}^{N} B_z(x_n)e^{ik_m \cdot x_n} \cdot \Delta x \qquad (5.10)$$

Making use of Eqs. (5.8), (5.9), we can get,

$$b_z(k_m) = Le^{-(m'-1)\pi i}\frac{1}{N}\sum_{n=1}^{N}B_z(x_n)e^{\frac{2\pi i}{N}(m'-1)(n-1)} = Le^{-(m'-1)\pi i}\cdot iFFT(B_z) \quad (5.11)$$

where $m'=m-N/2$. With the same manipulations, we can get $J(x)$ from $j(k)$.

$$J(x_n) = \int j(k)e^{-ikx}dk = \sum_{m=1}^{N}j(k_m)e^{-ik_m\cdot x_n}\cdot\Delta k = \frac{1}{L}e^{(n-1)\pi i}FFT(j) \quad (5.12)$$

Eqs. (5.11) and (5.12) are the basic formula used in programming of simulation.

The flow chart of the simulation is following. MatLab codes of the program can be found in Appendix A5, A6 and A7.
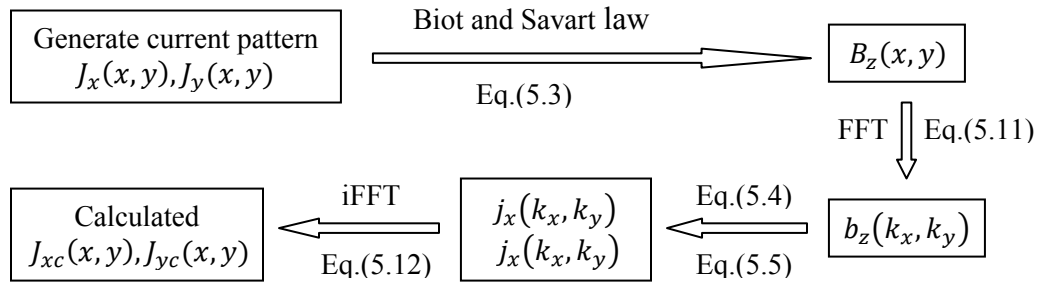
5.3. Simulation results

1). Create a 2D current distribution, shown in Fig.5.2.

This is 16 um × 16 um square area with 128 sampled points in each *x, y* direction, in which there are ring currents with ring diameter 1 um and arbitrary amplitudes satisfying the continuity condition.
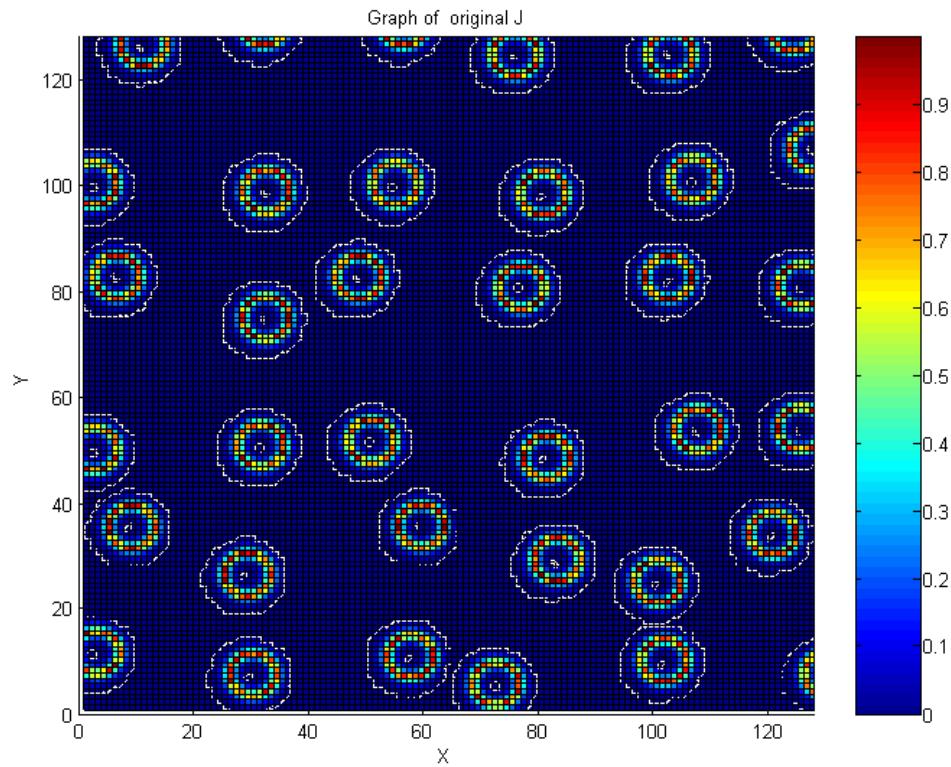
Fig. 0.2 Original current distribution.

2). Calculate the perpendicular component, B_z, of magnetic field.

The magnetic field is produced by this current density at z = 100, 200, 300 nm by Biot-Savart law, Eq. (5.3), and then calculate the current distribution from the above B_z data with the mathematical algorithm. The results are shown in Fig.5.2 and 5.3. From the simulation results, we can see that the algorithm is working and the distance z is a very important parameter for the simulation. In order to recover the original current distribution $J(x,y)$, the scanning range has to be at least 50 times bigger than z. The bigger is the scanning area, the better will the current distribution be recovered.
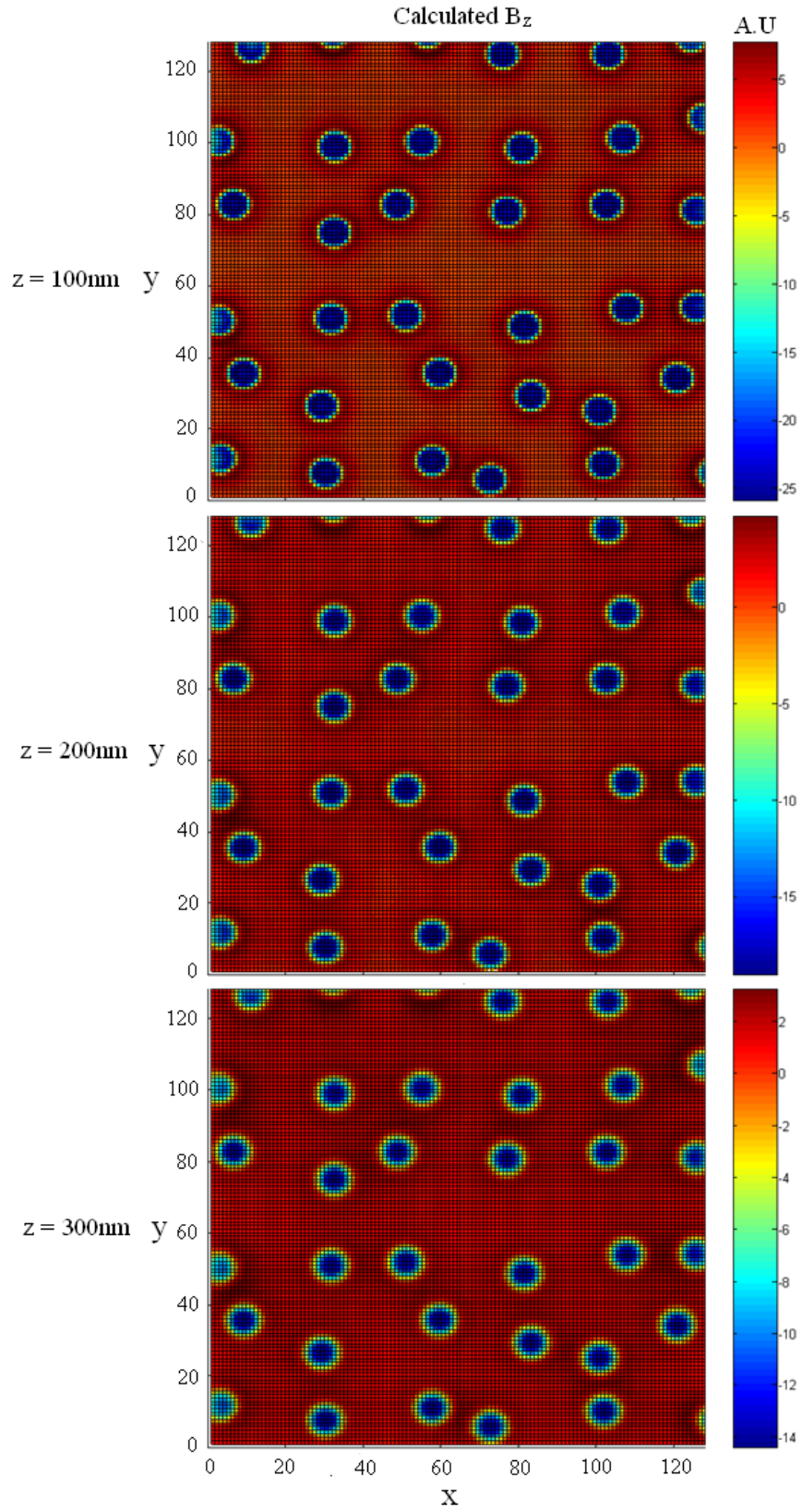
Fig. 0.3. Mappings of calculated Bz of z = 100, 200 and 300 nm.
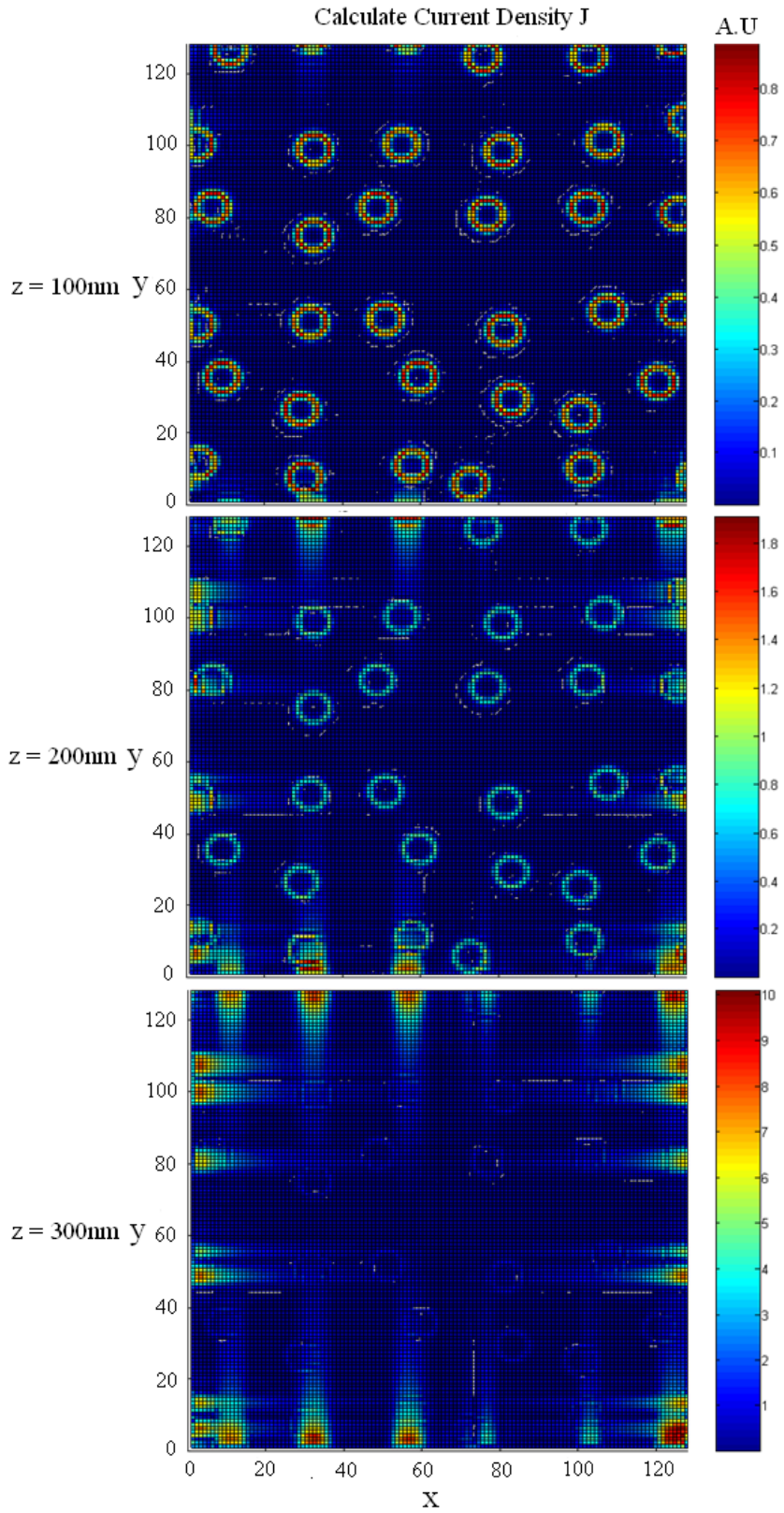
Fig. 0.4. Mappings of Calculated current density J of z = 100, 200 and 300 nm.

5.4. Estimate amplitude of magnetic field produced by cyclotron orbits

In order to address appropriate technique to measure the magnetic field produced by current, we need to estimate the magnitude of the magnetic field. Assume that current I is going through a ring with radius R. Then the magnetic field at ring center is given by:

$$B_c = \frac{\mu_0 I}{2\pi R}$$

A 2DEG under external magnetic field, B_{ex}, the total number of occupied Landau levels can be estimated by $N_{LL} \approx E_F / \hbar\omega_c$. Thus the portion of electron density at the top occupied Landau is:

$$\Delta n_s = \frac{n_{2D}}{N_{LL}} = \frac{n_{2D} \cdot \hbar\omega_c}{E_F}$$

At geometric resonance, the cyclotron orbits, with radius r_c, of electrons are pinned around the antidots. Thus the current caused by one electron is $I_e = ef_c = e\,\omega_c/2\pi$ and magnetic field at the center of the orbit produced by the electron is:

$$B_e = \frac{\mu_0 I_e}{2\pi r_c}$$

We suppose that all electrons on an area of $2r_c \times 2r_c$ around an antidot will form cyclotron orbits with same radius centered at this antidot and all electrons in the top occupied Landau level are involved in forming cyclotron orbits. So the number of electrons circling around one antidot is given by:

$$N = \Delta n_s \cdot (2r_c)^2$$

Therefore the total magnetic field at the center of these orbits is N times of B_e. On our 2DEG *GaAs* sample with density $n_{2D} \cong 2.8 \times 10^{11} \text{cm}^{-2}$, the Fermi level $E_F \cong 10\text{meV}$

and the first geometric resonance peak occurs at B_{ex} = 0.1 T with orbit radius of 1 μm, then the current produced by single electron is:

$$I_e = ef_c \approx 7nA$$

The number of electrons circling one antidot is $N \approx 200$. Hence the magnetic field at the orbit center: $B \approx 3$mGauss.

When the magnetic field on the orbit axis, but away from the orbit surface with distance z, then the magnetic field is given by:

$$B_z = \frac{\mu_0}{2} \cdot \frac{r_c^2 I}{(z^2 + r_c^2)^{3/2}}$$

Therefore, the perpendicular component of magnetic field we need to measure shall be no larger than 3 mGuass.

5.5. Scanning Hall Probe Microscope

To meet out requirements of measuring perpendicular component of magnetic field, low temperature Scanning Hall Probe Microscope (SHPM) which was developed by Chang, *et al* [150] is the most promising technique. The Scanning Hall Probe Microscope works based on Hall effect in which a Hall voltage, V_H, cross to excitation current, I, will be produced by a magnetic field, B, perpendicular to electron system, as shown in Fig.5.5. And V_H will be determined by

$$V_H = R_H \frac{I}{d} B \quad (5.13)$$

where R_H is Hall coefficient, an intrinsic property of the electron system. Thereby, magnetic field can be measured by measured Hall voltage. There are two main advantages of Hall Probe technique.

a). Unlike Magnetic Force Microscope responding to total magnetic field, the SHPM only responds to the component of magnetic field perpendicular to the probe. This is a perfect match to our requirements.

Fig. 0.3. Diagram of Hall effect.

b). SHPM has no saturation in high magnetic field, which is important for measurement performed in existence of external magnetic field.

The main shortage of SHPM is difficult to fabricate a small size Hall sensor with high sensitivity. In a small Hall sensor, mixture between longitudinal voltage and Hall voltage become serious so that magnetic field sensitivity will be strongly limited.

Fig. 0.6. Schematic diagram of Scanning Hall Probe Microscope. (figure from Ref. 151)

A typical structure of SHPM is shown in Fig.5.6. Photos of a real SHPM and Hall probe are shown in Fig.5.7 and 5.8. The SHPM was bought from Nanomagnetics Instruments and has following features:

❖ Scanning Tunneling Microscope (STM) positioning technique to control distance between Hall probe and sample surface. This STM tip is fabricated near the Hall probe section, as shown in Fig. 5.8. This STM positioning mechanism requires the sample surface shall be conductive.

❖ Use piezoelectric tube (PZT) to control scanning of Hall probe in XYZ directions. There are two separated parts working for step-moving: a big piezoelectric tube for Z direction, and a stack of two Attocube piezoelectric positioners for XY directions. As shown in Fig. 5.7, a slider is sitting around and can slide along the slider glass tube. The big PZT can make the slider move more than 10 mm on the slider glass tube and

has capability of moving mass up to 100 grams. The Attocube positioners are mounted on the slider and sample holder is mounted on the top positioner, so movement of slider results in sample moving in Z direction. And the positioners can provide up to 4 mm travel length in X and Y directions and have step size ranging from 3 nm to 50 nm, depending on applied voltage, at 4.2K.

❖ Have submicron spatial resolution. This spatial resolution is totally determined by size of Hall probe section. For our Hall probe sensors, the section has size of 1μm × 1μm, as shown in Fig.5.8.

❖ Achieve 16μm × 16μm scanning range at low temperature, down to 1 K.
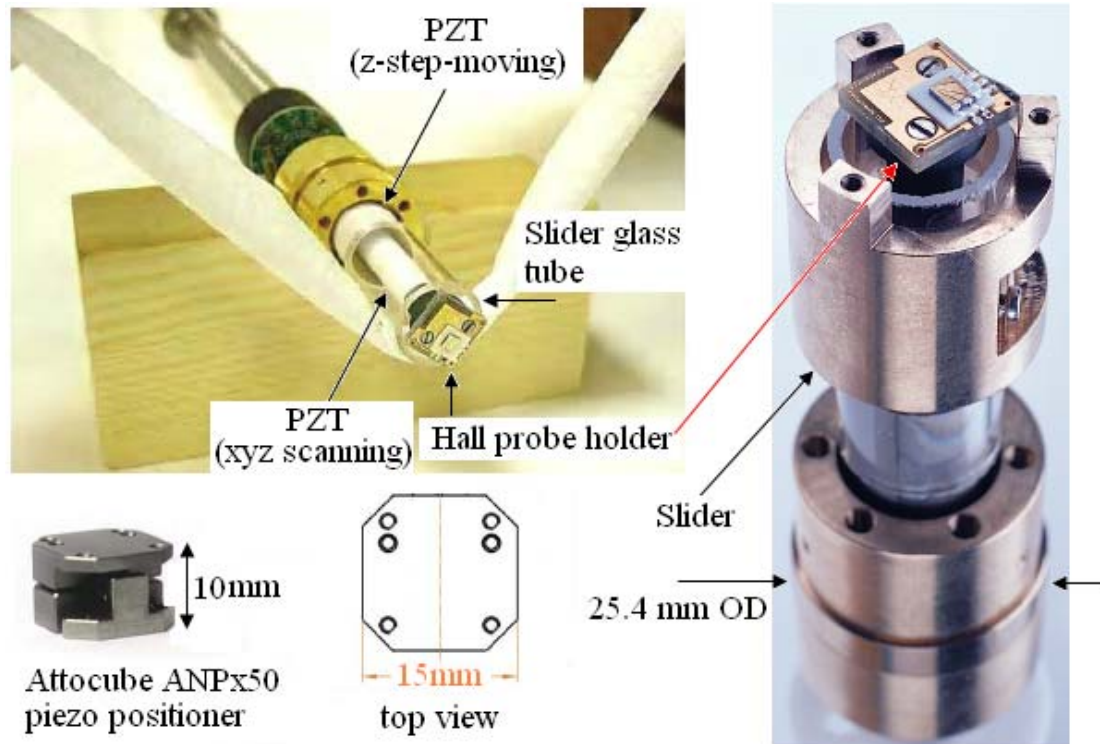
Fig. 0.4. Photos of our SHPM. The slider is sitting around and can move along the slider glass tube. A stack of two positioners is mounted on the slider and sample holder will be mounted on the top positioner.
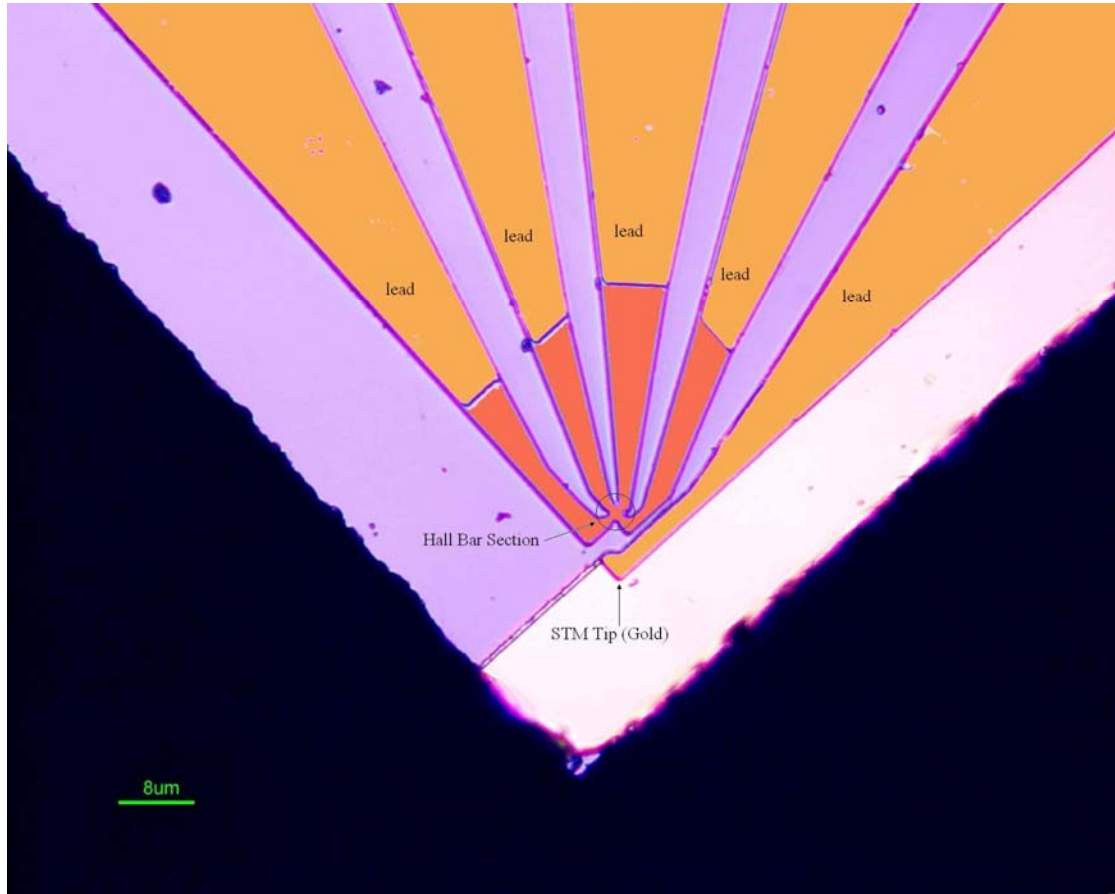
Fig. 0.8. Photos of Hall probe. In this Hall probe, the section of Hall probe has size of 1μm ×
1μm, and the gold STM tip is used for positioning.

Two images of magnetic field of a piece of hard disc at T = 300 K and 1 K are shown
in Fig.5.9. The curves below images are magnetic field profiles along the lines on images.
The noise on profiles indicates that the magnetic field resolution is about 1 G. To
calibrate the sensitivity of Hall sensors, we made a 10 mm long solenoid with diameter of
8.5 mm and put the Hall sensor at the center of the solenoid. If current of 1 A passes
through the solenoid, magnetic field at the center will be 25.5 G. With this calibration
setup, we can measure the sensitivity of Hall sensor around 200 mG at T ~ 1 K. After
employing lockin technique, the resolution could be improved to about 50 mG. This

sensitivity is still much lower than our requirement, about 1 mG. Therefore, further improvement on Hall sensor sensitivity is essential for success of imaging of current distribution of zero-resistance-state.
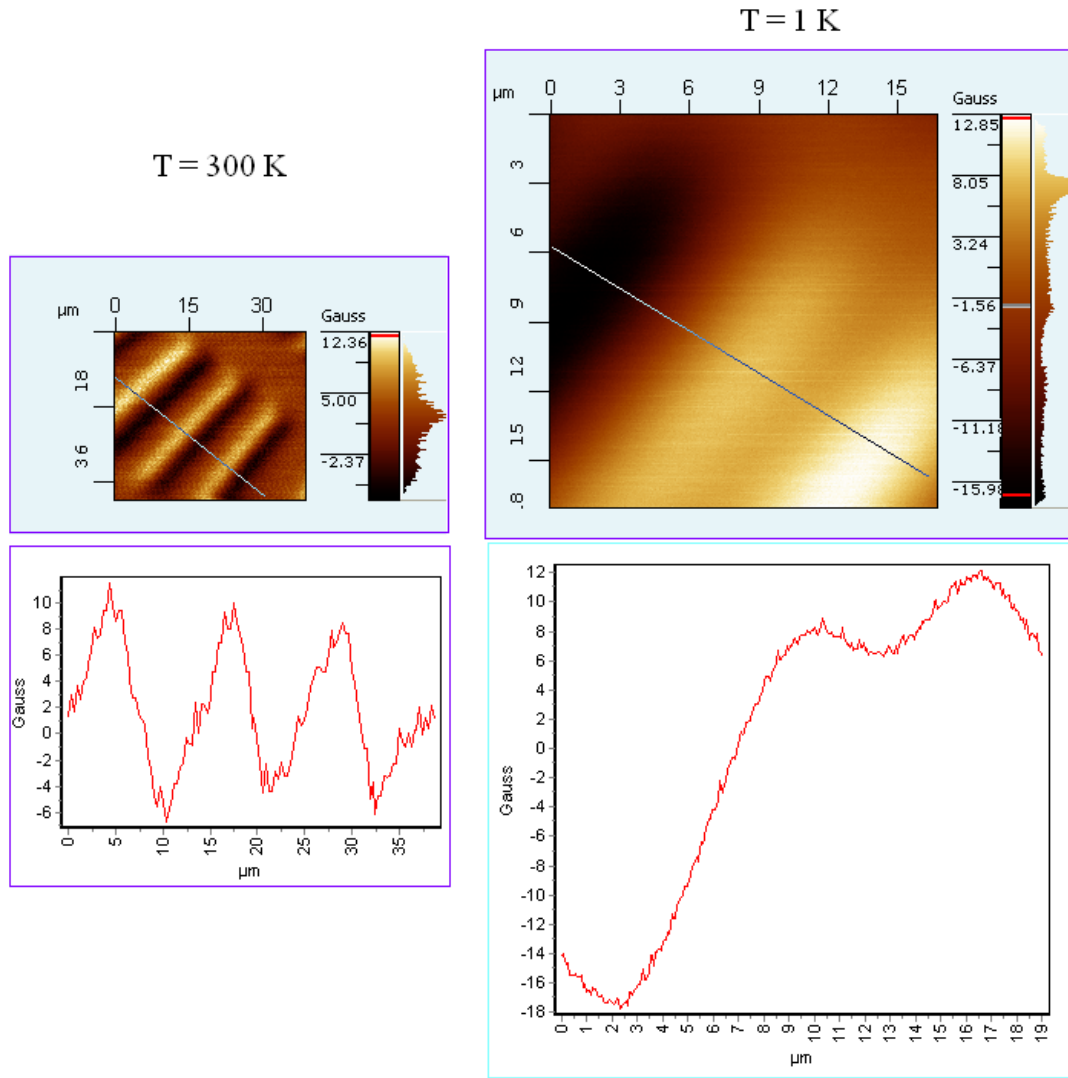
Fig. 0.5. SHPM images of magnetic field of a piece of hard disc at T = 300 K and 1 K, respectively. The curves below images are magnetic field profiles along the lines on images.

Chapter Six Conclusion

In this thesis, we reported our experimental studies on the microwave photoresistance in a high-mobility 2DEG modulated by a 2D triangular potential. The geometric resonance observed in the sample is remarkably different from previous systems of lower mobility. We observed microwave-induced resistance oscillations and magnetoplasmon resonance that are characteristically similar to those of unpatterned 2DEG. Our data shows that MIRO, MP, and geometric resonance are essentially decoupled from each other in these experiments. Ultimately, one would like to pursue the experimental regime where periodical modulation would lead to characteristically new behavior in the MIRO and ZRS. Along this line, a clean 2D electron system consisting of a short modulation period approaching magnetic length would offer exciting opportunities. Moreover, the issue concerning scattering parameters and their influences in the microwave photoresistance remains open for experimental as well as theoretical work.

To characterize transport properties of 2DHG in C-doped (100) GaAs/Al$_{0.4}$Ga$_{0.6}$As square QW, we measured the effective mass of the 2DHG with MW CR technique. Only one effective mass, $m^* \cong 0.4$, was detected due to small zero-field spin splitting, which was confirmed in Fourier transformation spectrum of beating pattern in SdH oscillations. Values of transport scattering time, τ_{tr} and cyclotron relaxation time, τ_{CR} prove the cleanness of this 2DHG QW from modulation doping. Magnetoresistance measurements under tilted magnetic field indicate that at $B \sim 1\ T$, the g-factor of 2DHG is large enough to cause Landau level crossing, and by increasing the total magnetic field, the product gm^* increases. This mainly results from an increase of m^*. Magnetotransport measurements on a gated 2DHG indicates that due to screening effect of doping layer,

front gate doesn't work reliably and the density can only be changed without shift back beyond a threshold gate voltage, about -1.0 V. Magnetotransport measurements on 2DHG modulated with 2D triangular antidot lattice shows strong geometric resonance oscillations whose pattern is consistent with that in high mobility 2DEG. MW photoresistance measurements on a gated 2DHG shows microwave induced resistance oscillations with heavy magnetic field damping on amplitudes and is much weaker than that in 2DEG having comparable transport scattering time. This finding implies that the complicated band structure of 2DHG might have suppression effect on MIRO. And the deduced effective mass from MIRO peak indicates that zero field spin splitting increases under applied gate voltage.

In order to explore the existence of domain of current density in of zero-resistance state, we develop a technique to image current distribution. The technique is consisted of two parts: an algorithm to calculate current distribution from measured magnetic field and low temperature Scanning Hall Probe Microscope to measure the magnetic field. So far, the only obstacle is limit of sensitivity of Hall sensor. From our estimation, the magnetic field needed to be measured has order of 1 mG, while current Hall sensor only achieves sensitivity about 50 mG. Hence success of current distribution imaging totally relies on the future improvement on the sensitivity of Hall sensor.

Reference

1. **K. von Klitzing, G. Dorda and M. Pepper.** Phys. Rev. Lett. 45, 494 (1980).

2. **D. C. Tsui, H. L. Stormer, and A. C. Gossard.** Phys. Rev. Lett. 48, 1559 (1982).

3. **Sankar Das Sarma and Aron Pinczuk.** *Perspectives in Quantum Hall Effects: Novel Quantum Liquids in Low-Dimensional Semiconductor Structures.* Wiley-Interscience, New York, 1996.

4. **D. Weiss, K. von Klitzing, K. Ploog and G. Weimann.** Europhys. Lett. 8 (2), 179 (1989).

5. **R. R. Gerhardts, D. Weiss and K. v. Klitzing.** Phys. Rev. Lett. 62, 1173 (1989).

6. **R. W. Winkler, J. P. Kotthaus, and K. Ploog.** Phys. Rev. Lett. 62, 1177 (1989).

7. **D. Weiss, M. L. Roukes, A. Menschig, P. Grambow, K. von Klitzing, and G. Weimann.** Phys. Rev. Lett. 56, 2790 (1991).

8. **M. A. Zudov, R. R. Du, J. A. Simmons and J. L. Reno.** Phys. Rev. B64, 201311 (2001).

9. **P. D. Ye, L. W. Engel, D. C. Tsui, J. A. Simmons, J. R. Wendt, G. A. Vawter and J. L. Reno.** Appl. Phys. Lett. 79, 2193 (2001).

10. **R. G. Mani, J. H. Smet, K. von Klitzing, V. Narayanamurti, W. B.Johnson, and V. Umansky.** Nature (London) 420, 646 (2002).

11. **M. A. Zudov, R. R. Du, L. N. Pfeiffer, and K. W. West.** Phys. Rev. Lett. 90, 046807 (2003).

12. **C. L. Yang, M. A. Zudov, T. A. Knuuttila, R. R. Du, L. N. Pfeiffer, and K. W. West.** Phys. Rev. Lett. 91, 096803 (2003).

13. **Z. Q. Yuan, C. L. Yang, R. R. Du, L. N. Pfeiffer, and K. W. West.** Phys. Rev. B 74, 075313 (2006).

14. **A. V. Andreev, I.L. Aleiner and A.J. Millis.** Phys. Rev. Lett. 91, 056803 (2003).

15. **H. L. Stormer, Z. Schlesinger, A. Chang, D. C. Tsui, A. C. Gossard, and W. Wiegmann.** Phys. Rev. Lett 51, 126 (1983).

16. **M. B. Santos, Y. W. Suen, M. Shayegan, Y. P. Li, L. W. Engel, and D. C. Tsui.** Phys. Rev. Lett. 68, 1188 (1992) .

17. **R. R. Du, M. A. Zudov, C. L. Yang, Z. Q. Yuan, L. N. Pfeiffer, and K. W. West.** *Oscillatory and Vanishing Resistance States in Microwave Irradiated 2D Electron Systems.* Proceedings of the 16th International Conference on High Magnetic Fields in Semiconductor Physics, eds. Y.-J. Wang, L. Engel, N. Bonesteel, World Scientific, Singapore, 2005.

18. **J. P. Harrang, R. J. Higgins, R. K. Goodall, P. R. Jay, M. Laviron and P. Delescluse.** Phys. Rev. B 32, 8126 (1985).

19. **John H. Davies.** *The Physics of Low-Dimensional Semiconductors.* Cambridge University Press, New York, 1998.

20. **Roth, P. N. Argyres and L. M.** J. Phys. Chem. Solids 12, 89 (1959).

21. **C. L. Yang.** Doctoral Thesis, Univ. of Utah (2005).

22. **S. Titeica.** Ann. Phys. (Leipzig) 22, 129 (1935).

23. **C. W. J. Beenakker.** Phys. Rev. Lett. 62, 2020 (1989).

24. **P. Vasilopoulos, and F. M. Peeters.** Phys. Rev. Lett. 63, 2120 (1989).

25. **F. M. Peeters, and P. Vasilopoulos.** Phys. Rev. B 46, 4667 (1992).

26. **K. Ensslin and P. M. Petroff.** Phys. Rev. B 41, 12307 (1990).

27. **R. R. Gerhardts, D. Weiss, and U. Wulf.** Phys. Rev. B 43, 5192 (1991).

28. **A. Lorke, J. P. Kotthaus,and K. Ploog.** Phys. Rev. B 44, 3447 (1991).

29. **F. Nihey, S. W. Hwang, and K. Nakamura.** Phys. Rev. B 51, 4649 (1995).

30. **E. Vasiliadou, R. Fleischmann, D. Weiss, D. Heitmann, K.von Klitzing, T. Geisel, R. Bergmann, H. Schweizer, C. T.Foxon.** Phys. Rev. B 52, R8658 (1995).

31. **H. Fang and P. J. Stiles.** Phys. Rev. B 41, 10171 (1990).

32. **T. Yamashiro, J. Takahara, Y. Takagaki, K. Gamo, S.Namba, S. Takaoka, and K. Murase.** Solid State Commun.79, 885 (1991).

33. **J. Takahara, T. Kakuta, T. Yamashiro, Y. Takagaki, T. Shiokawa, K. Gamo, S. Namba, S. Takaoka, and K. Murase.** J. Appl. Phys. 30, 3250 (1991).

34. **R. R. Gerhardts.** Phys. Rev. B 45, 3449 (1992).

35. **E. M. Baskin, G. M. Gusev, Z. D. Kvon, A. G. Pogosov, and M.V. Entin.** JETP Lett. 55, 678 (1992).

36. **R. Fleischmann, T. Geisel, and R. Ketzmerick.** Phys. Rev. Lett. 68, 1367 (1992).

37. **D. Pfannkuche and R. R. Gerhardts.** Phys. Rev. B 46, 12606 (1992).

38. **A. V. Vagov.** Phys. Rev. B. 51, 5065 (1995).

39. **S. Ishizaka, F. Nihey, K. Nakamura, J. Sone, and T. Ando.** Phys. Rev. B 51, 9881 (1995).

40. **S. Ishizaka, and T. Ando.** Phys. Rev. B 55, 16331 (1997).

41. **S. Ishizaka, and T. Ando.** Phys. Rev. B 56, 15195 (1997).

42. **R. Neudert, P. Rotter, U. Rössler, and M. Suhrke.** Phys. Rev. B 55, 2242 (1997).

43. **T. Ando, et al.** *Mesoscopic Physics And Electronics.* Springer-Verlag, Berlin, 1998. Chap. 2.5, pp. 72–76.

44. **A. D. Mirlin, E. Tsitsishvili, and P. Wölfle.** Phys. Rev. B 63, 245310 (2001).

45. **R. R. Gerhardts, and S. D. M. Zwerschke.** Phys. Rev. B 64, 115322 (2001).

46. **A. C. Durst, S. Sachdev, N. Read, and S. M. Girvin.** Phys. Rev. Lett. 91, 086803 (2003); Physica E 25, 198 (2004).

47. **Ryzhii, V. I.** Sov. Phys. Semicond. 20, 1299 (1986).

48. **S. A. Studenikin, M. Potemski, A. Sachrajda, M. Hilke, L. N. Pfeiffer, and K. W. West.** Phys. Rev. B 71, 245313 (2005).

49. **F. Stern.** Phys. Rev. Lett. 18, 546 (1967).

50. **E. Vasiliadou, G. Muller, D. Heitmann, D.Weiss, K. von Klitzing, H. Nickel, W. Schlapp, and R. Losch.** Phys. Rev. B 48, 17145 (1993).

51. **S. I. Dorozhkin.** JETP Lett. 77, 577 (2003).

52. **R. L. Willett, L. N. Pfeiffer, and K. W. West.** Physical Review Letters 93 026804 (2004).

53. **I. V. Kukushkin, M. Yu. Akimov, J. H. Smet, S. A. Mikhailov, K. von Klitzing, I. L. Aleiner, and V. I. Falko.** Phys. Rev. Lett. 92, 236803 (2004).

54. **M. A. Zudov.** Phys. Rev.B 69, 041304 (2004).

55. **R. R. Du, M. A. Zudov, C. L. Yang, Z. Q. Yuan, L. N. Pfeiffer, and K. W. West.** Int. J. Mod. Phys. B 18, 3465 (2004).

56. **R. G. Mani, J. H. Smet, K. von Klitzing, V. Narayanamurti, W. B. Johnson, and V. Umansky.** Phys. Rev. B 69, 193304 (2004); Phys. Rev. Lett. 92, 146801 (2004).

57. **R. G. Mani, V. Narayanamurti, K. von Klitzing, J. H. Smet, W. B. Johnson, and V. Umansky.** Phys. Rev.B 69, 161306(R) (2004); ibid. 70, 155310 (2004).

58. **S. A. Studenikin, M. Potemski, P. T. Coleridge, A. Sachrajda, and Z. R. Wasilewski.** Solid State Commun. 129, 341 (2004).

59. **R. G. Mani.** Phys. Rev. B 72, 075327 (2005).

60. **J. H. Smet, B. Gorshunov, C. Jiang, L. Pfeiffer, K. West, V. Umansky, M. Dressel, R. Meisels, F. Kuchar, and K. von Klitzing.** Physical Review Letters 95 116804 (2005).

61. **S. I. Dorozhkin, J. H. Smet, V. Umansky, and K. von Klitzing.** Physical Review B 71 201306 (2005).

62. **A. A. Bykov, Jing-qiao Zhang, Sergey Vitkalov, A. K. Kalagin, and A. K. Bakarov.** Physical Review B 72 245307 (2005).

63. **C. L. Yang, R. R. Du, L. N. Pfeiffer, and K. W. West.** Phys. Rev. B 74 045315 (2006).

64. **M. A. Zudov, R. R. Du, L. N. Pfeiffer, and K. W. West.** Phys. Rev. Lett. 96, 236804 (2006).

65. **M. A. Zudov, R. R. Du, L. N. Pfeiffer, and K. W. West.** Physical Review B 73 041303 (2006) .

66. **J.-Q. Zhang, S. Vitkalov, A. A. Bykov, A. K. Kalagin, and A. K. Bakarov.** Phys. Rev. B 75, 081305(R) (2007).

67. **W. Zhang, H.-S. Chiang, M. A. Zudov, L. N. Pfeiffer, and K. W. West.** Phys. Rev. B 75, 041304(R) (2007).

68. **W. Zhang, M. A. Zudov, L. N. Pfeiffer, and K. W. West.** Phys. Rev. Lett. 98, 106804 (2007).

69. **A. T. Hatke, H.-S. Chiang, M. A. Zudov, L. N. Pfeiffer, and K. W. West.** Phys. Rev. B 77, 201304(R) (2008).

70. **K. Stone, C. L. Yang, Z. Q. Yuan, R. R. Du, L. N. Pfeiffer, and K. W. West.** Physical Review B 76 153306 (2007) .

71. **B. Simovič, C. Ellenberger, K. Ensslin, H.-P. Tranitz, and W. Wegscheider.** Physical Review B 71 233303 (2005).

72. **I. A. Dmitriev, A. D. Mirlin, and D. G. Polyakov.** Phys. Rev. Lett. 91, 226802 (2003); ibid.99, 206805 (2007); Phys. Rev. B70, 165305 (2004); ibid. 75, 245320 (2007).

73. **F. S. Bergeret, B. Huckestein and A.F. Volkov.** Phys. Rev. B 67, 241303R (2003).

74. **A. A. Koulakov and M. E. Raikh.** Phys. Rev. B 68, 115324(2003).

75. **J. Shi and X. C. Xie.** Phys. Rev. Lett. 91, 086801 (2003).

76. **V. Ryzhii and R. Suris.** J. Phys.: Condens. Matter 15, 6855 (2003).

77. **V. Ryzhii.** Phys. Rev. B 68, 193402 (2003).

78. **V. Ryzhii and V. Vyurkov.** Phys. Rev. B 68, 165406 (2003).

79. **X. L. Lei and S. Y. Liu.** Phys. Rev. Lett. 91, 226805 (2003); Phys. Rev. B 72, 075345 (2005); Appl. Phys. Lett. 86, 262101(2005); ibid.88, 212109 (2006); ibid. 89, 182117 (2006); ibid.93, 082101 (2008).

80. **J. C. Phillips.** Solid State Commun. 127, 233 (2003).

81. **X. L. Lei.** J.Phys.: Condens. Matter 16, 4045 (2004); Appl. Phys. Lett. 91, 112104 (2007).

82. **M. G. Vavilov and I. L. Aleiner.** Phys. Rev. B 69, 035303 (2004).

83. **I. A. Dmitriev, M. G. Vavilov, I. L. Aleiner, A. D. Mirlin, and D. G. Polyakov.** Physical Review B 71 115316 (2005); Physica E (Amsterdam) 25, 205 (2004).

84. **M. G. Vavilov, I. A. Dmitriev, I. L. Aleiner, A. D. Mirlin, and D. G. Polyakov.** Phys. Rev. B 70, 161306(R) (2004).

85. **S. A. Mikhailov.** Phys. Rev. B 70, 165311 (2004).

86. **K. Park.** Phys. Rev. B 69, 201301(R) (2004).

87. **D. -H. Lee and J. M. Leinaas.** Phys. Rev.B 69, 115336 (2004).

88. **C. Joas, M. E. Raikh, and F. von Oppen.** Phys. Rev. B 70, 235302 (2004).

89. **V. Ryzhii, A. Chaplik, and R. Suris.** JETP Lett. 80, 363 (2004).

90. **J. P. Robinson, M. P. Kennett, N. R. Cooper, and V. I. Falko.** Phys. Rev. Lett. 93, 036804 (2004).

91. **J. Iñarrea and G. Platero.** Phys. Rev. Lett. 94, 016806 (2005); Phys. Rev. B 72, 193414 (2005).

92. **A. Auerbach, I. Finkler, B. I. Halperin, and A. Yacoby.** Phys. Rev. Lett. 94, 196801 (2005).

93. **J. Alicea, L. Balents, M. P. Fisher, A. Paramekanti, and L. Radzihovsky.** Phys. Rev. B 71, 235322 (2005).

94. **J. Dietel, L. I. Glazman, F. W. J. Hekking, and F. von Oppen.** Phys. Rev. B 71, 045329 (2005).

95. **C. Joas, J. Dietel, and F. von Oppen.** Phys. Rev. B 72, 165323 (2005).

96. **M. Torres, and A. Kunold.** Phys. Rev. B 71, 115313 (2005).

97. **M. Torres, and A. Kunold.** J. Phys: Condens. Matter 18, 4029 (2006).

98. **S. A. Mikhailov and N. A. Savostianova.** Phys. Rev. B 71, 035320 (2005); ibid.74, 045325 (2006).

99. **M. P. Kennett, J. P. Robinson, N. R. Cooper, and V. I. Falko.** Phys. Rev. B 71, 195420 (2005).

100. **G. Gumbs.** Physical Review B 72 125342 (2005).

101. **T. K. Ng and L. Dai.** Phys. Rev.B 72, 235333 (2005).

102. **O. E. Raichev and F. T. Vasko.** Phys. Rev. B 73, 075204 (2006).

103. **J. Dietel.** Phys. Rev. B 73, 125350 (2006).

104. **X. L. Lei.** Phys. Rev. B73, 235322 (2006).

105. **A. Kashuba.** Phys. Rev. B 73, 125340 (2006);JETP Lett. 83, 293 (2006).

106. **M. G. Vavilov, I. L. Aleiner, and L. I. Glazman.** Phys. Rev. B 76, 115331 (2007).

107. **A. Auerbach, and G. V. Pai.** Phys. Rev. B 76, 205318 (2007).

108. **J. Iñarrea and G. Platero.** Phys. Rev. B 76, 073311 (2007).

109. **I. V. Pechenezhskii, S. I. Dorozhkin, and I. A. Dmitriev.** JETP Lett. 85, 86 (2007).

110. **E. E. Takhtamirov and V. A. Volkov.** JETP 104, 602 (2007).

111. **S. Wang and T. K. Ng.** Phys. Rev. B 77, 165324 (2008).

112. **J. Zhang, S. K. Lyo, R. R. Du, J. A. Simmons, and J. L. Reno.** Phys. Rev. Lett. 92, 156802 (2004).

113. **P. H. Beton, P. C. Main, M. Davison, M. Dellow, R. P. Taylor, E. S. Alves, L. Eaves, S. P. Beaumont, and C. D. W. Wilkinson.** Phys. Rev. B 42, 9689 (1990).

114. **M. A. Zudov.** Ph.D thesis, University of Utah (1999).

115. **J. P. Lu, J. B. Yau, S. P. Shukla, and M. Shayegan.** Phys. Rev. Lett. 81, 1282(1998) .

116. **U. Ekenberg and M. Altarelli.** Phys. Rev. B 30, 3569 (1984);ibid. 32, 3712 (1985).

117. **D. A. Broido and L. J. Sham.** Phys. Rev. B 31, 888 (1985).

118. **L. C. Andreani, A. Pasquarello, and F. Bassani.** Phys. Rev. B 36, 5887 (1987).

119. **U. Ekenberg, L. C. Andreani and A. Pasquarello.** Phys. Rev. B 46, 2625 (1992).

120. **G. Edwards, E. C. Valadares, and F. W. Sheard.** Phys. Rev. B 50, 8493 (1994).

121. **G. Goldoni and F. M. Peeters.** Phys. Rev. B 51, 17806 (1995).

122. **G. Fishman.** Phys. Rev. B 52, 11132 (1995).

123. **J. P. Eisenstein, H. L. Stormer, V. Narayanamuri, A. C. Gossard, and W. Wiegmann.** Phys. Rev. Lett 53, 2579 (1984).

124. **R. K. Hayden, D. K. Maude, L. Eave, E. C. Valadares, M. Henini, F. W. Sheard, O. H. Hughes, J. C. Portal, and L. Cury.** Phys. Rev. Lett. 66, 1749(1991).

125. **R. K. Hayden, E. C. Valadares, M. Henini, L. Eaves, D. K. Maude, and J. C. Portal.** Phys. Rev. B46, 15586(1992) .

126. **B. E. Cole, J. M. Chamberlain, M. Henini, T. Cheng, W. Batty, A. Wittlin, J. A. A. J. Perenboom, A. Ardavan, A. Polisski, and J. Singleton.** Phys. Rev. B55, 2503(1997) .

127. **S. J. Papadakis, E. P. De Poortere, H. C. Manoharan, J. B. Yau, M. Shayegan, and S. A. Lyon.** Phys. Rev. B 65, 245312 (2002) .

128. **S. J. Papadakis, E. P. De Poortere, M. Shayegan, and R. Winkler.** Phys. Rev. Lett. 84, 5592(2000); Physica E 9, 31(2001).

129. **S. J. Papadakis, E. P. De Poortere, and M. Shayegan.** Phys. Rev. B62, 15375(2000).

130. **R. Winkler, S. J. Papadakis, E. P. De Poortere, and M. Shayegan.** Phys. Rev. Lett. 85, 4574 (2000).

131. **M. Rahimi, M. R. Sakr, S. V. Kravchenko, S. C. Dultz and H. W. Jiang.** Phys. Rev. B67, 081302(R) (2003).

132. **B. Habib, E. Tutuc, S. Melinte, M. Shayegan, D. Wasserman and S. A. Lyon, and R. Winkler.** Phys. Rev. B 69, 113311(2004) .

133. **W. Pan, L. Kai, S. P. Bayrakci, N. P. Ong, D. C. Tsui, L. N. Pfeiffer, and K. W. West.** Appl. Phys. Lett.83, 3519(2003).

134. **B. Grbic, C. Ellenberger, T. Ihn, K. Ensslin, D. Reuter, and A. D. Wieck.** Appl. Phys. Lett. 85, 2277 (2004).

135. **A. D. Wieck, and D. Reuter.** Inst. Phys. Conf. Ser. 166, 51 (2000).

136. **M. J. Manfra, L. N. Pfeiffer, K. W. West, R. de Picciotto, and K. W. Baldwin.** Appl. Phys. Lett. 86, 162106 (2005).

137. **C. Gerl, S. Schmult, H. -P. Tranitz, C. Mitzkus, and W. Wegscheider.** Appl. Phys. Lett. 86, 252105 (2005).

138. **T. M. Lu, Z. F. Li, D. C. Tsui, M. J. Manfra, L. N. Pfeiffer and K. W. West.** Appl. Phys. Lett. 92, 012109 (2008).

139. **Z. Q. Yuan, R. R. Du, M. J. Manfra, L. N. Pfeiffer, and K. W. West.** Appl. Phys. Lett. 94, 052103 (2009).

140. **G. Dresselhaus, A. F. Kip, and C. Kittel.** Phys. Rev. 98, 368 (1955).

141. **R. Winkler, S. J. Papadakis, E. P. De Poortere and M. Shayegan.** Phys. Rev. Lett 84, 713 (2000).

142. **H. W. van. Kesteren, E. C. Cosman, and W. A. J. A. van der Poel.** Phys. Rev. B41, 5283(1990).

143. **V. F. Sapega, M. Cardona, K. Ploog, E. L. Ivchenko, and D. N. Mirlin.** Phys. Rev. B 45, 4320 (1992).

144. **R. Winkle.** *Spin-Orbit Coupling Effects in Two-Dimensional Electron and Hole System.* Berlin : Springer, 2003 and references therein.

145. **Stern, F.** Phys. Rev. Lett. 21, 1687 (1968).

146. **E. Tutuc, S. Melinte, E. P. De Poortere, and M. Shayegan.** Phys. Rev. B67, 241309 (2003).

147. **R. Winkler, E. Tutuc, S. J. Papadakis, S. Melinte, M. Shayegan, D. Wasserman, and S. A. Lyon.** Phys. Rev. B 72, 195321 (2005).

148. **B. J. Roth, N. G. Sepulveda, and Jr. J. P. Wikswo.** J. Appl. Phys. 65(1), 361(1989).

149. **E. Hecht and A. Zajac.** *Optics.* Addison-Wesley, Reading, MA, 1979.

150. **A. M. Chang, H. D. Hallen, L. Harriott, H. F. Hess, H. L. Kao, J. Kwo, R. E. Miller, and T. Y. Chang.** Appl. Phys. Lett. 61, 1974 (1992).

151. **A. Oral, S. J. Bending, and M. Henini.** Appl. Phys. Lett. 69, 1324 (1996).

152. **C. Lin and C. P. Lee.** J. Appl. Phys. 67 (1), 260 (1990).

Appendix

A1. Recipe for optical lithography

Cleave a 3 mm × 5 mm sample piece from a GaAs/AlGaAs wafer, and follow steps shown below to define pattern on the sample.

1. Transfer mask pattern to photoresist on sample surface by lithography

   1.1, Clean sample surface. Rinse the surface of sample in following solvents in sequence: **Acetone → Methanol → DI water,** 5 minutes in each. In rest of recipe, the same procedure will be used in sample cleaning.

   1.2, Spin coat the sample with S1813 photoresist 6000 rpm for 40 seconds. Thickness of photoresist film will be around 15,000 Å.
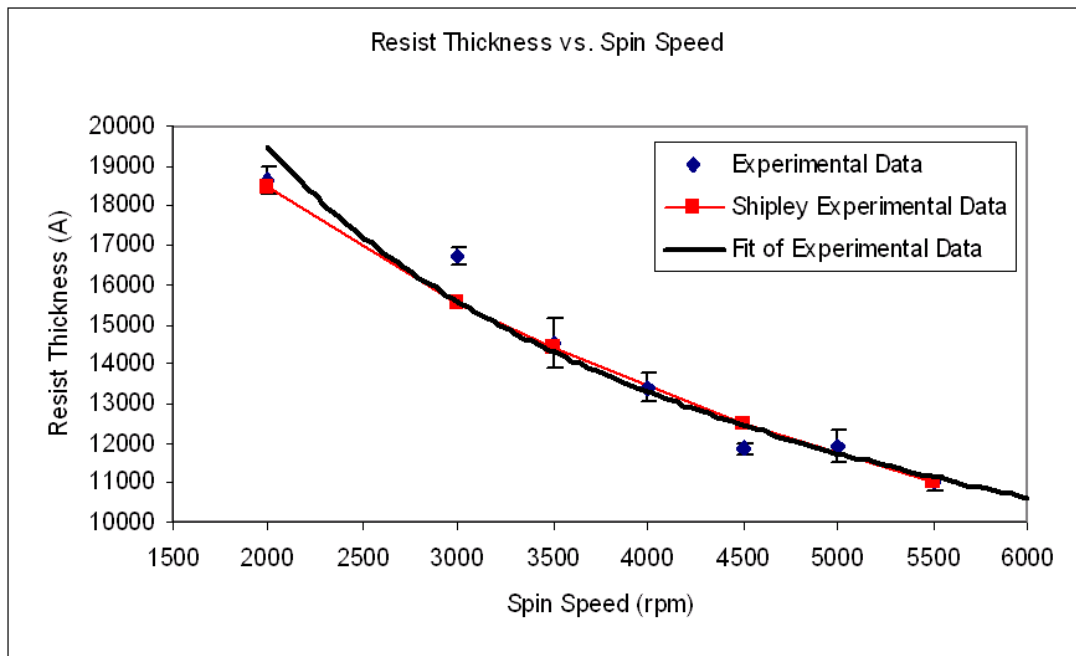

Fig. A.1 Thickness vs spin rate for photoresist 1813. (Figure adapted from website http://inside.mines.edu/Academic/courses/physics/phgn435)

1.3, Soft bake the sample at **95°C** for **60** seconds

1.4, Do exposure

Note: it is extremely important to choose right exposure time. If the photoresist is under exposure, it will remain on the exposed area after develop. While if the photoresist is over exposure, the protected area will be exposed by diffraction of UV light so that we can not get a sharp pattern. As the diffraction happens all the time, we shall choose the shortest exposure possible. The optimal exposure for S1813 is around 150 mJ/cm^2, and exposure time can be calculated from formula:

$$\text{Exposure (mJ/cm}^2) = \text{Power output level (mW/cm}^2) \times \text{Exposure time (sec)}$$

1.5, Immerse the sample in developer 321 for 30 seconds

Note: Remember, the developer also removes the unexposed photoresist but with much lower rate, so developing time shall be kept as short as possible. After developing, some windows contacts are opened on photoresist for making contacts.

2. Do etching for 2.5 minutes with etchant $H_3PO_4 : H_2O_2 : H_2O = 1 : 1 : 38$, whose etching rate on GaAs is 1200 Å /min, so the etching depth will be around 3000 Å.

A2. Recipe of making contact on n-GaAs

1. Make contact without involving thin film deposition.

    1.1. Transfer contact alloy to sample surface by solder iron tip.

        1.1.1. Cleave a piece of 2DEG sample with proper size.

        1.1.2. Heat solder iron tip to temperature 350 ˚C.

        1.1.3. Melt metals Indium (In) and Tin (Sn), and mix them to form alloy with solder iron tip.

        1.1.4. Scratch the sample surface a little bit with diamond tip and put InSn alloy to the scratched area with solder iron tip.

  1.2. Anneal contacts alloy on thermal station.

        1.2.1. Set thermal station temperature $T_1 = 450$ °C and $T_2 = 460$ °C.

        1.2.2. Flush forming gas (85% N_2 and 15% H_2) for 10 minute keeping flow meter reading 1.0.

        1.2.3. Turn on heater for 20 minutes. It takes about 8.5 minutes to reach 450 °C.

        1.2.4. Turn off heater and wait for cooling down with keeping forming gas flowing.

2. Make contacts used thin film deposition.

  2.1. Use procedure (A1.1) to transfer windows on sample surface.

  2.2. Rinse sample in dilute HCL for 10 seconds, and clean sample with DI water.

  2.3. Deposit metal alloy film on the sample surface by e-beam evaporator. In our recipe, Germanium (Ge), Palladium (Pd) and Gold (Au) are used to make contact. Deposit Ge/Pd/Au films on sample in sequence with thickness 430/300/870 Å at deposit rate of 1.5/1.5/2.5 Å respectively [152]. The thicknesses of Ge and Au films ensure ratio of Ge:Au = 12:88 in weight to keep the eutectic composition.

  2.4. Do lift-off. Immerse sample in Acetone and ultrasonic for 10 seconds so that all the metal films except for those on contacts windows are removed.

  2.5. Clean the sample with step (A1.1.1), and wait for sample dry.

Two different annealing processes can be used here. One is to use thermal station to anneal alloy. The other one is to use Rapid Thermal Annealing (RTA) machine to anneal alloy. Usually contacts annealed with RTA have better quality.

2.6. Anneal contacts alloy on thermal station.

    2.6.1. Set thermal station temperature $T_1 = 450$ ˚C and $T_2 = 460$ ˚C.

    2.6.2. Flush forming gas (85% N_2 and 15% H_2) for 10 minute, keeping flow meter reading 1.0.

    2.6.3. Turn on heater with 0.5 flowing meter reading.

    2.6.4. After temperature reach 450 ˚C, and keep it for 2 minutes.

    2.6.5. Turn off heater and cool down sample with 1.5 flowing meter reading

2.7. Anneal alloy with Rapid Thermal Annealing (RTA) machine.

    2.7.1. Pump vacuum for 40 seconds.

    2.7.2. Flush forming gas at 200 sccm for 30 seconds with vacuum valve closed, and keep form gas flowing in following steps.

    Note: if N_2, instead of forming gas, is used, 500 sccm flowing rate shall be used. Lower N_2 flowing rate will result in bad effect on sample surface so that etching process will not work.

    2.7.3. Increase temperature to 450 ˚C in 45 seconds.

    2.7.4. Keep at 450 for 2 minutes.

    2.7.5. Decrease temperate to 20 ˚C in 60 seconds.

    2.7.6. Shut down forming gas and pump vacuum for 60 seconds by open vacuum valve.

    2.7.7. Flush N_2 at 100 sccm for 60 seconds to cool down sample.

2.7.8. Pump vacuum.

2.7.9. Open purge valve to let air in.

A3. Recipe of making contact on p-GaAs (2DHG)

1. Transfer contact alloy to sample surface by solder iron tip.

   1.1. Cleave a piece of 2DHG sample with proper size.

   1.2. Heat solder iron tip to temperature 475 ˚C.

   1.3. Melt metals Indium (In) and Zinc (Zn), and mix them to form alloy with solder iron tip.

   1.4. Scratch the sample surface a little bit with diamond tip and put InZn alloy to the scratched area with solder iron tip.

2. Anneal contacts alloy on thermal station.

   2.1. Set thermal station temperature $T_1 = 450$ ˚C and $T_2 = 460$ ˚C.

   2.2. Flush forming gas (85% N_2 and 15% H_2) for 10 minute keeping flow meter reading 1.0.

   2.3. Turn on heater for 20 minutes. It takes about 8.5 minutes to reach 450 ˚C.

   2.4. Turn off heater and wait for cooling down with keeping forming gas flowing.

A4. Recipe of introducing antidot lattice to sample surface

1. Use procedure (A2.2) to make contacts by thin film deposition.

2. Use procedure (A1) to define Hall bar pattern on sample surface.

3. Introduce antidot lattice to sample with e-beam lithography.

   3.1. Clean sample surface.

   3.2. Spin coating sample with 950K A2 PMMA at 3000 rpm for 40 seconds. At this spin rate, the thickness of PMMA film is around 100 nm.

   3.3. Bake sample at 160 ℃ for 2 hours in oven.

   3.4. Write antidot pattern on PMMA with SEM (JEOL 6500). For e-beam lithography, SEM shall work at high voltage, 30 kV, with smallest aperture and 7 mm work distance. The exposure dose shall be $400 \sim 600 \ \mu C/cm^2$.

   3.5. Do development. Immerse sample in developer (MIBK: IPA = 1: 3) for 60 seconds, then IPA for 20 seconds.

   3.6. Do Reactive Ion Etching (Oxford PlasmalabSystem 90 RIE) for 30 seconds with following parameters:

BCl$_3$	85 sccm
Cl$_2$	50 sccm
Pressure	45mT
Power	150W
Temperature	20 ˚C

   Note: Wet chemical etching can be used here, but the diameter of antidot will be enlarged by wet etching.

3.7. Clean sample surface.

A5. MatLab codes for building ring currents.

```
clear
warning off MATLAB:divideByZero;
L=input('Area size (um) L= [6]');
if isempty(L)
    L=6;
end
N=input('Point number N= [64]');
if isempty(N)
    N=64;
end
r=input('Current orbit radius (um) r= [0.5]');
if isempty(r)
    r=0.5;
end
d=input('Distance between current orbit (um) d= [2]');
if isempty(d)
    d=2;
end
dx=L/N;
J=zeros(N);
Jx=J;
Jy=J;
pn=fix(L/d)+1;
for p=1:pn
    for q=1:pn
        x0=(p-1+rand(1)/2)*d;
        y0=(q-1+rand(1)/2)*d;
        for x=1:N
            for y=1:N
                x1=x*dx;
                y1=y*dx;
                dr=abs(sqrt((x1-x0)^2+(y1-y0)^2)-r);
                if dr<=3*L/N
                    J(x,y)=J(x,y)+exp(-10*dr);
                    if x1-x0~=0
                        Jx(x,y)=Jx(x,y)+sign(x1-x0)*J(x,y)*cos(atan((y1-y0)/(x1-x0)));
                        Jy(x,y)=Jy(x,y)-sign(x1-x0)*J(x,y)*sin(atan((y1-y0)/(x1-x0)));
                    else
                        Jy(x,y)=Jy(x,y)-sign(y1-y0)*J(x,y);
                    end
                end
            end
        end
    end
```

```
        end
    end
    filen=input('Please input filename to save data: [Jd0]','s');
    if isempty(filen)
        filen='Jd0';
    end
    save(filen,'N','L','J','Jx','Jy');
    clear d dr dx filen p pn q r x x0 x1 y y0 y1;
    %figure('name','Jx')
    %surface(Jx)
    %figure('name','Jy')
    %surface(Jy)
    figure('name','J')
    surface(real(J))
```

A6. MatLab codes for calculating z component of magnetic field.

```
    clear
    filen=input('Please input filename to load:','s');
    if isempty(filen)
        filen='Jd1';
    end
    load(filen);
    clear filen;
    %N=size(Jx,1)
    d=1*10^(-9);
    z=0.5*10^(-6);
    c0=i*2*pi*10^(-7)*d;
    dx=L/N;
    dk=2*pi/N/dx;
    k=ones(N,1);
    %x=ones(N,1);
    bz=zeros(N);
    for m=1:N
        k(m)=-pi/dx+(m-1)*dk;
        %k(m)=m*dk;
        %x(m)=-N*dx/2+(m-1)*dx;
    end
    jx=fft2(Jx);
    jy=fft2(Jy);
    for m=1:N
        for n=1:N
```

```
        if m<=N/2
            u=m+N/2;
        else
            u=m-N/2;
        end
        if n<=N/2
            v=n+N/2;
        else
            v=n-N/2;
        end
        kt=sqrt(k(u)*k(u)+k(v)*k(v));
        if kt==0
            bz(u,v)=-exp(-i*pi*(m+n-2))*(jx(m,n)-jy(m,n));
        else
            bz(u,v)=-exp(-kt*z)*exp(-i*pi*(m+n-2))*(k(u)*jx(m,n)-k(v)*jy(m,n))/kt;
            %bz(u,v)=exp(-kt*z)*exp(-i*2*pi*(u+v)/N)*kt/k(u)*jx(m,n);
            %bz(u,v)=-exp(-kt*z)*exp(-i*2*pi*(u+v)/N)*kt/k(u)*jy(m,n);
        end
    end
end
clear jx jy;
bz=c0*bz*dx*dx;

Bzt=ifft2(bz);
Bz=Bzt;
for m=1:N
    for n=1:N
        if m<=N/2
            u=m+N/2;
        else
            u=m-N/2;
        end
        if n<=N/2
            v=n+N/2;
        else
            v=n-N/2;
        end
        Bz(u,v)=exp(i*pi*(m+n-2))*Bzt(m,n);
    end
end
```

```
   clear jy bz Bzt m n u v;

   filen=input('Please input filename to save variables: [Bz0]','s');
   if isempty(filen)
      filen='Bz0';
   end
   save(filen,'Bz','J','Jx','Jy','L','N');

   clear dk dx k kt L N c0 d z filen;

   figure('name','Bz')
surface(real(Bz))
```

A7. MatLab codes for recovering ring currents by Fast Fourier Transform technique.

```
clear
filen=input('Please input filename to load: [Bz0]','s');
if isempty(filen)
    filen='Bz0';
end
load(filen);
clear filen;

%N=size(Bz,1)
d=1*10^(-9);
z=0.5*10^(-6);
c0=i*2*pi*10^(-7)*d;
dx=L/N;
dk=2*pi/N/dx;
k=ones(N,1);
%x=ones(N,1);
bz=zeros(N);
for m=1:N
   k(m)=-pi/dx+(m-1)*dk;
   %x(m)=-N*dx/2+(m-1)*dx;
end

bz=fft2(Bz);
```

```
jx=bz;
jy=bz;
for m=1:N
   for n=1:N
      if m<=N/2
         u=m+N/2;
      else
         u=m-N/2;
      end
      if n<=N/2
         v=n+N/2;
      else
         v=n-N/2;
      end
      kt=sqrt(k(u)*k(u)+k(v)*k(v));
      if kt==0
         jx(u,v)=-exp(-i*(m+n-2)*pi)*bz(m,n);
         jy(u,v)=exp(-i*(m+n-2)*pi)*bz(m,n);
      else
         jx(u,v)=-exp(kt*z)*k(u)/kt*exp(-i*(m+n-2)*pi)*bz(m,n);
         jy(u,v)=exp(kt*z)*k(v)/kt*exp(-i*(m+n-2)*pi)*bz(m,n);
      end
   end
end
clear bz;
jx=jx/c0;
jy=jy/c0;

Jxct=ifft2(jx);
Jyct=ifft2(jy);
clear jx jy;
Jxc=Jxct;
Jyc=Jyct;
for m=1:N
   for n=1:N
      if m<=N/2
         u=m+N/2;
      else
         u=m-N/2;
      end
```

```matlab
        if n<=N/2
            v=n+N/2;
        else
            v=n-N/2;
        end
        Jxc(u,v)=exp(i*(m+n-2)*pi)*Jxct(m,n);
        Jyc(u,v)=exp(i*(m+n-2)*pi)*Jyct(m,n);
    end
end
clear Jxct Jyct;
Jxc=real(Jxc);
Jyc=real(Jyc);
Jc=zeros(N);
Jc=(Jxc.*Jxc+Jyc.*Jyc).^(0.5);

filen=input('Please input filename to save current J: [J0]','s');
if isempty(filen)
    filen='J0';
end
save(filen,'Bz','J','Jx','Jy','L','N');

clear dk dx k kt L N c0 d z filen m n u v;

figure('name','Jx')
surface(Jx)
figure('name','Jy')
surface(Jy)
figure('name','J')
surface(J)
figure('name','Jxc')
surface(Jxc)
figure('name','Jyc')
surface(Jyc)
figure('name','Jc')
surface(Jc)
```